

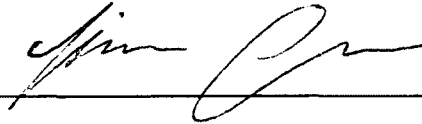
SURFACE PLASMON ENHANCED
QUANTUM DOT INFRARED PHOTODETECTOR

BY

PUMINUN VASINAJINDAKAW
B.S. CHULALONGKORN UNIVERSITY (2004)
M.S. UNIVERSITY OF MASSACHUSETTS LOWELL (2009)

SUBMITTED IN PARTIAL FULFILLMENT OF THE REQUIREMENTS
FOR THE DEGREE OF DOCTOR OF PHILOSOPHY
ELECTRICAL ENGINEERING
UNIVERSITY OF MASSACHUSETTS LOWELL

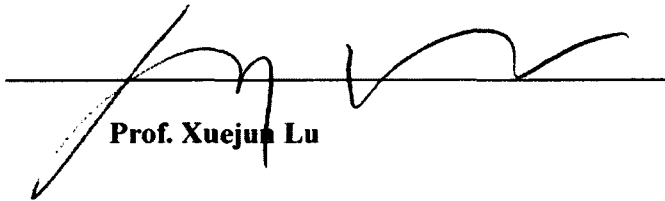
Signature of Author: _____



Date: _____

July 27, 2012

Signature of Dissertation Supervisor: _____



Name Typed: _____

Prof. Xuejun Lu

Signatures of Other Dissertation Committee Members

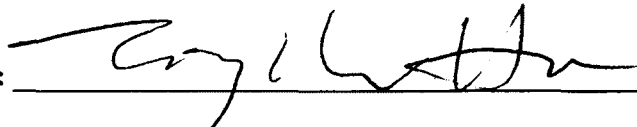
Committee Member Signature: _____



Name Typed: _____

Prof. Joel Therrien

Committee Member Signature: _____



Name Typed: _____

Prof. Tingshu Hu

**SURFACE PLASMON ENHANCED QUANTUM DOT INFRARED
PHOTODETECTOR**

BY

PUMINUN VASINAJINDAKAW

**ABSTRACT OF A DISSERTATION SUBMITTED TO THE FACULTY OF THE
DEPARTMENT OF ELECTRICAL AND COMPUTER ENGINEERING
IN PARTIAL FULFILLMENT OF THE REQUIREMENTS**

**FOR THE DEGREE OF
DOCTORAL OF PHILOSOPHY
ELECTRICAL AND COMPUTER ENGINEERING
UNIVERSITY OF MASSACHUSETTS LOWELL
2012**

**Dissertation Supervisor: Xuejun Lu, Ph.D,
Associate Professor, Department of Electrical and Computer Engineering**

UMI Number: 3532874

All rights reserved

INFORMATION TO ALL USERS

The quality of this reproduction is dependent upon the quality of the copy submitted.

In the unlikely event that the author did not send a complete manuscript and there are missing pages, these will be noted. Also, if material had to be removed, a note will indicate the deletion.



UMI 3532874

Published by ProQuest LLC 2012. Copyright in the Dissertation held by the Author.

Microform Edition © ProQuest LLC.

All rights reserved. This work is protected against
unauthorized copying under Title 17, United States Code.



ProQuest LLC
789 East Eisenhower Parkway
P.O. Box 1346
Ann Arbor, MI 48106-1346

ABSTRACT

Quantum dot infrared photodetector (QDIP) is a promising technology for infrared applications especially the infrared camera. Surface plasmon (SP) resonance on metallic thin film is recognized for an intense electrical field on the thin film surface with an extraordinary transmission. This dissertation objective is to improve the performance of QDIP detector by SP structure with the capability to apply on the focal plane array. The methodology is to integrate SP structure with the QDIP detector to enhance its overall performance. Begin with the investigation on the metallic thin film SP structures; The SP excitation throughout the transmission profiles on the middle-wave and long-wave infrared region is observed and discussed. Next, the SP structure is integrated on the QDIP detector and found the enhancement on the overall performance. The performance enhancement is discussed and found to be related to the SP excitation.

Two projects from the preliminary investigation are chosen to be fully investigated on QDIP. First, the wavelength selection enhancement depending on the polarization selection is reported. It is found that two wavelengths of enhancement can be achieved by the specific design of the SP structure integrated on QDIP. The performance enhancement is also reported. Second, the optimization of the performance enhancement was studied. It was found that the performance of QDIP with SP structure can be optimized by varying the metal thickness and the hole size diameter of the SP structure.

We believe that we have overcome the difficulty of polarization selection of the QDIP by sidestepping with our designed SP structure. We also demonstrate the performance improvement on the QDIP with metal thickness and hole diameter variation. Both of the projects including preliminary investigation are fabricated by the standard photolithography. Hence it is compatible with focal plane array fabrication. Our results address the development of infrared sensor and potentially offer the development of focal plane array cameras which will improve the performance of infrared camera.

ACKNOWLEDGEMENTS

I fully thank my advisor, Prof. Xuejun Lu, for every kind of support and advice. An invaluable experience and enjoyment of working with him will never be forgotten.

I thank Prof. Tingshu Hu and Prof. Joel Therrien for serving on the dissertation committees.

I thank Mr. Jarrod Vaillancourt for all of his help from the beginning of my research until the end.

I thank my father, mother, and sister for their love and care throughout my life. They are the first and foremost ingredient of my success.

TABLE OF CONTENTS

I. Introduction	1
1. Background	1
2. Dissertation structure	2
II. QDIP architecture & Plasmonics background.....	4
1. Quantum Dot Infrared Photodetector (QDIP).....	4
1.1. Introduction to QDIPs	4
1.2. Structure, Growth, and Fabrication	12
1.3. Characterization.....	16
1.4. Figure of Merit.....	19
2. Plasmonics Background.....	25
III. Preliminary Result (Plasmonics Enhanced QDIP).....	29
1. Initial Test and Design	29
2. Verification Experiment.....	33
3. Further Investigation.....	42
3.1. Lattice Alignment.....	42
3.2. Polarization Selection.....	43
3.3. Hole Size Variation	46

3.4. Metal Thickness Variation.....	47
3.5. Metal Selection	49
4. Conclusion	53
IV. Polarization Selection of Surface Plasmon Enhanced QDIP	54
1. Introduction.....	54
2. Surface Plasmon Structure Design.....	55
3. Device Fabrication (QDIP#2461)	62
4. Result and Discussion	64
5. Conclusion	69
V. Metal Thickness Variation Effect of Surface Plasmon Enhanced QDIP	71
1. Introduction.....	71
2. Transmission of Surface Plasmon Structure with Metal Thickness Variation	72
3. Device Fabrication (UML273)	80
4. Result and Discussion	83
5. Conclusion	96
VI. Literature cited.....	97

LIST OF FIGURES

Figure 1 Electromagnetic Wave Spectrums.....	5
Figure 2 Active Infrared Night Vision Camera	6
Figure 3 Diagram of Photon Absorption in Semiconductor	9
Figure 4 Physical Material and Band Diagram of QWIP	10
Figure 5 Absorption on the Conduction Band	11
Figure 6 QDIP Structure	13
Figure 7 (a)-(j) Fabrication Procedure of QDIP	15
Figure 8 Mounted QDIP Sample	16
Figure 9 PL Measurement Band Diagram	17
Figure 10 Example of XTEM Image on QDIP Sample.....	18
Figure 11 Example of XTEM Image on QDIP Sample Absorption Layer.....	18
Figure 12 AFM Measurements, Left: 1 μ m by 1 μ m Area, Right: 2 μ m by 2 μ m Area	19
Figure 13 Black Body Radiations at Different Temperature	21
Figure 14 Noise Current Spectrums at Different Bias Voltages.....	24
Figure 15 The Lycurgus Glass. Left side: Observed Transmitted Light. Right side: Observed Reflected Light. <i>*Image from http://en.wikipedia.org/wiki/Lycurgus_Cup.....</i>	26
Figure 16 SP Metallic Hole Array (6 μ m period)	30
Figure 17 SP Metallic Hole Array (2.6 μ m period) (SEM)	30
Figure 18 Transmission Profile1 of SP Sample on GaAs.....	31

Figure 19 Transmission Profile ² of SP Sample on GaAs.....	32
Figure 20 Relationship Between the Peak & Dip Position and Period Size.....	33
Figure 21 2DSHA on QDIP (Optical Microscope).....	35
Figure 22 2DSHA on QDIP (SEM).....	36
Figure 23 Spectral Response and Transmission Profile Comparison.....	38
Figure 24 Noise Current Comparisons	40
Figure 25 Responsivity Comparison.....	41
Figure 26 Detectivity Comparison.....	41
Figure 27 Transmission Profile of SP (Square vs Hexagonal Array).....	43
Figure 28 Hexagonal Lattice Hole Array and Square Lattice Hole Array	43
Figure 29 2.6x-3.0y-1.3um Sample	44
Figure 30 2.6x-3.0y-1.3um Sample Transmission Profile.....	45
Figure 31 Transmission of 2.6x-3.0y-1.3um Sample for Polarization Selection	46
Figure 32 Transmission of SP Varied Hole Size	47
Figure 33 Transmission of SP with Different Metal Thickness.	48
Figure 34 Transmission of SP Varied Metal Thickness (Zoom in).....	48
Figure 35 Transmission Profile of Gold (Au), Silver (Ag), Cobalt (Co), and Titanium (Ti)	50
Figure 36 Spectrum Response of UML302SP (Ag)	52
Figure 37 Spectrum Response and Enhancement Ratio of UML302SP (Ag).....	52
Figure 38 Transmission Profile of Surface Plasmon Structure on GaAs.....	57
Figure 39 SP Period Design.....	58
Figure 40 QDIP Diagram: Left Side for Ref-QDIP, Right Side for SP-QDIP	58

Figure 41 2.6x-3.0y-1.3um Sample Transmission Profile.....	59
Figure 42 2DSHA on QDIP	60
Figure 43 Transmission of 2.6x-3.0y-1.3um Sample for Polarization Selection	61
Figure 44 Photocurrent Spectrum of 2DSHA-QDIP	64
Figure 45 Polarization Selection on 2DSHA-QDIP (No Polarizer)	65
Figure 46 Polarization Selection on 2DSHA-QDIP (0 Degree)	66
Figure 47 Polarization Selection on 2DSHA-QDIP (45 Degree)	66
Figure 48 Polarization Selection on 2DSHA-QDIP (90 Degree)	67
Figure 49 Polarization Selection on 2DSHA-QDIP (Summary)	68
Figure 50 Enhancement Ratio on 2DSHA-QDIP	69
Figure 51 Transmission of Plasmonics Structure Varied Metal Thickness.....	74
Figure 52 Transmission of Plasmonics Structure Varied Temperature.....	75
Figure 53 Transmission of Plasmonics Structure Varied Metal Thickness (15nm-300nm)	76
Figure 54 Transmission of Plasmonics Structure Varied Metal Thickness (15nm-300nm) Zoom in.....	76
Figure 55 Maximum-Minimum Value of Transmission Profile.....	77
Figure 56 Transmission Profile of Surface Plasmon Structure 2.6um Period	78
Figure 57 Calculated Momentum Vector (kz) on Wavelength Domain	79
Figure 58 Correlation Coefficient of kz	79
Figure 59 UML273 MBE Growth Structure.....	81
Figure 60 UML273-SP (SEM@430x magnification).....	82
Figure 61 UML273-SP (SEM@3700x magnification).....	82

Figure 62 UML273-SP (SEM@12000x magnification).....	83
Figure 63 UML273-SP Spectrum Response $V=-0.47V$	84
Figure 64 UML273-SP Spectrum Response $V=-0.70V$	84
Figure 65 UML273-SP Spectrum Response $V=-1.20V$	85
Figure 66 UML273-SP Enhancement Ratio	85
Figure 67 UML273-SP Enhancement Ratio Zoom in	86
Figure 68 UML273-SP Enhancement Ratio Varied Metal Thickness.....	87
Figure 69 UML273-SP Enhancement Ratio Varied Metal Thickness Zoom in.....	87
Figure 70 UML273-SP Enhancement Ratio Varied Metal Thickness $V= -0.70V$	88
Figure 71 Maximum Value of Enhancement on QDIP (UML273-SP2.6-1.3 μm).....	89
Figure 72 UML291-SP Hole Diameter 1.2 μm	90
Figure 73 UML291-SP Hole Diameter 1.3 μm	91
Figure 74 UML291-SP Hole Diameter 1.4 μm	91
Figure 75 UML291-SP Hole Diameter 1.5 μm	92
Figure 76 UML291-SP Au 25nm	93
Figure 77 UML291-SP Au 37.5nm	93
Figure 78 UML291-SP Au 50nm	94
Figure 79 UML291-SP Au 62.5nm	94
Figure 80 UML291-SP Au 75nm	95
Figure 81 UML291-SP Au 100nm	95

I. INTRODUCTION

1. Background

During the last ten years, an approach to tailor the properties of the materials, called bandgap engineering, has been developed. Bandgap engineered photodetectors were developed toward fiber optic communication (at wavelength of 1.4 μ m) and military application (at wavelength of 8-12 μ m) such as missile guidance, night vision and surveillance [1-3]. Quantum dot infrared photodetectors (QDIP) are one of the developments from bandgap engineering used for long-wavelength infrared detection (8-12 μ m). QDIPs are a promising alternative for the long-wavelength infrared detection and imaging applications [4, 5]. QDIPs have very low noise current and the manufacturing cost of QDIPs is much lower than the established HgCdTe detector. However, due to the accumulated strain in multi-stacked quantum dot layers, the number of absorption layers is limited to a few tens periods. The limited number of absorption layers limits the QDIPs performance and is a barrier to overcome compared to current infrared detector.

Also, during the last ten years, surface plasmon (SP) effect has been investigated and reported [6-13]. Surface plasmon has the ability to couple with photons on metal-dielectric interface. Such a coupling effect results in a strong electromagnetic field which leads to a field enhancement on the metal-dielectric interface. This captivating research

topic has found itself used in various applications. A famous example of surface plasmon in a commercial application is surface enhanced Raman scattering (SERS). The field enhancement on the metal-dielectric interface also gives rise to the possibility of performance enhancement on QDIPs. In this dissertation, plasmonics structures are monolithically integrated onto QDIPs in order to enhance its performance. The characteristic of the plasmonics structures in conjunction with QDIPs will be studied.

2. Dissertation structure

Chapter II: The background of QDIPs will be presented together with method of growth and fabrication, and also with the pertinent figure of merits for QDIPs. An introduction of surface plasmon effect will also be discussed.

Chapter III: This chapter presents the preliminary results of our design and initial tests followed by the verification experiments. The performance enhancements of the surface plasmon structure on QDIPs will be discussed.

Chapter IV: As a consequence of the investigation from the preliminary results in Chapter III, the designed surface plasmon structure is applied on top of the QDIPs. The device characterizations are shown. The polarization selection will be discussed together with the performance enhancement of QDIPs.

Chapter V: As a consequence of the investigation from the preliminary results in Chapter III, the effect of the metal thickness on surface plasmon structure will be studied

on QDIPs. The metal thickness variation of surface plasmon structure on QDIPs will be optimized and reported.

II. QDIP ARCHITECTURE & PLASMONICS

BACKGROUND

1. Quantum Dot Infrared Photodetector (QDIP)

1.1. Introduction to QDIPs

Infrared (IR) light is the part of the electromagnetic spectrum which lies in between the visible light and microwave regions. The infrared spectrum spans roughly from 700nm to 300um. In the sensor field, the infrared spectrum can be divided into 5 sub-regions, which are 1.) Near infrared (NIR), covering from 0.7 – 1.0um, 2.) Short-wavelength infrared (SWIR), covering from 1.0 – 3.0um, 3.) Middle-wavelength infrared (MWIR), covering from 3 – 5um, 4.) Long-wavelength infrared (LWIR), covering from 8 – 12um, 5.) Very-long wavelength infrared (VLWIR), lies from 12 – 30um. Figure 1 shows the infrared and sub-infrared spectrum.

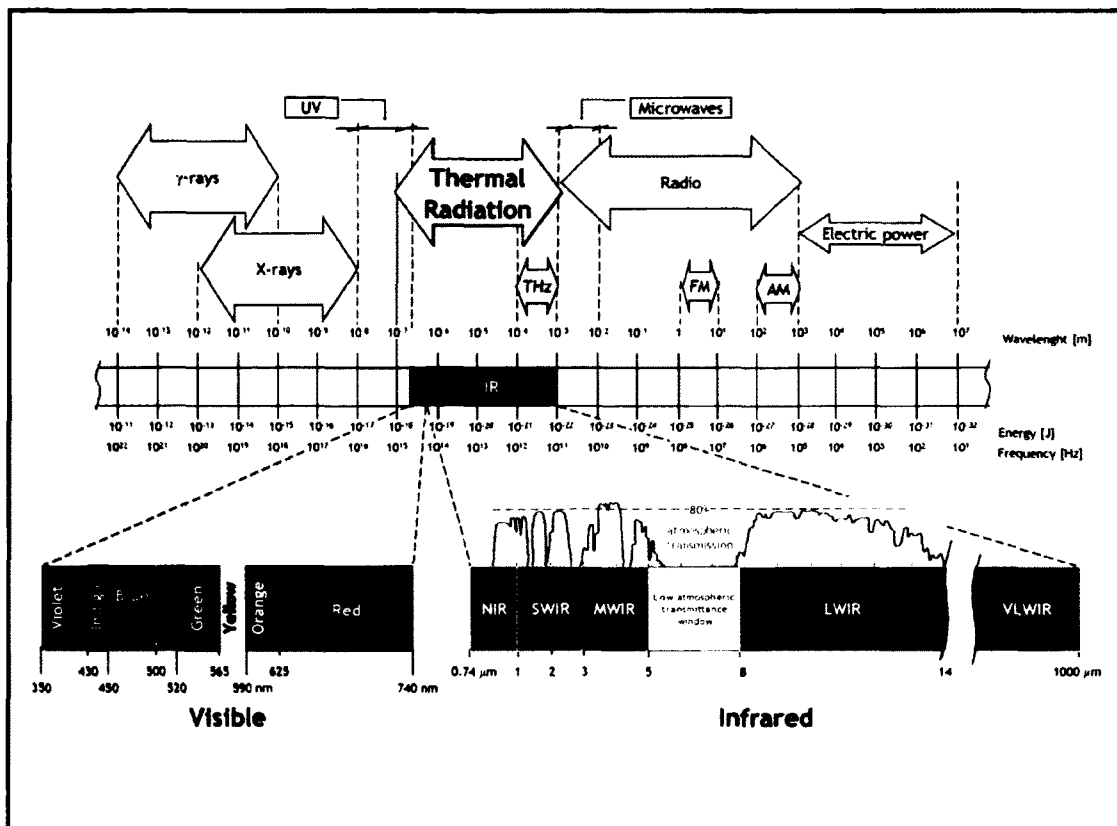


Figure 1 Electromagnetic Wave Spectrums

**Image from http://en.wikipedia.org/wiki/Infrared_vision. Author: Clemente Ibarra-Castanedo @ Canada Research Chair in Multipolar Infrared Vision - MiViM*

Infrared sensors have been used for many applications in various fields. The majority of uses fall in military and space domains. The military applications include missile guidance, night vision, and surveillance [2]. Examples of space applications are satellite detection, space observation, space vehicle navigation and flight control [14]. For nonmilitary applications, infrared sensors also play important roles in optical communication, remote control, thermography camera, night vision, and weather satellites [14].

Figure 2 shows the advantage of an Active-Infrared night vision system. Despite an invisible scene for bare eyes, active-infrared night vision can deliver the scene details, as seen on the display monitor.

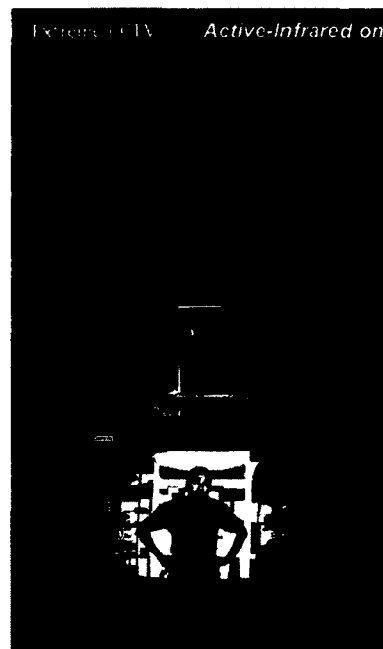


Figure 2 Active Infrared Night Vision Camera

**Image from www.ExtremeCCTV.com*

Infrared detectors can be divided into two categories. The first is infrared thermal detectors such as bolometer and thermopile, and the other is infrared photo detectors which are quantum well infrared photodetector (QWIP) and quantum dot infrared photodetector (QDIP).

Infrared thermal-detector

Bolometer:

Detector which detects a change in resistance based incident photon flux is called a bolometer. The principle is based on the temperature increase caused by absorption of incident radiant energy. It consists of an absorber, which is usually a thin metal plate, and external electrical circuits. The absorber connects to a heat sink by a weak thermal link. Absorption of infrared radiation causes the temperature of the thin-film to change depending on the metal properties of the absorber. The temperature increase causes a change in electrical resistance, which is subsequently measured by the external electrical circuit. When the radiation is shut off, the absorber cools down with the heat sink, and temperature relaxes back to its initial value again. A bolometer is considered to be a sensitive detector. To achieve the best sensitivity, it must be cooled down near absolute zero. Modern bolometers based on semiconductor films, which are called micro-bolometers, are small and light in weight. However, it still has drawbacks regarding the slow response, and reliability issues.

Thermopile:

The working principle of a thermopile detector is based on the thermoelectric effect. A temperature gradient along a conductor creates an electro-magnetic field. If two conductors of different materials are joined at one point, an electro-magnetic field (which is a voltage) is created between the open ends. The electro-magnetic field generated depends on the temperature of each junction. A thermopile is used by medical professionals to measure body temperature such as the ear thermometer. It can also be

used in heat flux sensor, gas burner safety controls, and microwave oven sensor. Modern thermopiles are made from thin films that can be fabricated into complex arrays. Thermopiles have slow response times compared to other thermal detectors. The voltage generated from the device is usually in order of tens millivolts. Therefore, it requires amplifiers which can be large and expensive.

Infrared Photodetector

An infrared photodetector converts an electromagnetic wave (light) into an electrical signal such as current or voltage. The working principle is explained as followed. A photon is absorbed in the material that generates electron in the conduction band (CB) and hole in the valance band (VB). The generated electron hole pairs (EHPs) are subsequently collected and formed photocurrent. In an interband transition photodetector, the energy of photon must be larger or equal to the band gap of the semiconductor material. In the intersubband transition photodetector, the energy of the photon must be greater or equal to the energy gap between ground state and continuum state in the material. The relation between photon energy and wavelength is given by:

$$E = h\nu = \frac{hc}{\lambda} \quad \text{Equation 1}$$

where as E is the energy of the photon, h is the Plank's constant, ν is the frequency of light, c is the speed of light, and λ is the wavelength of the light.

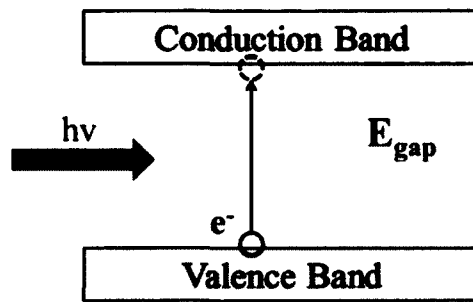


Figure 3 Diagram of Photon Absorption in Semiconductor

Interband and Intersubband Transition Photodetector

For the interband transition photodetector, the incident photon, which has energy greater than or equal to the band gap of the semiconductor material, is absorbed in the material and creates excess electron-hole pairs in the conduction band and valence band. By either built-in electrical field or an external electrical field that applied across the device, electron-hole pairs are swept along the electrical field direction and collected by the external electrodes to produce a current.

The current state-of-the-art interband transition photodetector are based on mercury cadmium telluride (MCT, HgCdTe). By using growth techniques such as liquid phase epitaxy (LPE) or molecular beam epitaxy (MBE), the composition can be changed to form $\text{Hg}_{1-x}\text{Cd}_x\text{Te}$. The spectral range of $\text{Hg}_{1-x}\text{Cd}_x\text{Te}$ can be designed to cover the SWIR to LWIR range. HgCdTe detector has a fast response time and high sensitivity compare to other infrared detectors. However, the cost is relatively high and its application of LWIR needs to be cooled down to 77K or colder in order to reduce noise in the device.

In an intersubband transition photodetector, the stacks of different material are grown by molecular beam epitaxy (MBE) with a precise (atomic level) control of the thickness of each layer. The thin layers with different energy gap of each layer form quantum wells and generate discrete energy levels in both conduction band and valence band. The discrete energy levels have reduced density of states (DOS) in the quantum well. Examples of intersubband transition photodetector are quantum well infrared photodetector (QWIP) and quantum dot infrared photodetector (QDIP).

Quantum well infrared photodetector (QWIP)

The basic operation principle of QWIP is described as following. When incident light shines on the detector with appropriate energy, electron in ground state absorbs photon energy and excites to a higher energy level near continuum band. The applied bias causes the electron to tunnel through the potential barrier to the continuum where it can be collected as photocurrent.

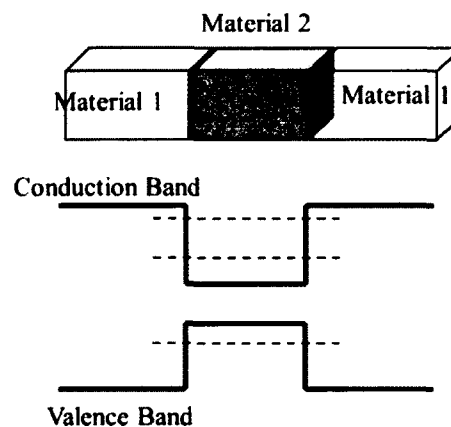


Figure 4 Physical Material and Band Diagram of QWIP

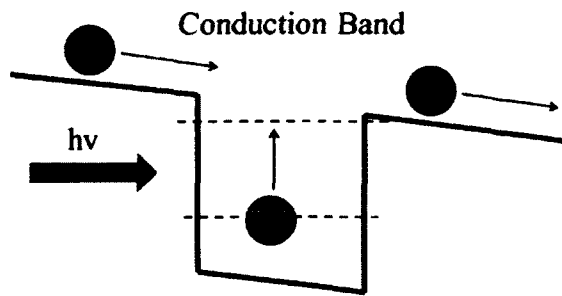


Figure 5 Absorption on the Conduction Band

QWIPs have several advantages over other IR detectors. First, QWIPs have low cost and good uniformity compared to other IR detectors. Secondly, it offers high sensitivity with wavelength flexibility in MWIR, LWIR, and VLWIR regions [1, 2]. Thirdly, it has multicolor capability over the other IR detectors [1, 2]. However, QWIPs have the disadvantage due to its inability to absorb normal incident radiation [3] and the need for cryogenic cooling.

Quantum dot infrared photodetector (QDIP)

QDIPs were developed from QWIPs. The basic principle operation of QDIPs is quite similar to QWIPs. The only difference is that instead of having one dimensional confinement, QDIP has three dimensional confinements. The third dimension confinement allows sensitivity on normal incident radiation [15]. QDIPs also have other advantages which outweigh QWIPs. QDIPs have a lower dark current than a QWIPs since the density of states in QDs are much lower than that in QWs, which allows QDs to hold less thermally-generated electrons and thus less dark current [16]. In addition, QDIPs have long excited state lifetime which allows efficient collection of photo-excited carriers and this leads to high photoconductive gain and photoresponsivity [16].

1.2. Structure, Growth, and Fabrication

Molecular beam epitaxy (MBE) is the method of depositing an atomic thickness onto the substrate. MBE is a common method used to grow the quantum wells and quantum dots devices. Self-assembled quantum dots device is also grown by MBE by using the Stranski-Krastanov (SK) method. The SK method is based on growing a lattice mismatched film of different materials such as InAs on GaAs. This lattice mismatch introduces the strain on the surface between two materials. Beyond a certain thickness, the edge dislocation will occur and islands will form to alleviate the stress.

The QDIP structure is shown below in Figure 6. The QDIP was grown using a V80H MBE System, start from 0.3 μm Si-doped (n+) GaAs bottom contact layer ($n = 1 \times 10^{18} \text{ cm}^{-3}$), followed by the growth of a 0.1 μm undoped GaAs buffer layer. 10 periods of InAs quantum dots absorption band (2ML) with spacer layers of 50nm GaAs were then grown. Next, 150nm GaAs spacer layer were grown, followed by 0.1 μm highly Si-doped ($n=1 \times 10^{18} \text{ cm}^{-3}$). The surface quantum dot on the top is for characterization purposes. The top surface quantum dot will be used to measure the size and height by atomic force microscope (AFM). Then it will be removed by wet etching before QDIP fabrication process begins.

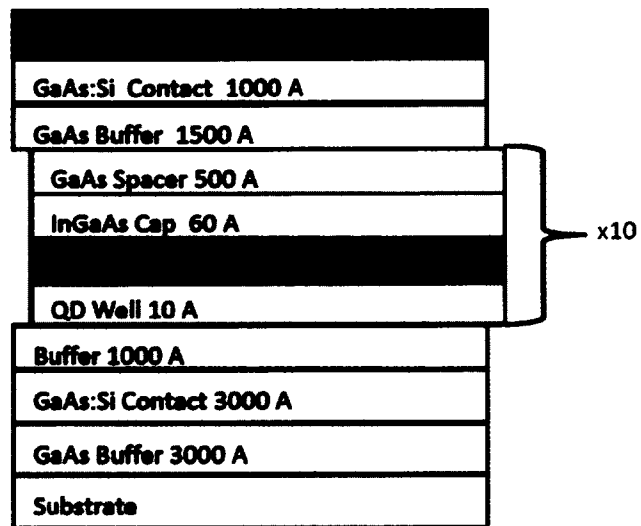
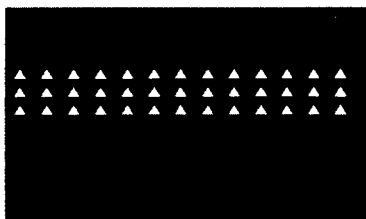
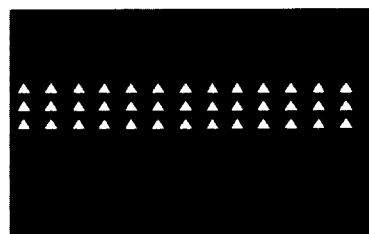


Figure 6 QDIP Structure

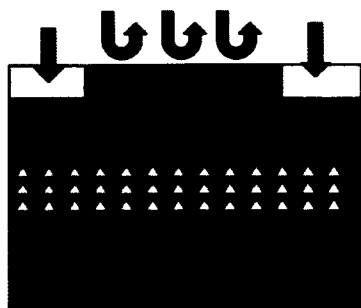
Fabrication procedures of the self-assembled quantum dots are schematically shown in Figure 7 (a) through (j).



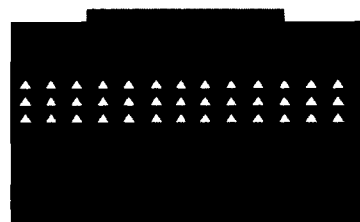
(a)



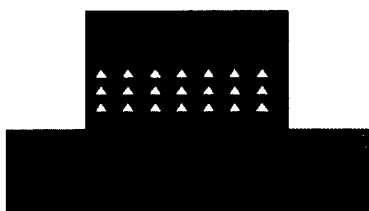
(b)



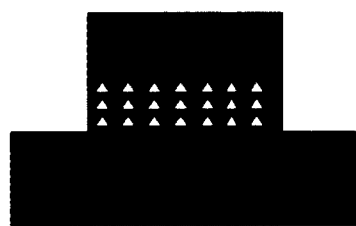
(c)



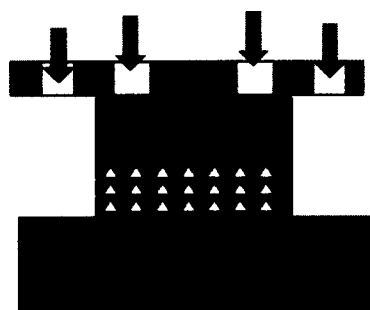
(d)



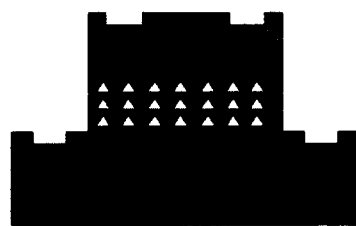
(e)



(f)



(g)



(h)

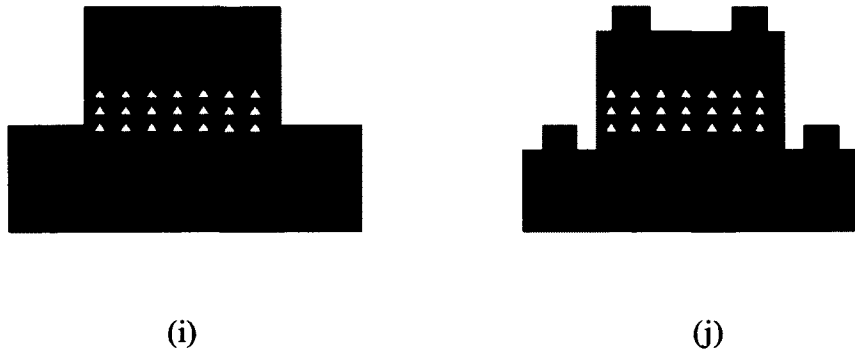


Figure 7 (a)-(j) Fabrication Procedure of QDIP

After MBE growth, a test photodetector array is fabricated using the steps shown above. The wafer is spin-coated with a positive photoresist (Figure 7(b)). After 3 minutes soft baking at 95°C , the wafer is then exposed with UV light using a photo mask containing the QDIP patterns (Figure 7(c)). The exposed wafer is then developed using CD-30 developer. The desired photoresist pattern will be transferred onto the wafer (Figure 7(d)). The wafer is then etched by using piranha etch solution containing sulfuric acid (H_2SO_4): hydrogen peroxide (H_2O_2) : water (H_2O) in the ratio of 1: 8: 80 by volume. The QDIP mesa is now formed (Figure 7(e)). The photoresist is then removed using a solvent bath and the wafer is then washed using deionization water (DI) and spin coated with the photoresist and soft baked again (Figure 7(f)). Using the mask for metal electrode patterns, we aligned the photo mask with mesas and exposed (Figure 7(g)). After it is developed, the metal contact patterns on the wafer will be opened (Figure 7(h)). The wafer is then deposited with the metal alloys (Ni 50\AA /Ge 170\AA /Au 330\AA /Ni 150\AA /Au 3000\AA) (Figure 7(i)). The unwanted metals are lifted off by soaking in acetone

in the ultra-sonic bath and finally annealed (Figure 7(j)). The sample is then wire-bonded and is ready to be tested (Figure 8).

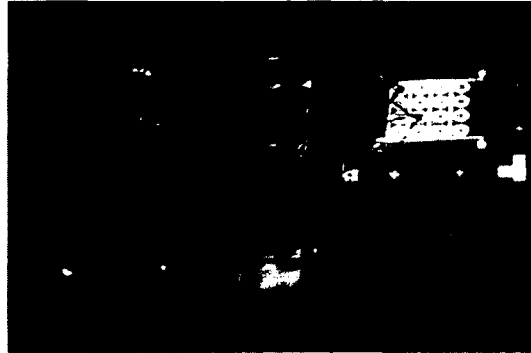


Figure 8 Mounted QDIP Sample

1.3. Characterization

Photoluminescence (PL) Measurement

Photoluminescence (PL) spectroscopy is a method for measuring the energy levels of the quantum dot. Usually, PL measurement is done after the MBE growth to determine if the MBE growth was successful.

The PL process begins with the excitation of electron-hole pairs (EHP) generated by a pump laser in the conduction and valance bands. The electrons and holes subsequently diffuse and are captured by QDs. The recombination of EHP to the ground states of QDs results in a re-emission of photons (photoluminescence) at a longer wavelength.

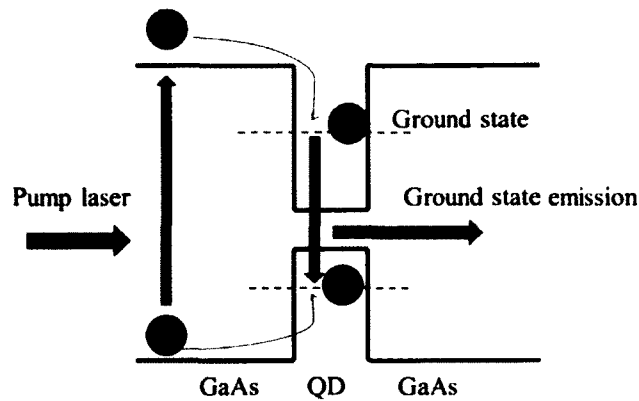


Figure 9 PL Measurement Band Diagram

The PL test of the QDIP sample was measured at room temperature by a continuous wave diode pumped solid state laser (DPSS) with excitation wavelength of 532nm. Laser output power is 200mW. The laser spot size was measured to be $\sim 0.5\text{mm}^2$. The chopper was used at frequency 500Hz to reduce $1/f$ noise. Liquid nitrogen cooled InGaAs detector was used to detect the re-emission signal.

Growth Characterization by XTEM and AFM

Cross-sectional transmission electron microscopy (XTEM) imaging is used to characterize the accuracy of the QDIP structure from the MBE growth. By knowing the physical size and dimension of QDs on each layer of the growth, one can determine and control the deposition parameter of MBE source accordingly to the structure. On Figure 10 and Figure 11, XTEM images of our QDIP were characterized by Evans Analytical Group (www.eaglabs.com). The images show the fine dimensions with the structure design the XTEM images show ten periods of absorption layer sandwiched between the top and bottom contact layers.

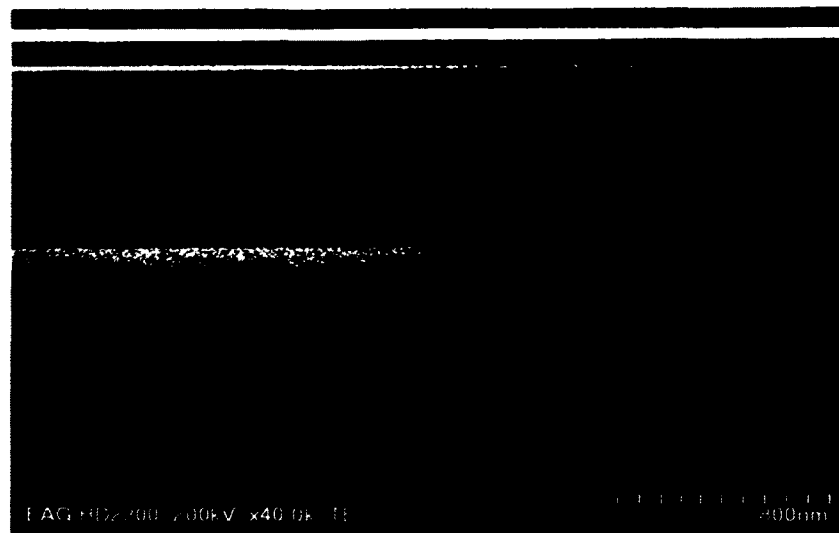


Figure 10 Example of XTEM Image on QDIP Sample



Figure 11 Example of XTEM Image on QDIP Sample Absorption Layer

AFM measurement characterizes the dot size and dot density on the surface of the QDIP sample. It is also helpful to determine the uniformity of the dot

across the entire area of the growth sample. AFM measurement is tested on the surface quantum dot grown on the sample. AFM images of QDIP sample are shown in Figure 12

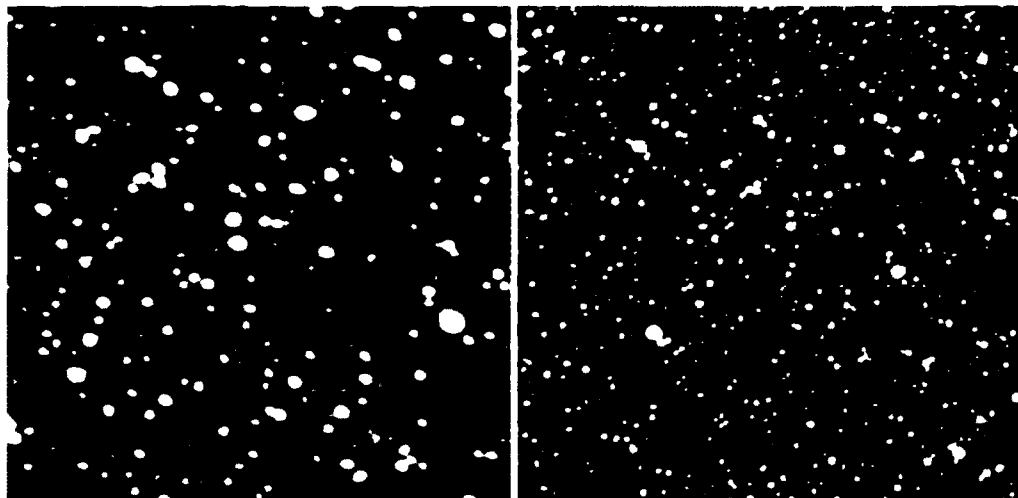


Figure 12 AFM Measurements, Left: 1μm by 1μm Area, Right: 2μm by 2μm Area

1.4. Figure of Merit

Fourier Transform Infrared (FTIR) measurement

Fourier transform infrared (FTIR) spectroscopy is a common technique to test the spectral response of the photodetector. A FTIR spectrometer consists of an infrared black body source, a 50% beam splitter, a fixed mirror, a movable mirror, and an IR detector. The brief principle of the FTIR spectrometer is explained below.

An IR beam is split by a 50% beam splitter. One beam travels to the fixed mirror and is reflected back. The other beam travels to the moveable mirror. Both beams reflect back to the beam splitter. The interference of the two reflected beams generates an

interferogram. Every data point of interferogram contains frequency information. The frequency information is obtained by the inverse Fourier transform.

In the spectral response test, the sample is secured in the cooling chamber (Janis, model No: ST-100) and connected to electrical wires in order to apply voltage to the sample. The chamber is placed into the FTIR body (Bruker, Tensor27) and aligned. The bias voltage is applied to the sample using the preamplifier (Stanford research systems, model SR570). During the test, a temperature controller (Lakeshore, 331 Temperature Controller) is connected to the chamber to adjust temperature.

Photocurrent and Photoresponsivity

Photocurrent is the current that flow through a QDIP device as a result of the black body radiation. Electron-hole pair absorbs energy from photon generated by the black body radiation. Then electron and hole flow through the device by the electrical field applied on the sample's electrodes.

Black body radiation causes by any object at any temperature above absolute zero. The radiation spectrum is different depending on the temperature of the object. At room temperature, black body emits mostly infrared wavelengths, however, as the temperature increases, black body starts to emit more visible light.

Figure 13 shows black body radiation spectrums at different temperatures.

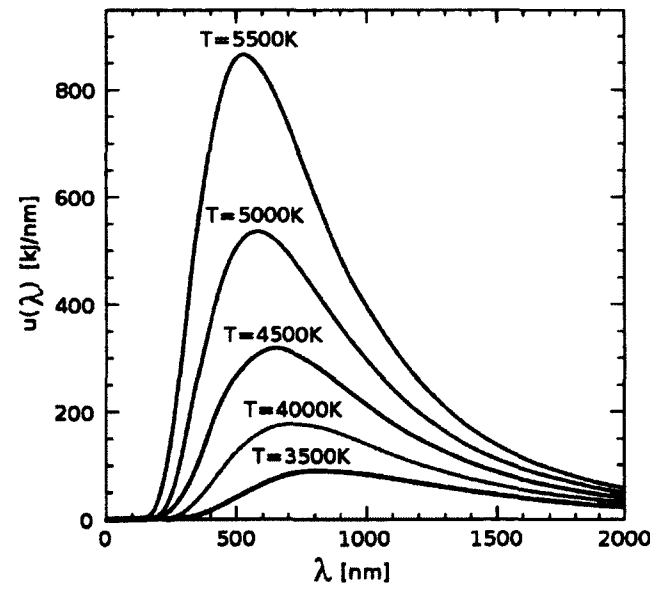


Figure 13 Black Body Radiations at Different Temperature

**Image from http://en.wikipedia.org/wiki/File:Wiens_law.svg. Author: GNU Free Documentation License*

In the photocurrent test, the black body (SBIR, Santa Barbara Infrared INC.) emits infrared light through the internal chopper at frequency 600 Hz. The modulated light passes through an optical filter (depending on wavelength selection, for example ISP optic, 1-25 μm , Transmittance = 60%) filtering the spectrum into the desired infrared band. Then the filtered light reaches the device in the chamber through ZnSe window (3-14 μm , Transmittance = 60%). The photocurrent generated in the device flows by electrical field set up by preamplifier. The photocurrent then flows to the preamplifier to amplify the signal and send out to the spectrum analyzer (Stanford research systems, model SR760 FFT spectrum analyzer). The spectrum analyzer reads the photocurrent at 600Hz in order to reduce the $1/f$ noise. The noise current will be collected at the same frequency in order to calculate the photoconductive gain.

Photoresponsivity

The Photoresponsivity (R) characterizes the performance of photodetector in term of photocurrent generated per incident optical power (I_{ph}) at specific wavelength range. The photoresponsivity of the QDIP can be calculated by:

$$R = \frac{\text{Photocurrent}(A)}{\text{Incident Optical Power}(W)} = \frac{I_{ph}}{P_0} \quad \text{Equation 2}$$

The incident optical power is the optical power from black body source that approaches to the photodetector surface, which can be calculated using a black body radiation calculator. The incident optical power depends on the opening area of the photodetector surface, solid angle in the test set up, photodetector pick-up wavelength and transmittance of optical filter, ZnSe window and photodetector itself.

Dark Current

Dark current is the main resource of the noise in QDIPs. Dark current is a small amount of current that flows through the photodetector in the dark circumstance.

For the dark current test set up, the chamber (Janis, model No: ST-100) is covered by foil so that no light exposes the photodetector. The chamber is cooled down with liquid nitrogen reach the temperature 77K. The temperature controller (Lakeshore, 331 Temperature Controller) is used to set up the appropriate temperature. The dark current (I_{dark}) is measured using Keithley 2602 System Sourcemeter with the LabTracer program. The sourcemeter applies bias into the QDIP and simultaneously collects the current. Then each of the current plots is plotted to generate I-V characteristics.

The dark current density of the QDIP can be calculated by:

$$J_{dark} = \frac{I_{dark}}{A} \quad \text{Equation 3}$$

where A is the opening area of the mesa

Noise current

Noise current is dark current test at specific frequency, in this case, approximately frequency 600Hz in order to avoid 1/f noise. The noise current test set up is as same as photocurrent but without the light source. The sample in the chamber, cooled down to temperature 77K, is connected with preamplifier. Preamplifier applies bias voltage into and collects the current from the QDIP. The preamplifier then amplifies current and sends the voltage signal to the spectrum analyzer. Spectrum analyzer records noise current over broad band frequency. Finally, the noise current at selected frequency is extracted from the records and plotted by varying the voltage bias.

Figure 14 shows the noise current for different bias voltages. Note that the 1/f noise dominates at a low frequency range. To avoid 1/f noise, the noise currents (i_{noise}) at high frequency (~600Hz) were measured.

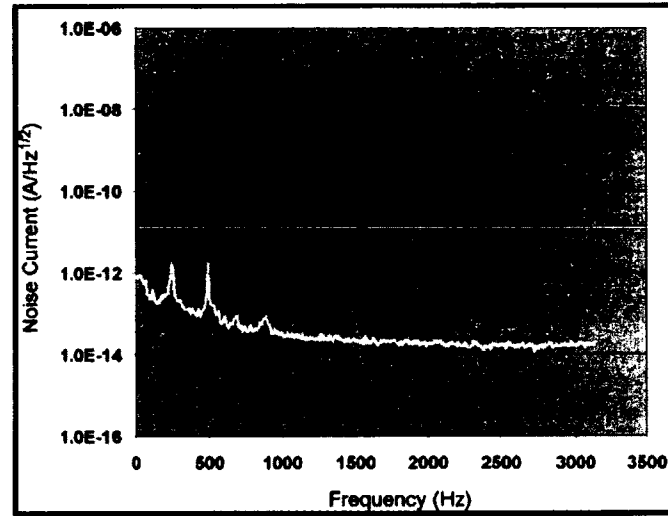


Figure 14 Noise Current Spectrums at Different Bias Voltages

Detectivity

Detectivity determines the capability of a photodetector to detect the weak signals. It is the sensitivity of the detector which normalized to 1 cm² area and 1 Hz of noise-equivalent bandwidth. A larger detectivity means a higher signal to noise ratio (SNR).

The detectivity (D^*) can be calculated by:

$$D^* = \frac{R\sqrt{A}}{i_{\text{noise}}} \quad \text{Equation 4}$$

where A is an opening area for the photodetector that expose to the IR radiation, and R is photoresponsivity.

2. Plasmonics Background

Plasmonics effect is the phenomena based on the interaction of near-field effect, which electrons on the surface of metal interact with the electromagnetic field of light. The metal media could be nanoparticles (with different size and shape or different structure of) or thin film. Such media has ability to optically induce the oscillation of free electrons at the metal surface. The resonance of surface electrons has been created and called surface plasmon. The famous example of plasmonics effect, in particular of metal nanoparticles, is the Lycurgus glass. The Lycurgus glass is a Roman glass caged cup which made by mixing ground gold and silver dust into glass thus formed colloidal nanoparticles in glass. The colloidal nanoparticles have formed in specific distance from each other so that it scatters the blue end of visible spectrum. As a result, the different color can be seen with different observation angle. The red color dominates when observed with transmitted light and the green color dominates with reflected light as shown in Figure 15 [17]. The early research of plasmonics field was reported from Mie [18] (small particles) and Richie [19] (flat interfaces). It brought much attention when Ebbesen [6, 20] claimed that the transmission profile of the plasmonics structure was greater than 100% compared with Bathe rule [21]. Since then, surface plasmon resonance has become popular on various kinds of application such as solar cell [22-25], sensor [26-28], antenna and collimator [29, 30], laser and diode [31-33].

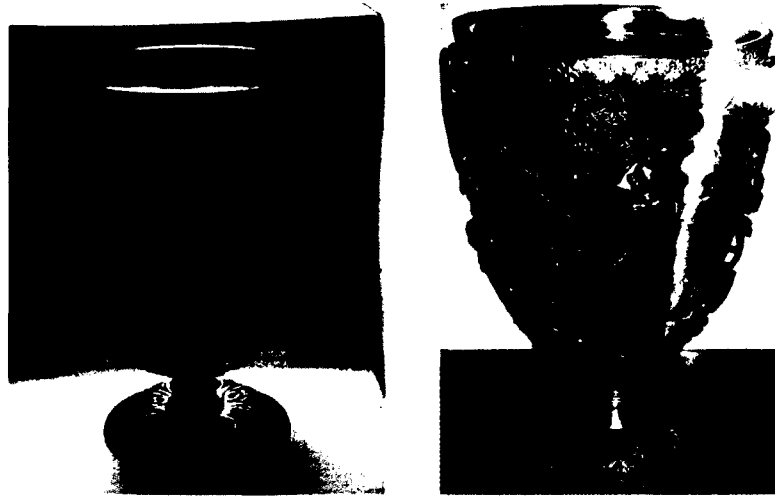


Figure 15 The Lycurgus Glass. Left side: Observed Transmitted Light. Right side: Observed Reflected Light. **Image from http://en.wikipedia.org/wiki/Lycurgus_Cup*

Plasmonics effect can be categorized into 2 groups depending on the effect of the excitation. The first is localized surface plasmon resonances (LSPR) which supports localized modes of the electromagnetic wave. The second is surface plasmon polaritons (SPP) which supports propagating modes.

Localized Surface Plasmon Resonances (LSPR)

In general, LSPR can be seen in metal nanoparticles. When light passes through metal nanoparticles, free electrons on particles surface interact with electric-field of incident light leading to the resonance of free electron on the metal surface thus induce a dipole moment on the particle itself. When the particle size is smaller than the wavelength, the quasi-static analysis can be derived to the following formula for the particle polarizability (α) [34]

$$\alpha = 4\pi a^3 \frac{\epsilon_m - \epsilon_d}{\epsilon_m + 2\epsilon_d}$$

Equation 5

where ϵ_m is the dielectric constant of metal in the function of wavelength,

ϵ_d is the dielectric constant of the surrounding medium

a is the radius of the particle

Since the metal dielectric constant (ϵ_m) varies with wavelength, the particle polarizability (α) also varies with wavelength. The more polarize in particle leads to the stronger of electrons resonance. The key to reach maximum particle polarizability (α) is to minimize the denominator of particle polarizability on equation 5. In visible regime, it is possible to cancel out the real part of the denominator by choosing the dielectric constant of surrounding medium to match with the correct metal at the specific wavelength. In other words, the dielectric constant of surrounding medium has to match with the dielectric constant of the metal. For example, the regular laboratory glass has refractive index (n) of 1.5 in the visible regime which equal to dielectric constant $\epsilon_d = n^2 = 2.25$. So the minimum denominator come from $\text{Re}(\epsilon_m) = -4.5$ which approximately corresponds to silver(Ag) at 420nm, gold(Au) at 520nm, and copper(Cu) at 470nm [35, 36]. The imaginary part of the denominator is associated with Ohmic heating losses in the particle [12]. The lower the imaginary value, the less loss there will be, thus an increase in resonance. The resonance wavelength of LSPR can be tuned by various parameters such as particle size, particle shape, metal type, and surrounding medium. The applications of LSPR lies on various fields such as molecular detector (Surface-enhanced Raman Scattering), semiconductor (Thin-film solar cell), and optical device (light-emitting diodes)

Surface Plasmon Polaritons (SPP)

SPP occurs on the flat metal surface. Compared with LSPR, SPP is created at the interface between metal and surrounding medium and the electromagnetics wave constructed at the surface may propagate. By applying the boundary condition on the Helmholtz equation and reviewing the solution for propagating wave at the interface, the surface plasmon wave vector can be yielded [37, 38]

$$k_{SPP} = k_0 \sqrt{\frac{\epsilon_m \epsilon_d}{\epsilon_m + \epsilon_d}} \quad \text{Equation 6}$$

where k_{SPP} is the wave vector of surface plasmon, k_0 is the wave vector in free space, ϵ_m is the dielectric constant of metal in the function of wavelength, ϵ_d is the dielectric constant of the surrounding medium.

Providing $k_0 = \frac{\omega}{c}$, one can draw dispersion curve of SPP compared with the dispersion curve of light line.

III. PRELIMINARY RESULT (PLASMONICS ENHANCED QDIP)

1. Initial Test and Design

The sub-wavelength hole array has been a popular topic and extensively researched [6-11, 39]. The effect of surface plasmon has been demonstrated in the visible regime with metallic hole arrays [13]. However, there are limited reports that address the effect in the infrared regime. In this section, the two dimensional metallic hole array is fabricated on GaAs wafer double-side polished. The transmission profiles will be tested to verify the surface plasmon phenomena.

In this section, the thickness of gold thin film is 25nm. Several periods are chosen from 2.6 μ m to 6.0 μ m with 50% filling factor. The image of metallic holes array is shown in Figure 16 and Figure 17. The transmission profile is also shown in Figure 18.



Figure 16 SP Metallic Hole Array (6 μ m period)

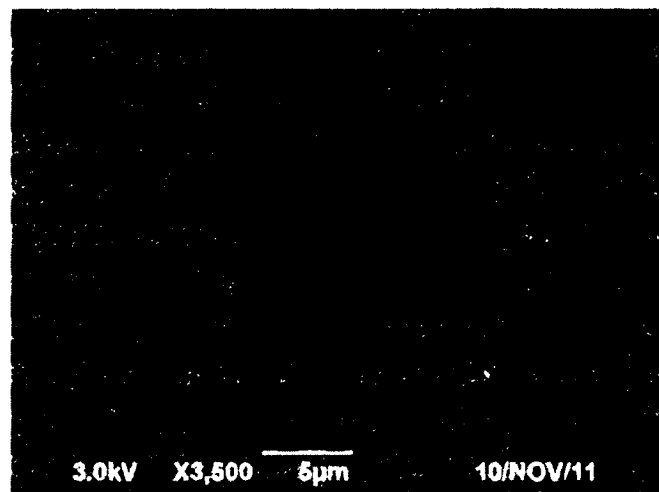


Figure 17 SP Metallic Hole Array (2.6 μ m period) (SEM)

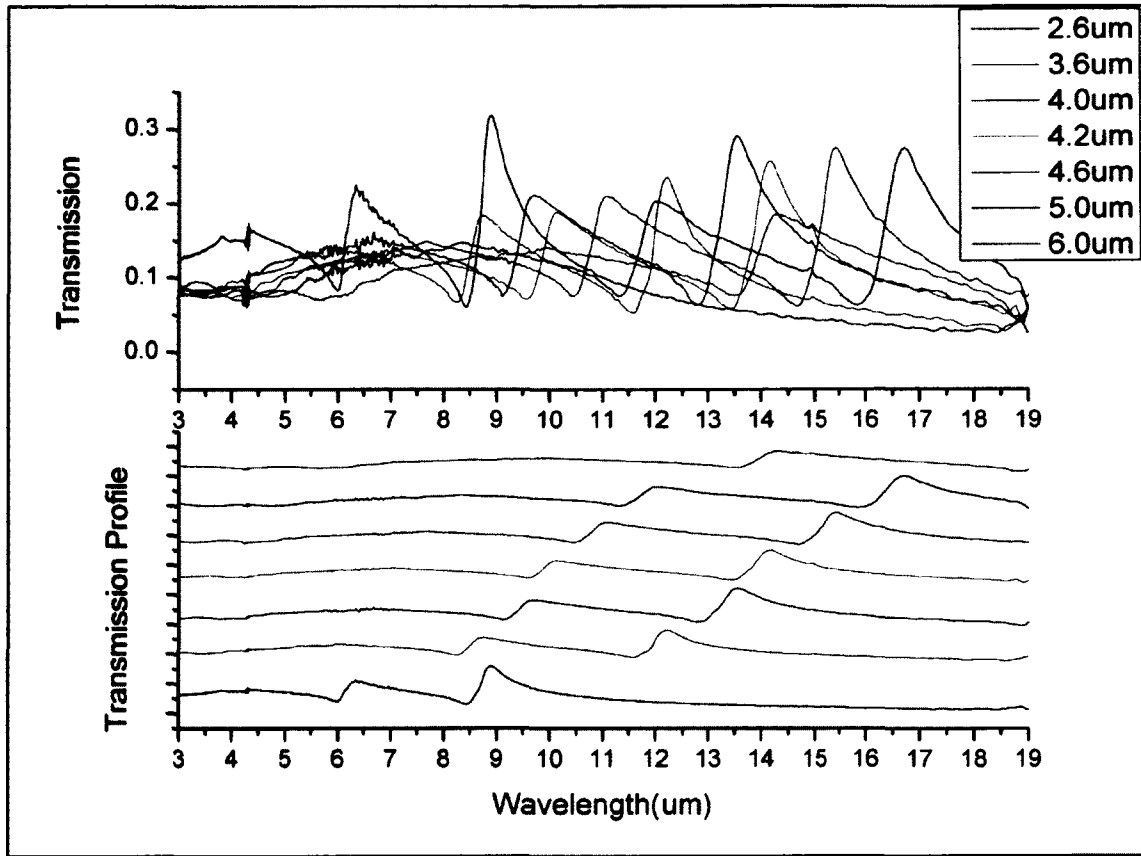


Figure 18 Transmission Profile1 of SP Sample on GaAs

From Figure 18, the result exhibits the peak position changing with period. For 2.6um period, the peak position is at 8.8um. For 3.6um, the peak position is at 12.1um. Since the QDIP device operates at MWIR and LWIR, the specific periods are chosen from 2.2um to 3.0um in order to observe the surface plasmon phenomena at MWIR and LWIR. The metallic hole arrays from 2.2um to 3.0um period were fabricate and tested again for the transmission profiles. For the result, the transmission peak positions are seen at 7.8um to 10.2um correspondingly. Figure 19 shows the transmission profile of metallic hole arrays from the period of 2.2um to 3.0um.

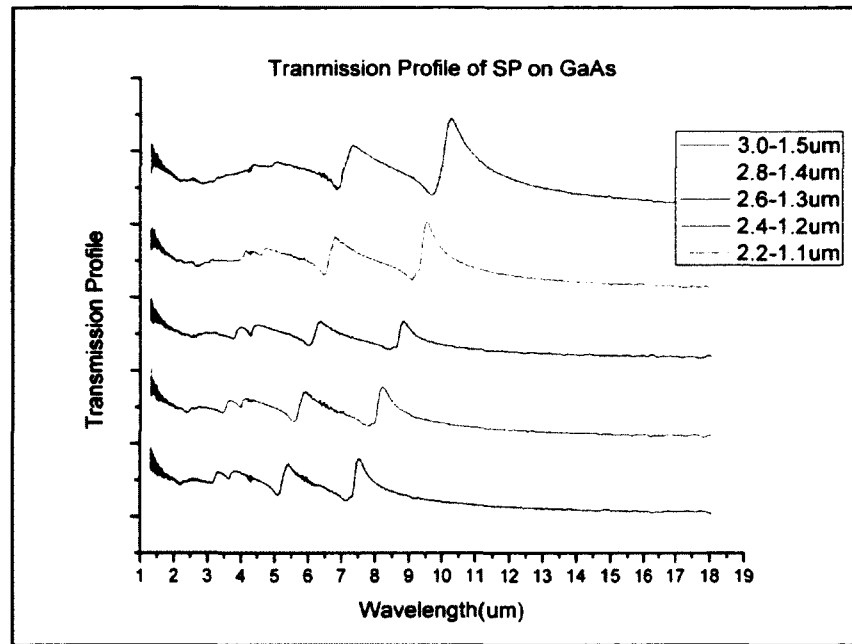


Figure 19 Transmission Profile2 of SP Sample on GaAs

After the transmission profiles are observed, the relation between the peak and dip wavelength and period size are derived for later application to match our QDIP absorption wavelength region. Figure 20 represents the relationship between the peak and dip position and period size.

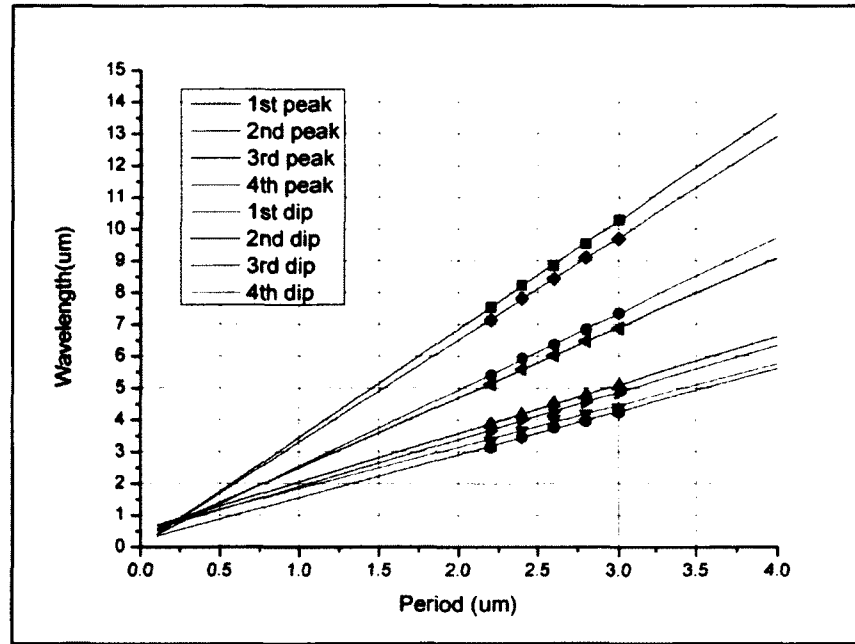


Figure 20 Relationship Between the Peak & Dip Position and Period Size

2. Verification Experiment

This section will discuss the figures of merit, all parameters and performance of the detector after we have integrated surface plasmon structure together with the QDIP. The main idea is to employ the plasmonic structure that interacts with light so that it creates resonance on dielectric-metal interface. The strong electromagnetic field on GaAs-Au interface will induce the photon absorption which leads to increasing photocurrent. Similar as this thesis, the focus in this section will be on the performance enhancement of QDIP by surface plasmon structure.

Device characterization (UML167)

The QDIP sample (#UML167) is grown by using a V80H molecular beam epitaxy (MBE) system. A 0.3 μm Si-doped (n+) GaAs contact layer ($n = 1 \times 10^{18} \text{cm}^{-3}$) is first grown on a semi-insulating GaAs (100) wafer, followed by the growth of a 0.1 μm undoped GaAs buffer layer. The growth temperature for the GaAs contact and buffer layers is 580 $^{\circ}\text{C}$. The active region of the QDIP consists of ten periods of QD heterostructures. Each period of the QD heterostructures consists of 1 nm $\text{In}_{0.15}\text{Ga}_{0.85}\text{As}$ followed by 2 monolayers (ML) of InAs QDs, 1 nm $\text{In}_{0.15}\text{Ga}_{0.85}\text{As}$ cap layer and 50nm GaAs spacer layer. The doping level of the QD region is tuned to be approximately 5 electrons/dot. The QD layers and the $\text{In}_{0.15}\text{Ga}_{0.85}\text{As}$ cap layers are grown at 485 $^{\circ}\text{C}$. The top contact layer is 0.1 μm Si-doped ($n=1 \times 10^{18} \text{cm}^{-3}$) GaAs layer. After the growth, the wafer is then processed into 250 μm -diameter circular mesas with top and bottom electrodes using standard photo-lithography, wet etching procedures, E-beam metal evaporation deposition, lift-off and thermal annealing processes [15]. The metallic two dimension holes array (2DSHA) structure is finally fabricated on top of the QDIP mesa using standard photo-lithography, E-beam metal deposition, and lift-off processes. The thickness of the deposited Au film is 25 nm. The QDIP with the top 2DSHA structure is referred to as QDIP-2DSHA. A QDIP is also made without the 2DSHA structure for reference (referred to as Ref-QDIP)

The top views of the QDIP with the metallic 2DSHA are shown in Figure 21 and Figure 22. The 2DSHA is a square lattice with the lattice constant $a = 2.6 \mu\text{m}$. The diameter of the hole is $d = 1.3 \mu\text{m}$. The same type of 2DSHA structure is also made on a bare GaAs wafer for reference purposes (referred to as Ref-2DSHA).

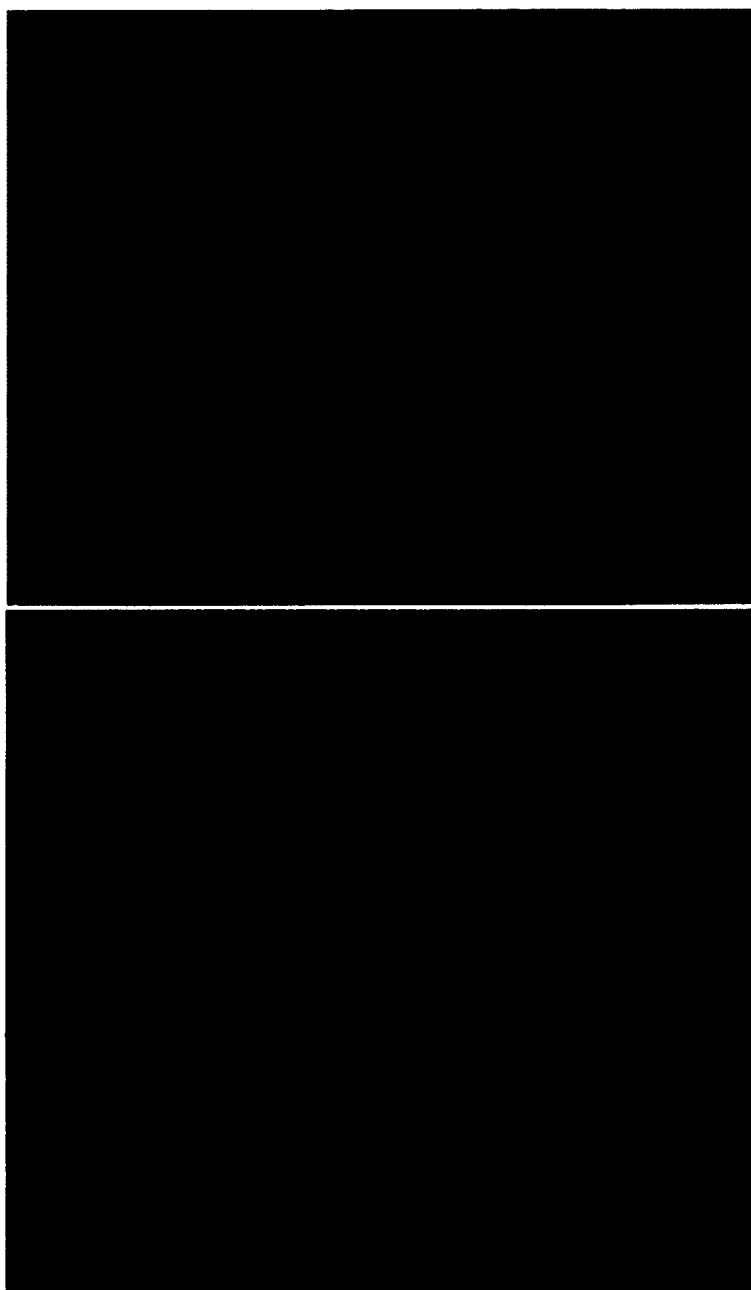


Figure 21 2DSHA on QDIP (Optical Microscope)

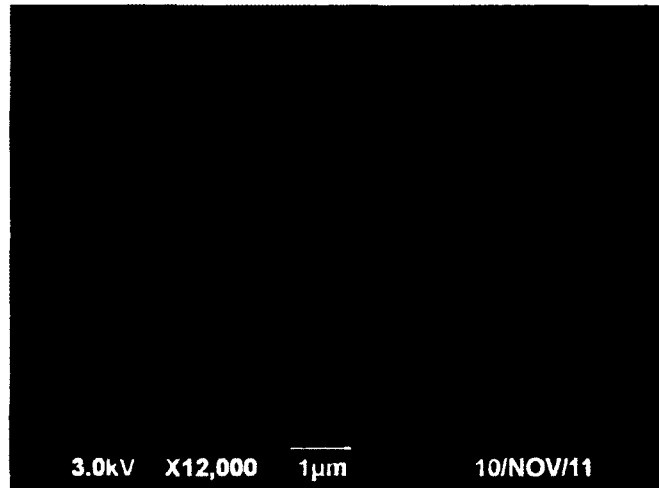


Figure 22 2DSHA on QDIP (SEM)

Result and Discussion

Figure 23 (a) shows the FTIR transmission spectrum of the Ref-2DSHA at the sample temperature of 77 K. It shows a narrower plasmonics resonance peak at 8.9 μm and a broader plasmonics resonance peak at 6.4 μm . It also shows two dips at 8.3 μm and 5.9 μm . Figure 23 (b) shows the FTIR photocurrent spectrum of the QDIP-2DSHA (pink trace) and the Ref-QDIP (blue trace) measured at 77 K. The FTIR spectrum of the QDIP-2DSHA and the Ref-QDIP samples are measured using the same pre-amplifier sensitivity and plotted on the same scale. The photocurrent spectrum of the QDIP-2DSHA (pink trace) shows slight enhancement at $\sim 5.9 \mu\text{m}$ wavelength region and over 200% enhancement at 8-9 μm wavelength regions. Note that the photocurrent enhancement wavelengths shift away from the plasmonics resonant peaks at 8.9 μm and 6.4 μm and correspond to the dips at 8.3 μm and 5.9 μm in the FTIR transmission spectrum of the Ref-2DSHA. The dips in the transmission spectrum of 2DSHA structures have been reported and are attributed to the Fano-type interference between the discrete

plasmonics resonance and the radiative damping of plasmon due to the surface plasmon scattering on the hole arrays [8, 11, 20, 37, 39]. The dips are referred to as Fano dips, at which wavelength the strongest localized field at the holes can be found [11, 39]. Due to the strong optical field localization, the intensity of emission light is at the minimum. The strong field localization effect may cause photocurrent enhancements. This qualitatively explains the reason the photocurrent enhancement wavelengths correspond to the Fano dips. The significantly higher photocurrent enhancement at 8.3 μm (mode 01 or 10) than at 5.9 μm (mode 11) is possibly due to the higher diffraction efficiency for lower order plasmonics mode and thus stronger localization effect [37].

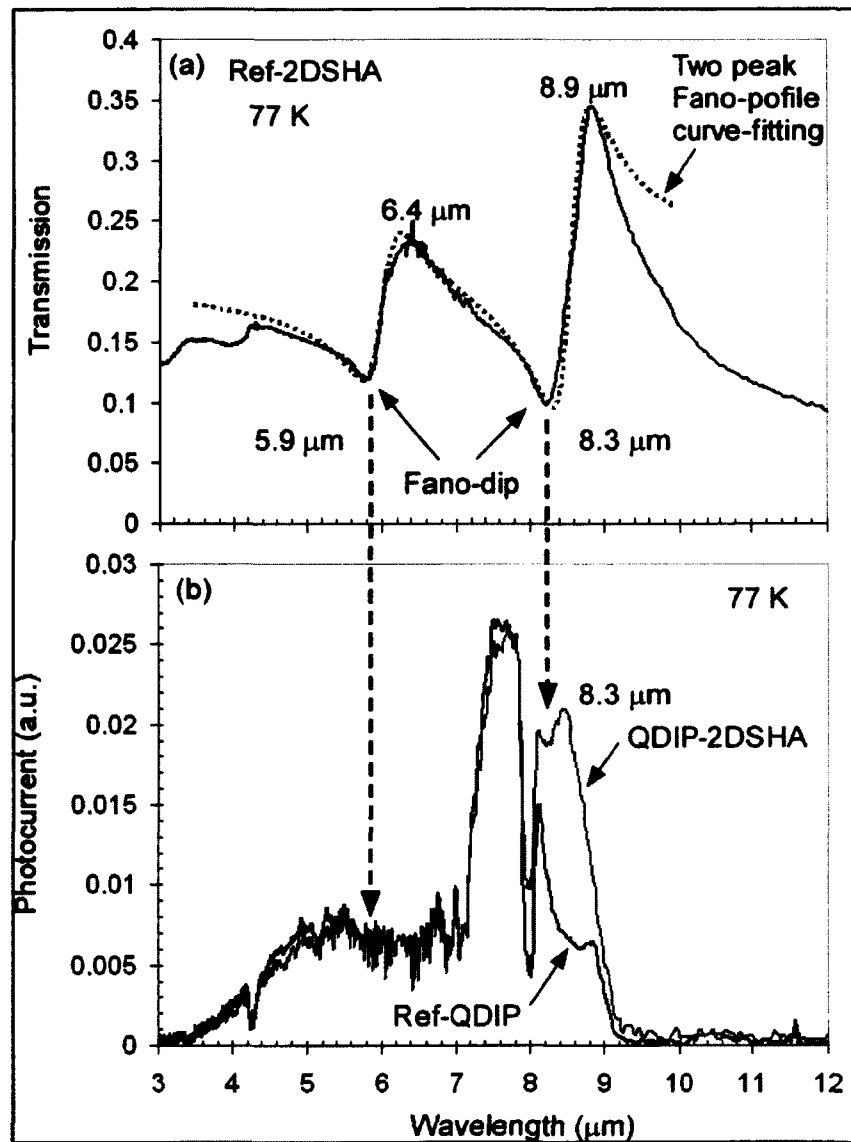


Figure 23 Spectral Response and Transmission Profile Comparison

Further analysis is performed to verify the Fano-type interference in the 2DSHA structure. The two transmission peaks at 8.9 μm and 6.4 μm correspond to the first plasmonics mode01 or mode10 and the second plasmonics model1, respectively [7, 40]. Following Genet *et al* in [39], the transmission of the Fano-type interference can be written as:

$$T = |t_B|^2 \frac{[\varepsilon + q]^2}{\varepsilon^2 + 1}, \quad \text{Equation 7}$$

where, t_B is the transmission coefficient of direct non-resonant (background) transition, ε is a dimension less parameter which can be expressed as [39]:

$$\varepsilon = \frac{E - (E_{sp} + \hbar\Delta)}{\hbar\Gamma/2}, \quad \text{Equation 8}$$

where, E_{sp} is the resonant energy, Γ is the line width, Δ is the resonant shift, and $q = 2\delta/\Gamma$, δ is the ratio between the resonant transition amplitude and non-resonant transition amplitude. For a two peak Fano-type transmission, the total transmission can be written as a superposition of the two Fano-type transmissions:

$$T = |t_{B1}|^2 \frac{[\varepsilon_1 + q_1]^2}{\varepsilon_1^2 + 1} + |t_{B2}|^2 \frac{[\varepsilon_2 + q_2]^2}{\varepsilon_2^2 + 1}, \quad \text{Equation 9}$$

The red-dashed line in Figure 23 (a) shows the curve fitting of the two peak Fano-type transmission using Equation 9. The transmission profile agrees well with the experiment FTIR transmission spectrum of the Ref-2DSHA, which verifies that the transmission of the Ref-2DSHA is due to the Fano-type interference. This analysis shows that the strong field localization effect leads to photocurrent enhancement at the Fano-dips.

Figure 24 shows the noise current (i_{noise}) of the QDIP-2DSHA and the Ref-QDIP at different biases at the sample temperature of 77 K. Both samples show similar noise

current levels, indicating the top 2DSHA structure does not introduce any significant noise current [41].

The Responsivity of the QDIP is measured using a (1000 K) calibrated blackbody source [15] and 7.5 μm long pass filter is used to ensure the collected IR signal are from the LWIR-band. Figure 25 shows the measured responsivity of the QDIP-2DSHA and the Ref-QDIP on different biases at 77 K. The responsivity of the QDIP-2DSHA shows over 200% enhancement at all biases. Detectivity enhancement of over 200% by the 2DSHA is achieved (Figure 26). A peak Detectivity of $5.0 \times 10^8 \text{ cmHz}^{1/2}/\text{W}$ is obtained at a bias of -1.0 V at 77 K.

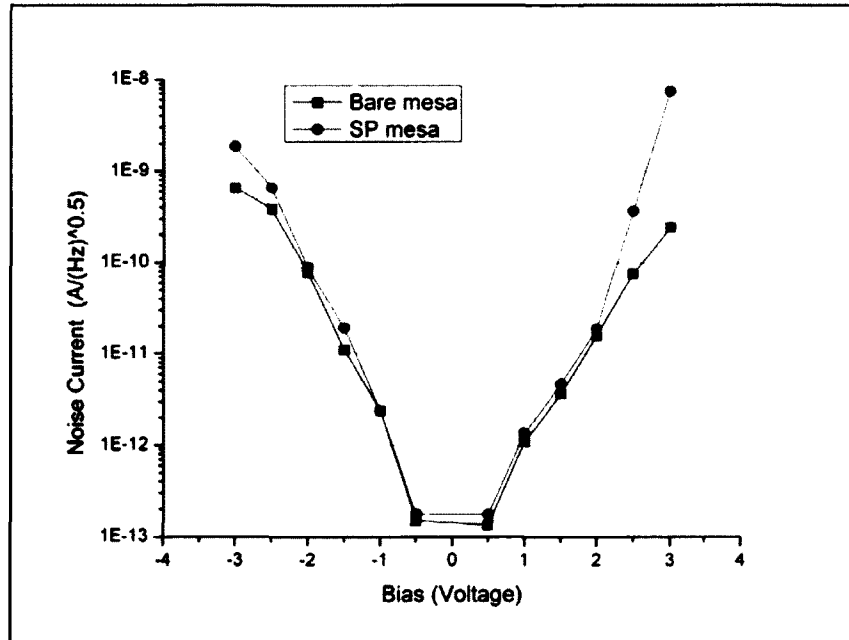


Figure 24 Noise Current Comparisons

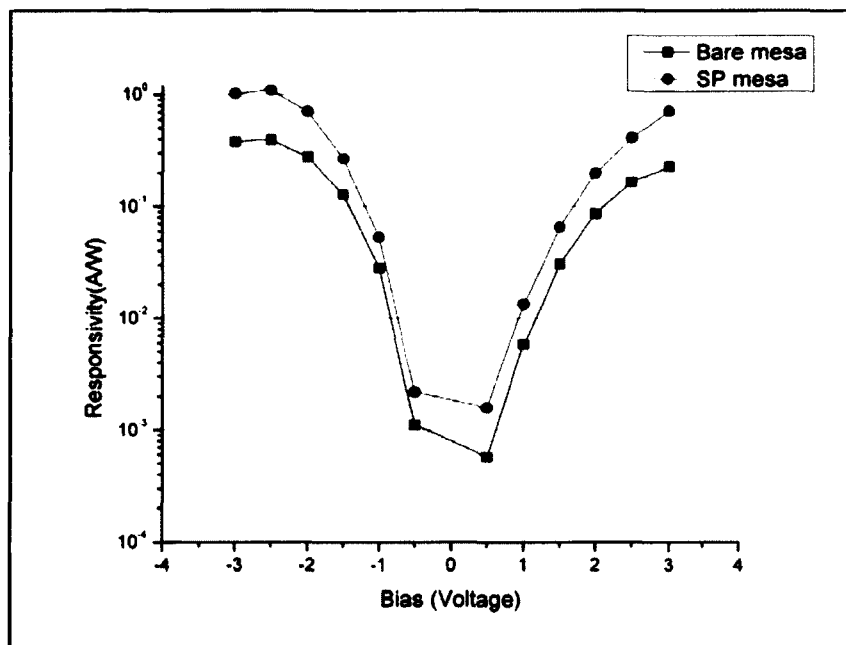


Figure 25 Responsivity Comparison

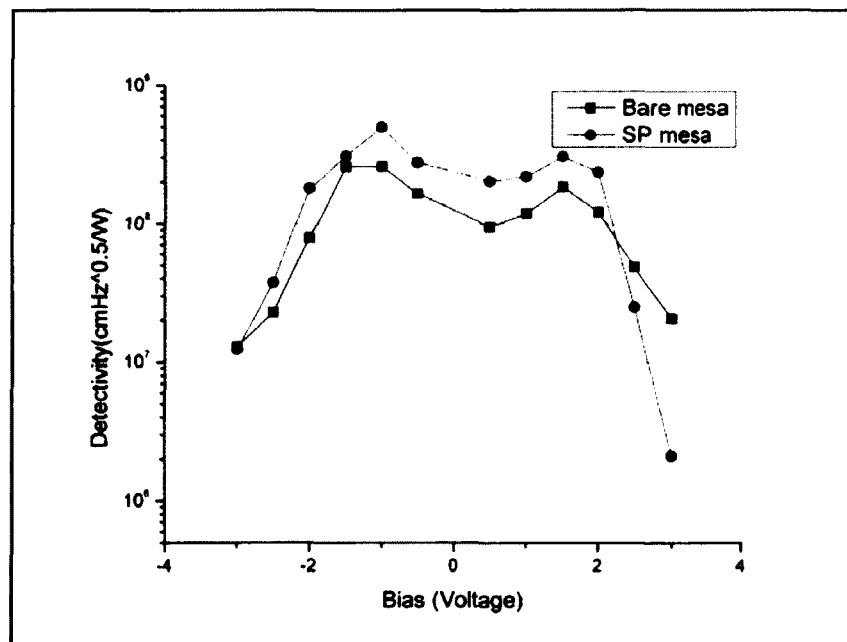


Figure 26 Detectivity Comparison

3. Further Investigation

In this section, several alternative parameters involving in surface plasmon effect have also been investigated. The transmission profiles are recorded. Considered the most benefit to the QDIP performance, subjects from this section will be selected and used for experiments in the following chapters.

3.1. Lattice Alignment

In the visible regime, metallic nanoparticles have shown the resonant wavelength shift with different particle shapes [42, 43]. The wavelength shift is due to the retardation effect on the particle. It is also possible to observe the resonant wavelength shift of metallic thin film hole array by designing the different lattice alignment. Figure 27 shows the transmission of hexagonal lattice holes array and square lattice holes array. Both samples have 2.6 μm period and 1.3 μm circular holes diameter. From Figure 27, SP square structure has 2 plasmonics modes, which are mode01 and mode11, while SP hexagonal structure has only 1 plasmonics mode, which is mode01. The peak and dip of transmission profile are also in the different position. Figure 28 shows the pictures of hexagonal lattice hole array and square lattice hole array.

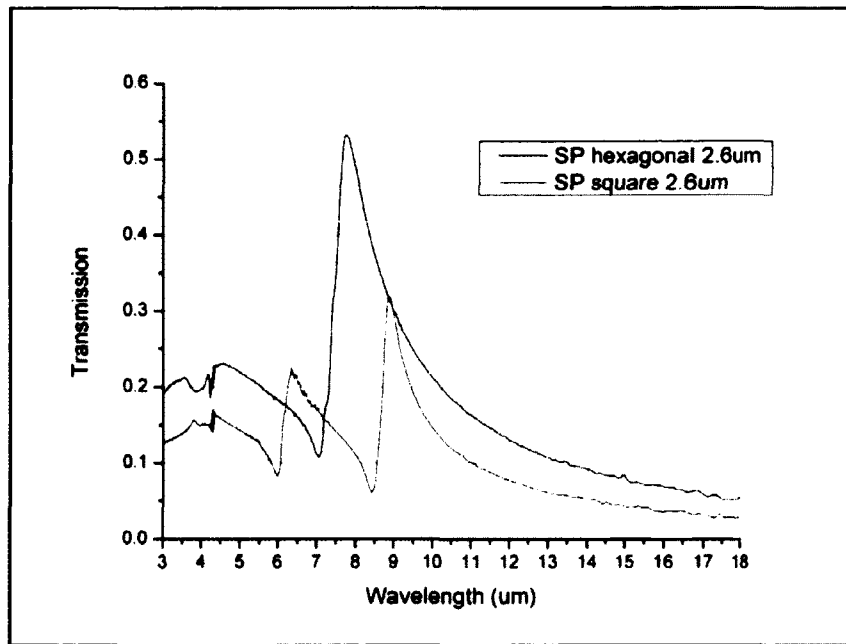


Figure 27 Transmission Profile of SP (Square vs Hexagonal Array)

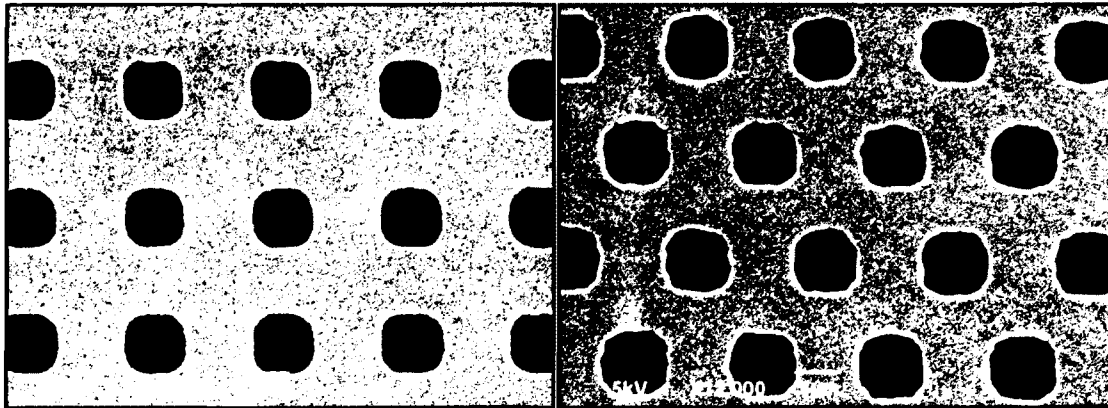


Figure 28 Hexagonal Lattice Hole Array and Square Lattice Hole Array

3.2. Polarization Selection

The sensitivity of polarization is investigated in this experiment. With SP square pattern 2.6um and 3.0um, the combination of both patterns into one structure, which x-

axis contains SP 2.6 μm period and y-axis contains SP 3.0 μm period, is attempted. Figure 29 shows the SEM picture of 2.6x-3.0y-1.3 μm sample on GaAs. Figure 30 exhibits the polarization in function of the geometry of surface plasmon structure. The transmission profile of SP 2.6x-3.0y mimics one peak (at 8.7 μm) of SP 2.6 μm structure and one peak (at 10.1 μm) of SP 3.0 μm structure. Moreover, the third plasmonics mode of SP 2.6x-3.0y peak is in between the peaks of SP 2.6 μm and SP 3.0 μm structure.

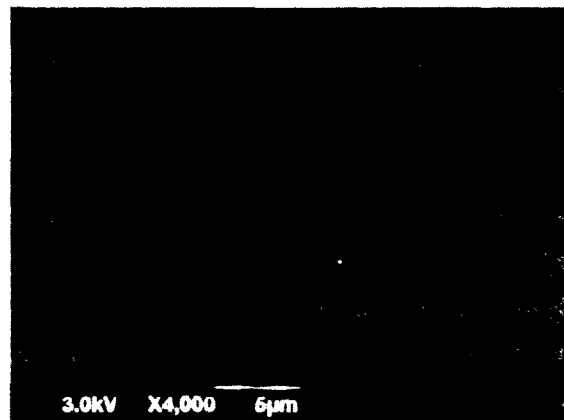


Figure 29 2.6x-3.0y-1.3 μm Sample

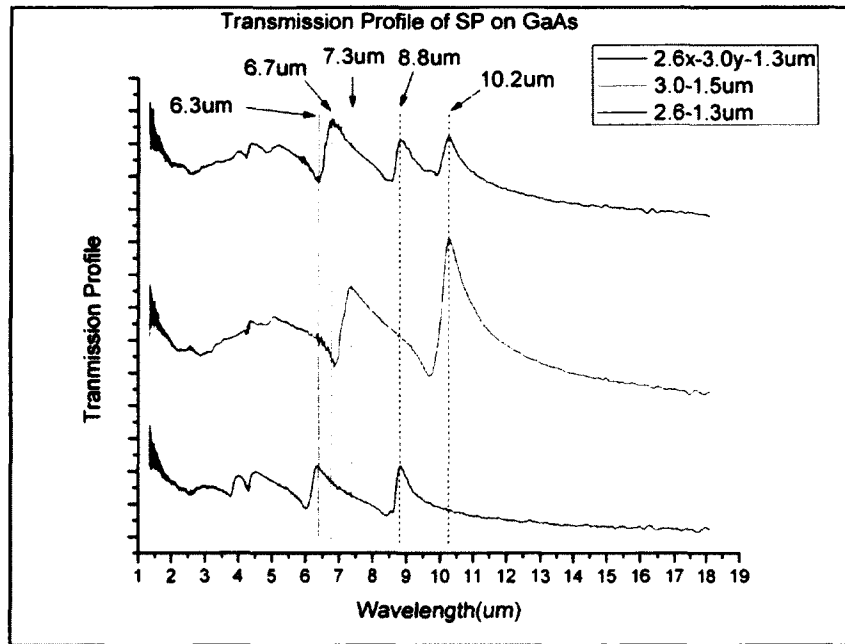


Figure 30 2.6x-3.0y-1.3um Sample Transmission Profile

Furthermore, the polarization selection of SP 2.6x-3.0y structure is tested. By placing the polarizer in front of the sample, the transmission profile exhibits the difference between 0 degree, 45 degree and 90 degree. Defined the first plasmonics mode peak is at 10.2um and the second mode peak is at 8.8um. With 0 degree polarization, the first mode exists but the second mode clearly disappears. On the other hand, 90 degree polarization exhibits the second mode but the first mode vanishes. For polarizations in between, 45 degree polarization, both modes are present but the transmission peaks are weaker than the peak at 0 degree and 90 degree polarization.

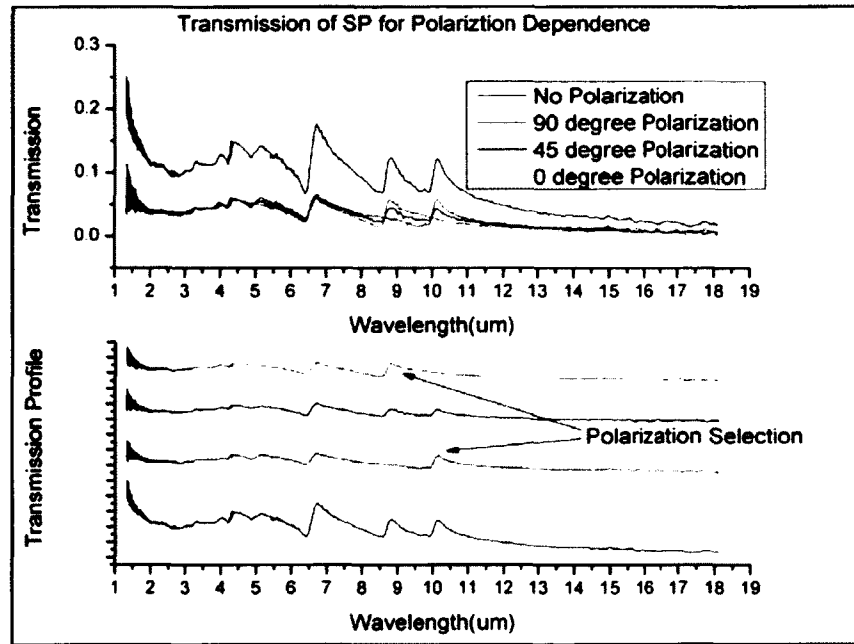


Figure 31 Transmission of 2.6x-3.0y-1.3um Sample for Polarization Selection

3.3. Hole Size Variation

The hole size of the plasmonics structure is one crucial parameter to determine the transmission intensity suggested by Bethe rule [21]. It is worth studying the enhancement of plasmonics structure with varying hole sizes on the QDIP to optimize the maximum enhancement. Figure 32 shows the transmission profile on each hole size from 1.1um to 1.7um of 2.6um period plasmonics structure. On each profile, the peak and dip locations are at the same position. However, the transmission intensity is increased with the hole size, which agrees with Bethe rule [21].

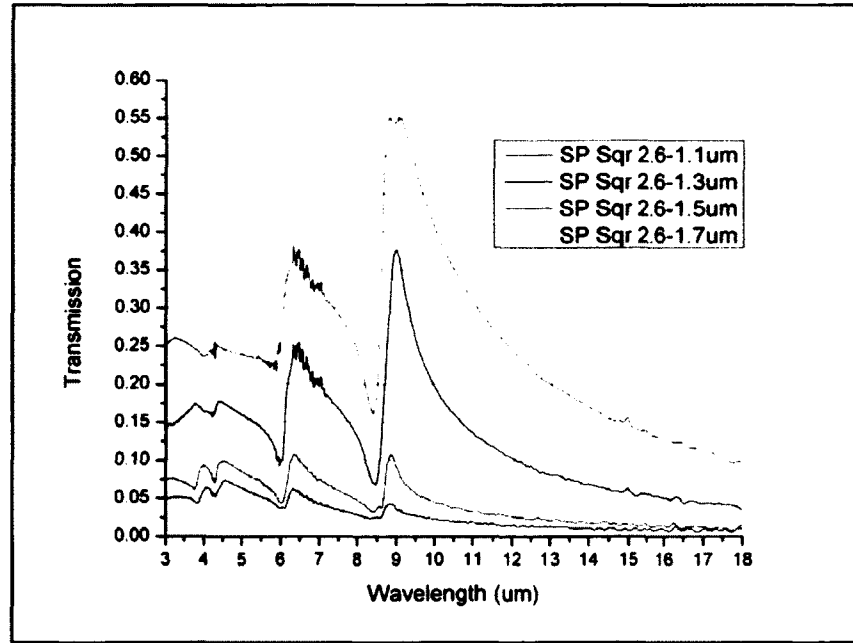


Figure 32 Transmission of SP Varied Hole Size

3.4. Metal Thickness Variation

With Wood's anomaly [44], it is suggested that the thickness of the metal could play the role on the dark spot of spectrum from metal grating due to the light traveling along surface of the metal. The metal thickness could also affect the transmission profile of surface plasmon structure as well. With this hypothesis, the samples of surface plasmon structure (Au) with 3 different thicknesses, 25nm, 50nm and 100nm are fabricated and tested for transmission measurement. Figure 33 shows the transmission profile of SP 2.6x-3.0y structure with varying metallic thicknesses. The bandwidth is measured and reported on Table 1 and Table 2. With the full width 75% maximum on Table 2, it strongly shows that the bandwidth decreases with an increased gold thickness.

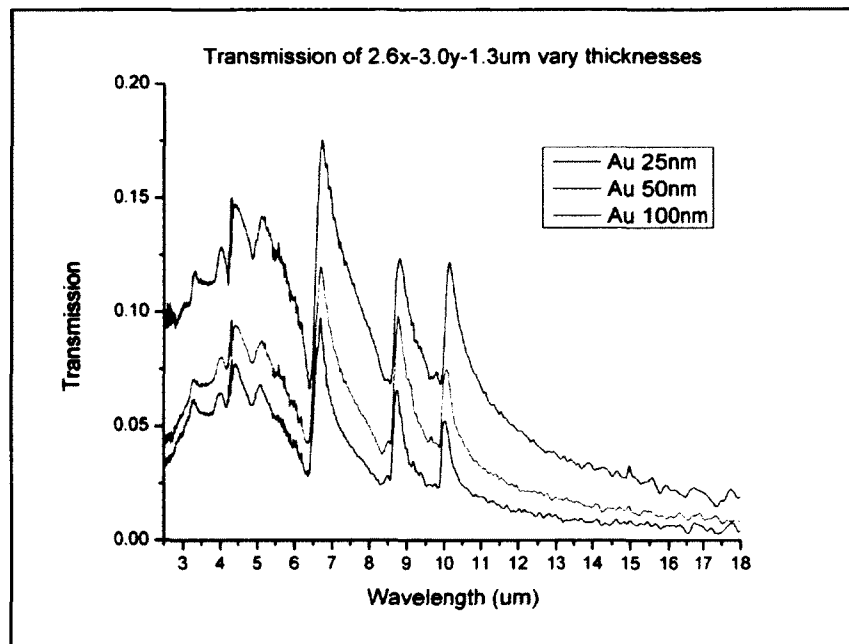


Figure 33 Transmission of SP with Different Metal Thickness.

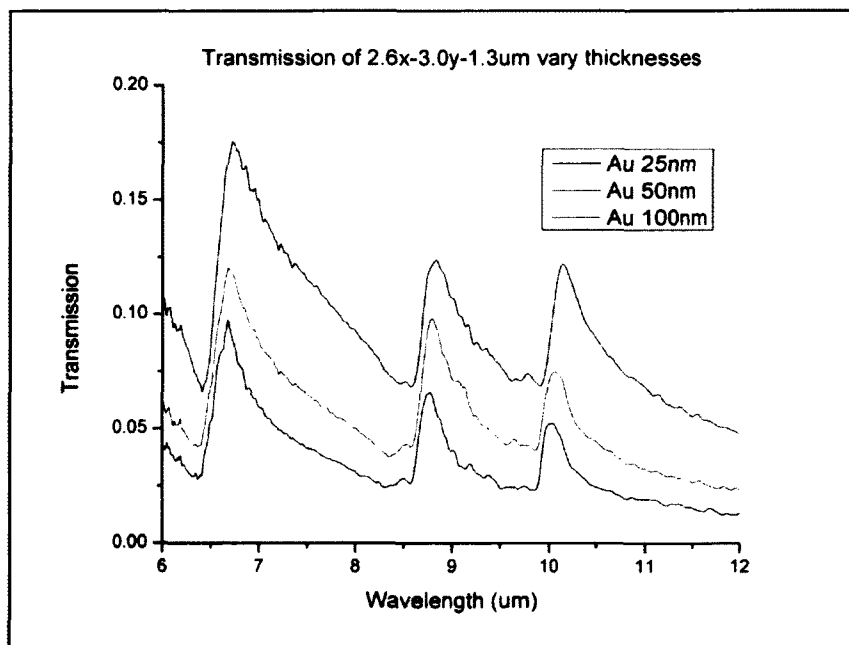


Figure 34 Transmission of SP Varied Metal Thickness (Zoom in).

FWHM(um)	peak3	peak2	peak1
Au 25nm	1.591		
Au 50nm	1.172	0.783	
Au 100nm	0.76	0.515	0.538

Table 1 FWHM (um) of SP Transmission Varied Metal Thickness.

FW75%M(um)	peak3	peak2	peak1
Au 25nm	0.603	0.523	0.444
Au 50nm	0.423	0.302	0.314
Au 100nm	0.286	0.252	0.254

Table 2 FW75%M (um) of SP Transmission Varied Metal Thickness.

3.5. Metal Selection

Metal selection experiment is conducted to seek an alternative material, other than gold, to apply on the plasmonics structure and to understand the Ohmic loss associated with the imaginary part of the dielectric constant of metal.

From chapter II section 2) Plasmonics background, the wave vector of surface plasmon wave is complex number. The imaginary part of the wave vector determines internal absorption which can be seen as loss. In this topic, we select 4 metals to examine which are gold (Au), silver (Ag), cobalt (Co), and titanium (Ti). The dielectric constant of each metal is shown in Table 3.

	Gold (Au)	Silver (Ag)	Cobalt (Co)	Titanium (Ti)
Dielectric Constant	-5050+i1090	-5140+i749	-820+i419	-281+i290

Table 3 Dielectric Constant of Metals

Gold (Au), silver (Ag), cobalt (Co), and titanium (Ti) are fabricated on GaAs and then the transmission profiles are measured. The results are shown in Figure 35. Gold and silver clearly show the peak and dip on the transmission profile while cobalt has shallower peak and dip. Titanium does not exhibit any significant change on transmission compare to bare GaAs wafer. Since silver demonstrates similar transmission profile, it has a potential to substitute gold for the fabrication of plasmonics structure.

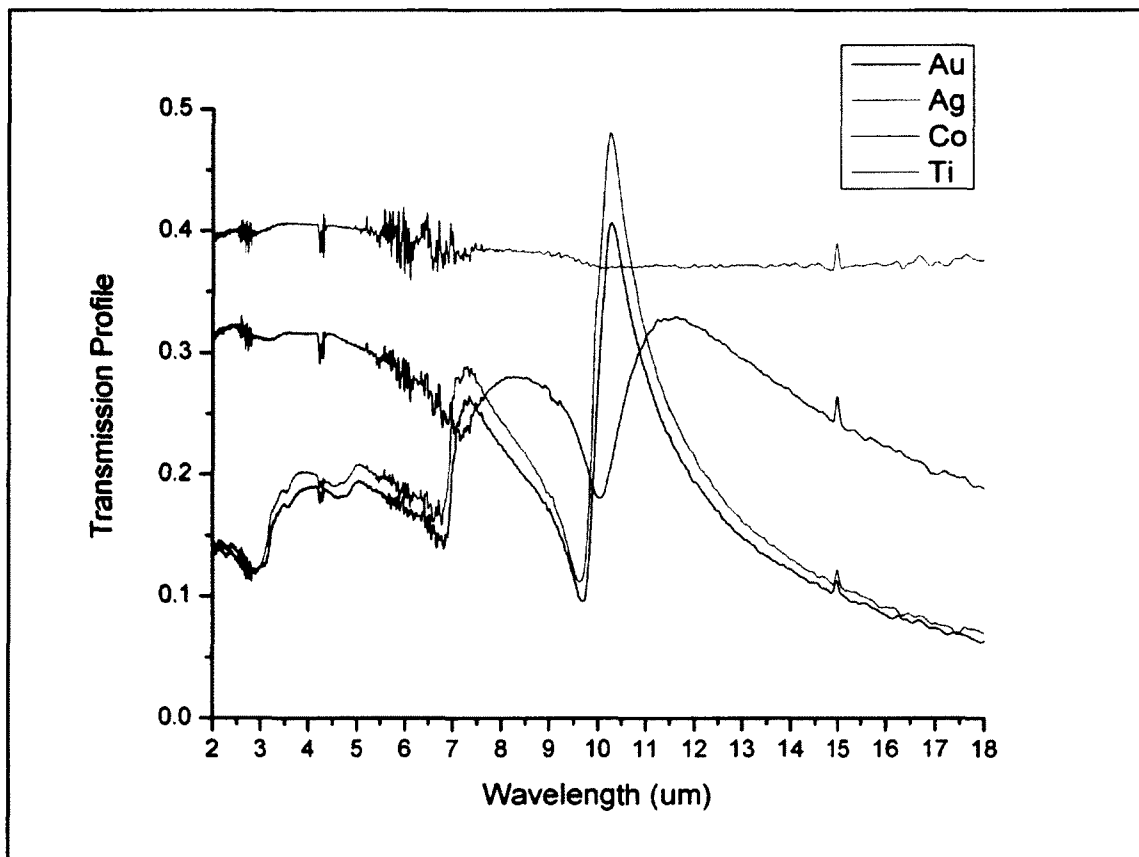


Figure 35 Transmission Profile of Gold (Au), Silver (Ag), Cobalt (Co), and Titanium (Ti)

It is also can be seen here, from Table 3, the dielectric constant ratio of real part and imaginary part of gold and silver are approximately the same around 5:1 ratio, while

cobalt is at 2:1 and Titanium is at 1:1. These ratios play a role on equation 6. When substitute dielectric constant of each metal into equation 6, we get

$$k_{SPP-Au} = k_0(3.30340 + 0.00074i)$$

$$k_{SPP-Ag} = k_0(3.30343 + 0.00050i)$$

$$k_{SPP-Co} = k_0(3.31748 + 0.00902i)$$

$$k_{SPP-Ti} = k_0(3.33092 + 0.03287i)$$

From the wave vector of each metal, gold and silver have small imaginary part while cobalt and titanium has approximately 13 times and 47 times larger than that of gold. Considering the imaginary part of wave vector determines an internal absorption, silver is found to be an alternative metal apart from gold.

The silver plasmonics structure was then fabricated on sample UML302. Figure 36 show the spectrum response of UML302 bare mesa and silver plasmonics mesa. The enhancement wavelength and curve is similar to that of gold plasmonics mesa in Figure 23. Figure 37 shows the spectrum response and enhancement ratio of UML302SP (Ag). The enhancement peak is around 2.5 times which also relatively approximate to that of gold in Figure 23. Therefore, we conclude that silver can be a candidate for alternative metal other than gold for the SP structure on QDIP.

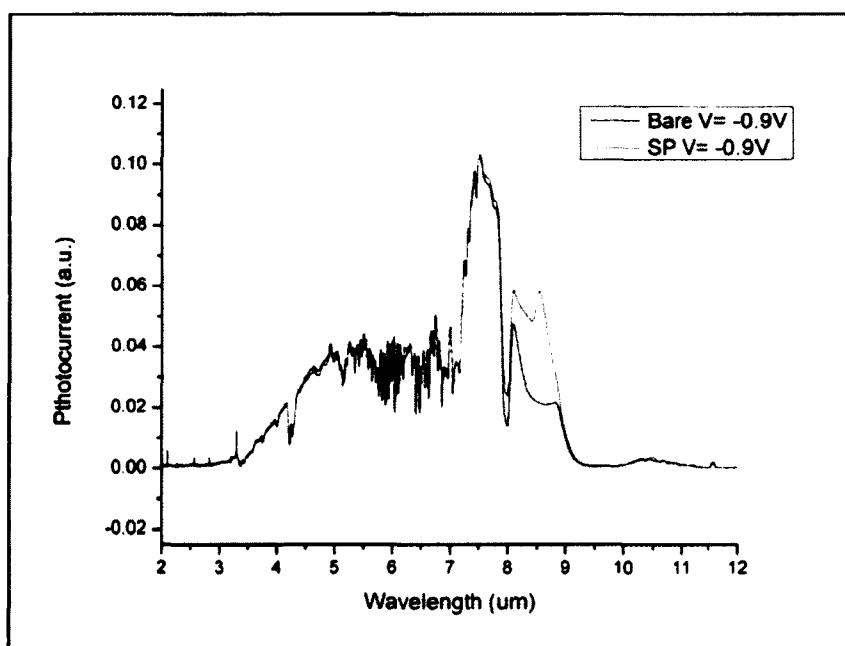


Figure 36 Spectrum Response of UML302SP (Ag)

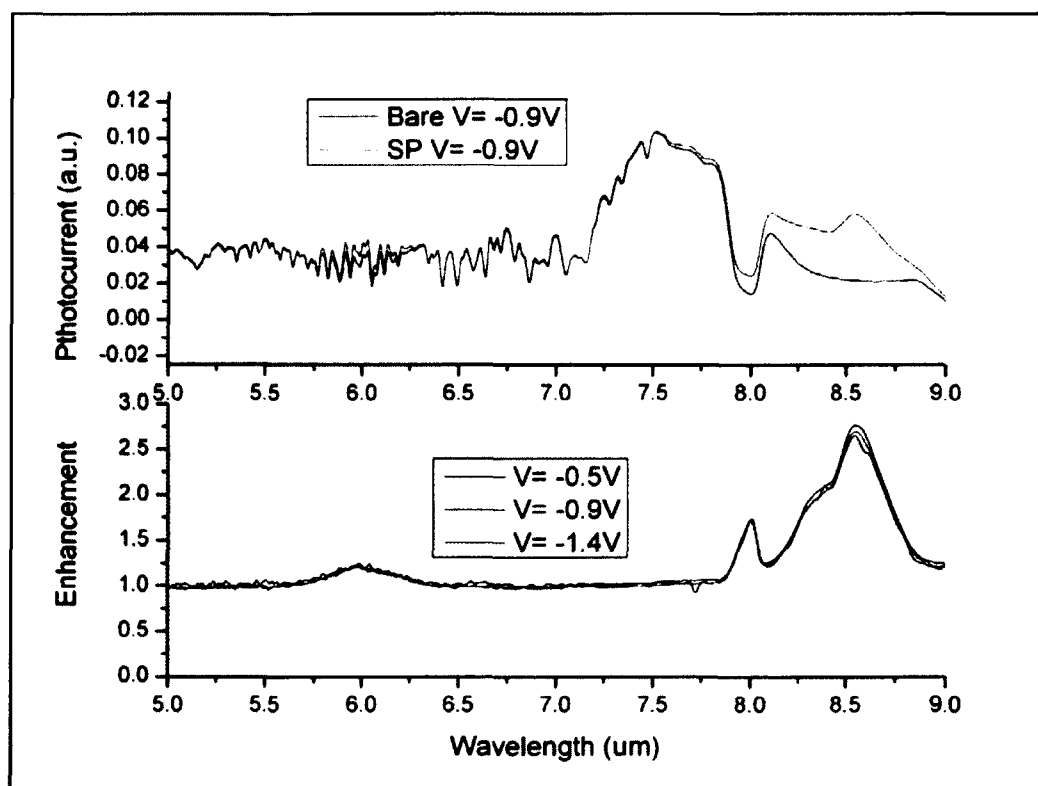


Figure 37 Spectrum Response and Enhancement Ratio of UML302SP (Ag)

4. Conclusion

In this chapter, the transmission profiles of surface plasmon structures have been reported. The relation between the peak and dip of the transmission profile and surface plasmon geometry has been studied. A long wave infrared quantum dot photodetector with the top metallic two dimension holes array structure has been fabricated. The photocurrent enhancement wavelength offset from the plasmonics resonant peak has been observed and attributed to the Fano-type interference in the metallic two dimension holes array structure. The asymmetric line shape of the plasmonics resonance has been analyzed and agrees well with the two-peak Fano-type interference model. Fano-type interference induced a red-shift of plasmonics resonance and Fano dips are observed. A 200% detectivity enhancement is obtained at the Fano dip of the first order plasmonics mode. The further investigation contains 5 projects which are lattice alignment, polarization selection, hole size variation, metal thickness variation, and metal selection. The characteristic of surface plasmon structure of each project has been addressed.

IV. POLARIZATION SELECTION OF SURFACE PLASMON ENHANCED QDIP

1. Introduction

This chapter is the following investigation from chapter III section 3.2 polarization selection. From the initial experimental result, the surface plasmon structure is applied on the top surface of QDIP. Then it will be tested the performance compared with the regular QDIP.

It has been known that periodic sub-wavelength apertures of the metallic thin film (SP structure) exhibit unique optical properties. The surface plasmon effect is important for optoelectronics devices [45], in the IR range such as laser diode and IR sensor [28, 33]. Yet, the numbers of reports of surface plasmon structure on the infrared detector are still limited. Recently, the surface plasmon polaritons have been applied to quantum well infrared photodetector (QWIP) and quantum dot infrared photodetector (QDIP) to enhance the performance [41, 46-51]. The photocurrent enhancement originates from intense electric field generated by surface plasmon polaritons at the interface of metal thin film and detector substrate. Despite the photocurrent enhancement reports, only few of polarization effect were mentioned [20]. Due to the nature of self-assembled QD

grown by the Stranski-Krastanov method, the polarization selectivity on QDIPs is still problematic to achieve with the QD growth.

This chapter is designed to study the polarization selection effect of surface plasmon structure on QDIPs. We investigated the polarization effect of the periodic metal-hole-array on QDIPs. Not only is the photocurrent enhanced, but the polarization selection on each wavelength has been realized. The relationship between the polarization and geometry of the plasmonics structure is reported. In particular, by a design of the plasmonics structure, 2 transmission peaks are reported with different polarization, x-axis and y-axis.

2. Surface Plasmon Structure Design

For surface plasmon polaritons on a metallic thin film, the wavelengths of the excited SP modes at normal incidence can be expressed as equation 10 [9]

$$\lambda_{ij} = \frac{a_0}{\sqrt{i^2 + j^2}} \sqrt{\frac{\epsilon_m \epsilon_d}{\epsilon_m + \epsilon_d}} \quad \text{Equation 10}$$

where a_0 is the period of periodic hole array on metal thin film, i and j are integers, ϵ_m is dielectric constant of metal, ϵ_d is dielectric constant of surrounding medium

One can achieve the wavelength of surface plasmon polaritons by designing the period of holes array on metal thin film. In the visible regime, several experimental and simulation results have been reported on the enhancement of transmission on holes array

metallic thin film [20, 52-54]. In infrared regime, the formula on equation 10 is still applicable with a substantial change on ϵ_m .

Figure 38 is repeated from chapter III. Our 2-dimension sub-wavelength holes array (2DSHA) is fabricated by standard lithography on GaAs wafer with gold thickness of 25nm. Various periods were investigated in chapter III. The results show the transmission profile of 2DSHA from the period of 2.2um up to 3.0um. On the label in the figure, the front number indicates period and the following number indicates circular hole size diameter. The physical geometry of 2DSHA is similar as Figure 42, except the 2DSHA is on GaAs wafer. On Figure 38, all samples have 50% filling factor. Each transmission profile displays 2 obvious peaks corresponding to surface plasmon modes in equation 10. As an example, ϵ_d is equal to 12.9 for GaAs. ϵ_m is approximately equal to $-5050 + 1090i$ for gold at wavelength of 10um [55]. For the calculated surface plasmon mode with the 3.0 um period, $\lambda_{01} = \lambda_{10} = 10.8\text{um}$, $\lambda_{11} = 7.6\text{um}$. On Figure 38, 3.0-1.5um sample shows the peak at 10.3um and 7.4um respectively to the first surface plasmon mode and second surface plasmon mode.

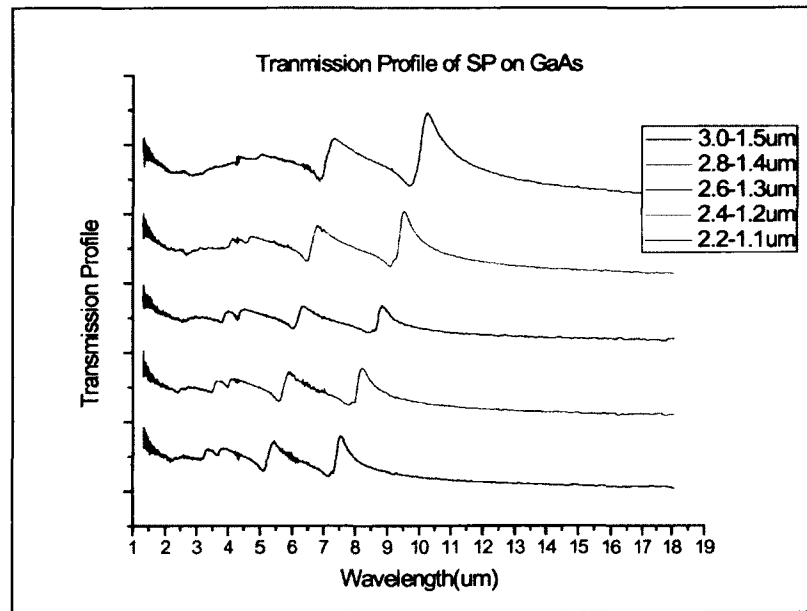


Figure 38 Transmission Profile of Surface Plasmon Structure on GaAs

Next, the linearity relationship between peak position and dip position vs. wavelength from chapter III is shown again in Figure 39. The dotted lines are experiment data and the solid lines are formulated trend lines with a high correlation coefficient more than 0.997 up to the third peak and dip. Based on our period design of Figure 39, we choose two periods of surface plasmon structure, 2.6um period and 3.0um period, to match with our QDIP operating wavelength, which is around 7-10um.

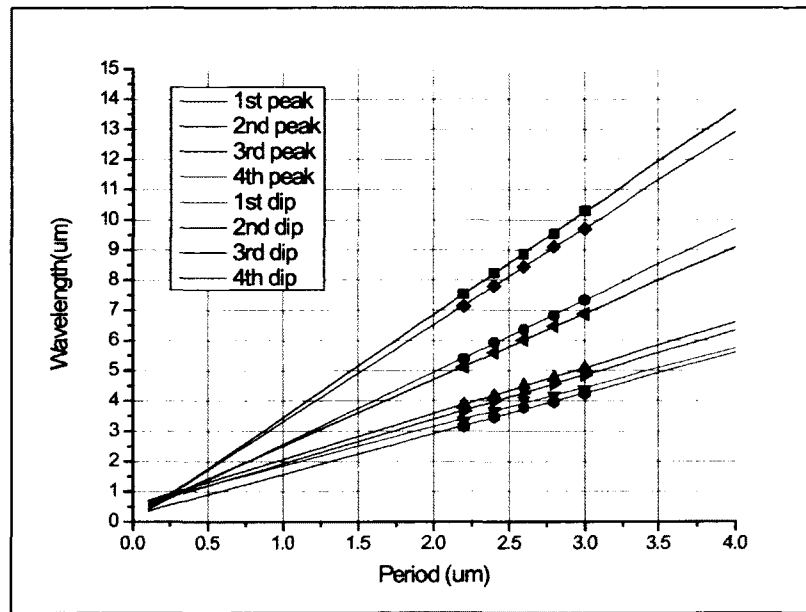


Figure 39 SP Period Design

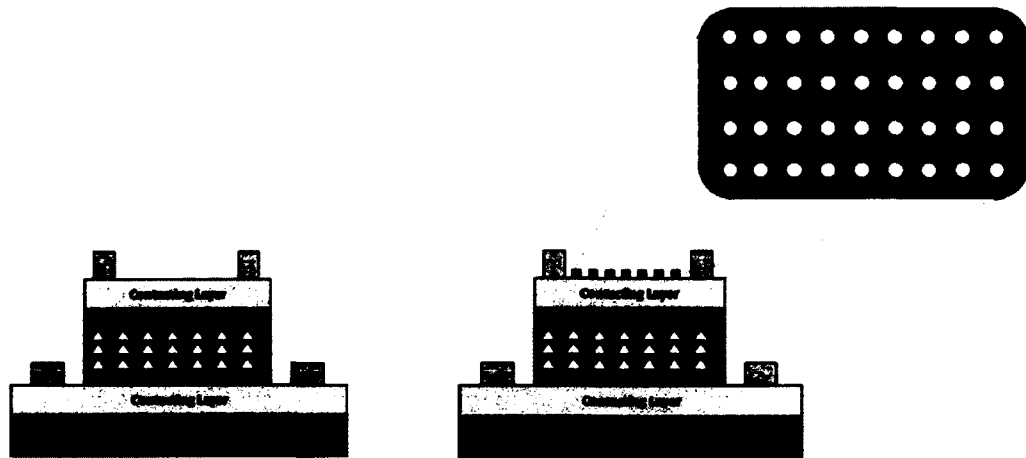


Figure 40 QDIP Diagram: Left Side for Ref-QDIP, Right Side for SP-QDIP

For comparison, we fabricated and compared regular QDIP structure and another QDIP with plasmonics structure as show in Figure 40. In Figure 40, the left figure is the diagram for reference QDIP and the right figure is the QDIP with plasmonics structure.

Both detector will be fabricated and compared for the performance enhancement later in this chapter.

We then fabricated the combination structure of two surface plasmon periods, called 2.6x-3.0y-1.3um. It has period of 2.6um on x-direction and period of 3.0um on y-direction. The hole size is 1.3um in both direction. Figure 41 shows transmission profile of 2.6x-3.0y-1.3um sample. The transmission profile exhibits an identical first surface plasmon mode of both 3.0-1.5um and 2.6-1.3um transmission at wavelength of 8.8um (λ_{10}) and 10.2um (λ_{01}). The second mode, however, doesn't replicate any peak of either previous sample but locates in between both peaks at 6.7um (λ_{11}). This can be explained from the Figure 42 that the first mode is corresponded with orthogonal direction (x-direction and y-direction) and the second mode is corresponded with a diagonal direction.

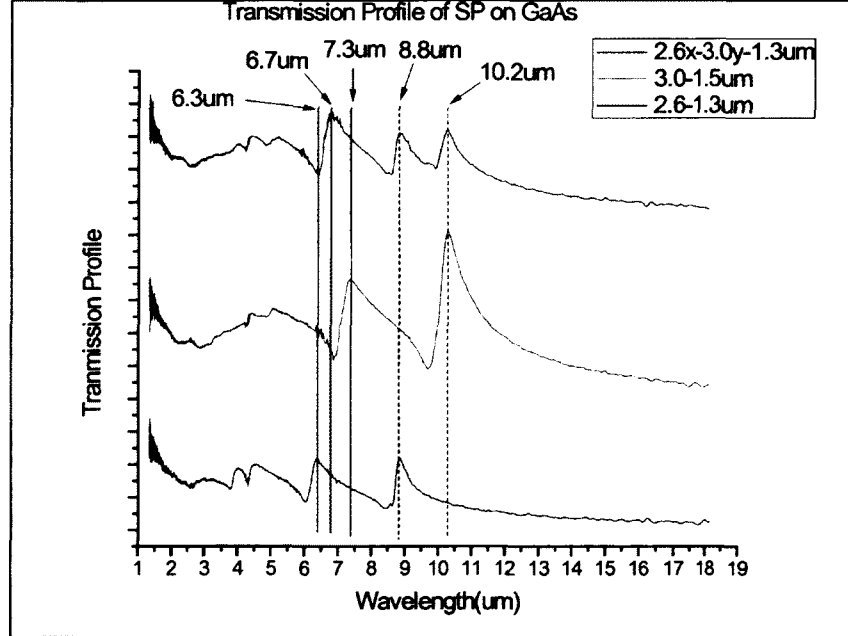


Figure 41 2.6x-3.0y-1.3um Sample Transmission Profile

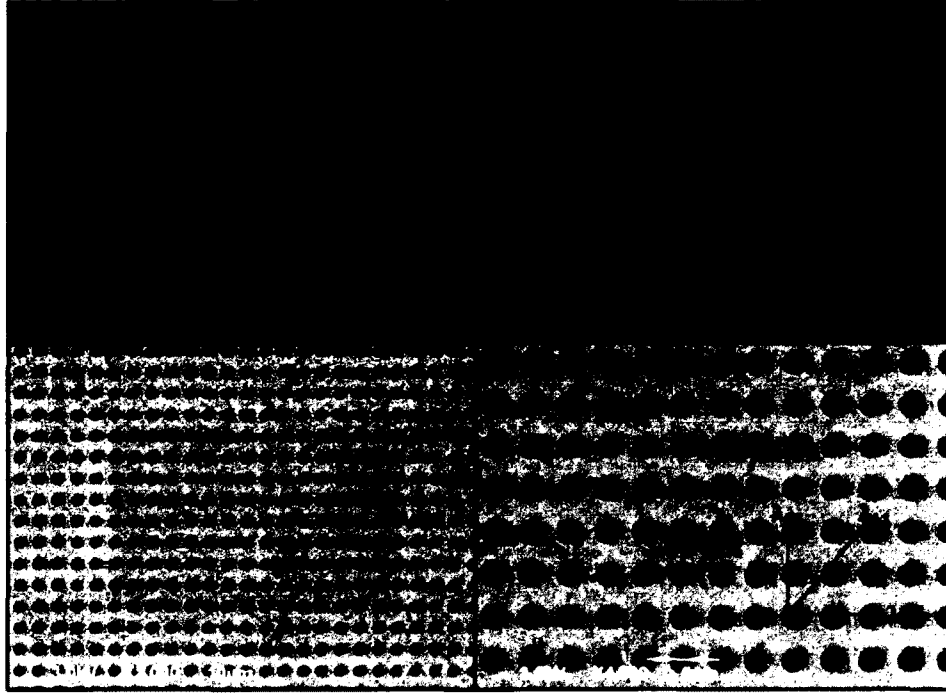


Figure 42 2DSHA on QDIP

For surface plasmon structure on two different periods, the grating momentums are different between x-direction and y-direction. For our 2.6x-3.0y-1.3 μm sample, $|G_x| = \frac{2\pi}{a_0}$, $|G_y| = \frac{2\pi}{b_0}$ where $a_0 = 2.6\mu\text{m}$ and $b_0 = 3.0\mu\text{m}$. With momentum conservation and surface plasmon dispersion on smooth thin film [37], the wavelengths of the excited surface plasmon modes at normal incidence can be expressed as equation 11

$$\lambda_{ij} = \frac{\sqrt{\frac{\epsilon_d \epsilon_m}{\epsilon_d + \epsilon_m}}}{\sqrt{\left(\frac{i}{a_0}\right)^2 + \left(\frac{j}{b_0}\right)^2}} \quad \text{Equation 11}$$

The transmission profile of 2.6x-3.0y-1.3 μm sample is plotted in Figure 43 with polarization dependent investigation. The top subfigure represents transmission of 2.6x-3.0y-1.3 μm sample with 3 polarization direction, 0 degree (x-axis), 45 degree, and 90

degree (y-axis). Note that due to the wire grid polarizer ($T_{Polarizer} = 0.4-0.5$), all of 3 transmission signals are about half of the transmission without polarizer. The bottom subfigure demonstrates clearly that the peak of the first surface plasmon mode depend strongly on the polarization direction. For 0 degree polarization, the first surface plasmon mode exists only at wavelength of 8.8 μm but 10.2 μm peak disappears. On the contrary, 90 degree polarization presents only 10.2 μm peak but absents 8.8 μm peak. 45 degree polarization shows both peaks with lessen signal. This result indicates the polarization selection on 2 different wavelengths, 8.8 μm and 10.2 μm .

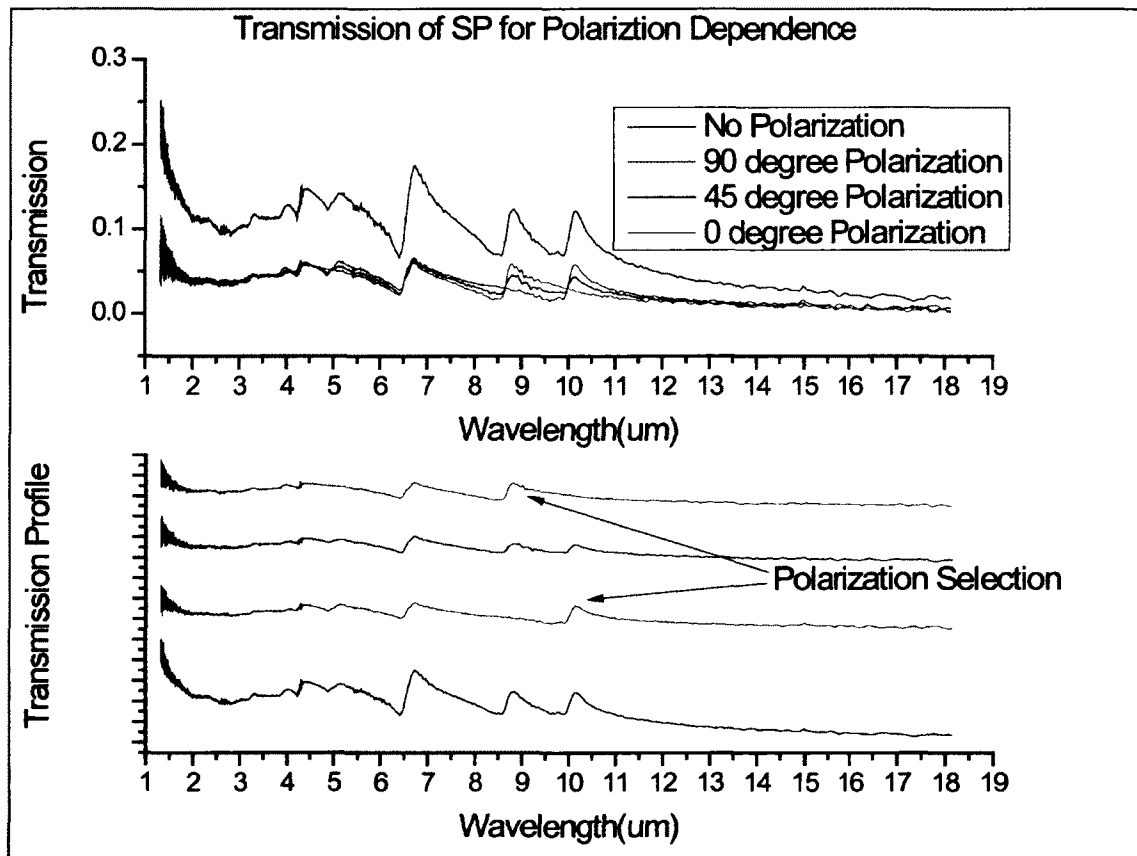


Figure 43 Transmission of 2.6x-3.0y-1.3μm Sample for Polarization Selection

3. Device Fabrication (QDIP#2461)

The QDIP is grown by molecular beam epitaxy (MBE) using a V80H MBE system. A 0.3 μm Si-doped($n+$) GaAs contact layer ($n=1\times 10^{18} \text{ cm}^{-3}$) is first grown on a semi-insulating GaAs (100) wafer, followed by the growth of 20 nm undoped $\text{Al}_{0.20}\text{Ga}_{0.80}\text{As}$ bottom current-blocking layer and a 60 nm undoped GaAs buffer layer. The growth temperature for the GaAs contact and buffer layers is 620 °C. The active absorption region consists of ten periods of QD heterostructures sandwiched between the bottom and top $\text{Al}_{0.20}\text{Ga}_{0.80}\text{As}$ current-blocking layers. Each period of the QD heterostructures consists of 1 nm $\text{In}_{0.15}\text{Ga}_{0.85}\text{As}$ followed by 2.4 monolayer (ML) of InAs, 30 ML of $\text{In}_{0.20}\text{Ga}_{0.80}\text{As}$ cap layer, and 50 nm GaAs spacer layer. The growth rates of the InAs QDs, $\text{In}_{0.20}\text{Ga}_{0.80}\text{As}$ cap layers, and GaAs spacers were 0.16, 0.8, and 0.9 ML/ s, respectively. The doping level of the QD region was estimated to be $3.5\times 10^{17} \text{ cm}^{-3}$. The QD layers and the $\text{In}_{0.20}\text{Ga}_{0.80}\text{As}$ cap layers were grown at 470 °C. The top contact layer is highly Si-doped ($n=1\times 10^{18} \text{ cm}^{-3}$) GaAs with a thickness of 0.1 μm . After the growth, the wafer was processed into 250 μm diameter circular mesas using standard photolithography and wet etching procedures. The top and bottom electrodes were formed simultaneously on top of and surrounding the mesas by standard e-beam metal evaporation deposition, lift-off, and thermal annealing processes. The QDIP was then wire-bonded and mounted on a cold finger inside a temperature-controllable infrared (IR) dewar with a ZnSe IR window. The photocurrent spectrum of the QDIP was measured using a Bruker Optics Tensor27 FTIR spectrometer.

2DSHA on QDIP

Afterward, we fabricated 25nm thick of 2.6x-3.0y-1.3um 2DSHA on top surface of our QDIP with standard lithography. Figure 42 shows 2.6 x-3.0y-1.3um patterns on QDIP mesa. Figure 44 shows the photocurrent spectrum of our QDIP with and without 2.6x-3.0y-1.3um pattern compared with the transmission of 2.6x-3.0y-1.3um sample. The enhancement of photocurrent spectrum corresponds to the dip of surface plasmon mode at 9.8um, 8.6um, and 6.4um. The explanation can be found elsewhere [47]. The dark current is tested both before and after the plasmonics structure was fabricated with 2.6x-3.0y-1.3um pattern on QDIP and the dark current shows essentially equivalent levels. Hence, the enhancement originates from photocurrent contributes to surface plasmon polaritons wave on the interface between 2DSHA and GaAs. We have also tested the transmission of surface plasmon structure on GaAs with different temperature ranging from T=78K to T=300K. The transmission profiles show an identical result, which peaks and dips occurred at the same wavelength and the transmission intensity has relatively same intensity.

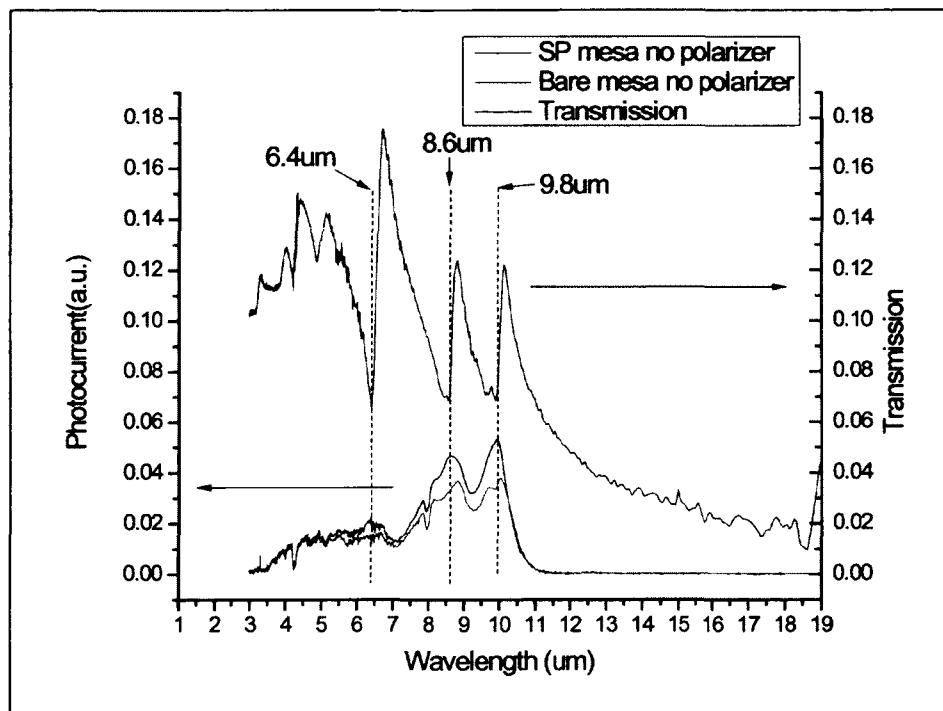


Figure 44 Photocurrent Spectrum of 2D SHA-QDIP

4. Result and Discussion

Finally, we tested the polarization dependence of 2.6x-3.0y-1.3μm pattern on QDIP. Similar to the transmission test in Figure 43, 3 polarization directions have been tested. Figure 45 Polarization Selection on 2D SHA-QDIP (No Polarizer) Figure 45 indicates the photocurrent without polarizer. Figure 46, Figure 47, and Figure 48 indicate the photocurrent with polarization selection on 0 degree polarization, 45 degree polarization and 90 degree polarization, respectively. We have tested the polarization selection on our QDIP and found that our detector responds very much alike in all polarization. We have also tested the polarization selection for our FTIR system and the

response is uniform for all polarizations. This suggests that the results on Figure 45, Figure 46, Figure 47, and Figure 48 solely contribute from the surface plasmon structure.

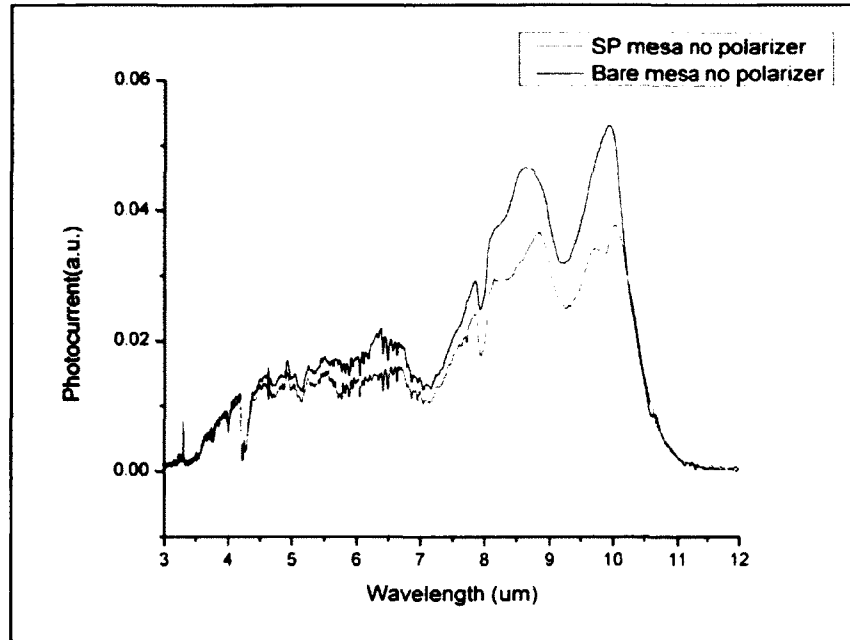


Figure 45 Polarization Selection on 2DSHA-QDIP (No Polarizer)

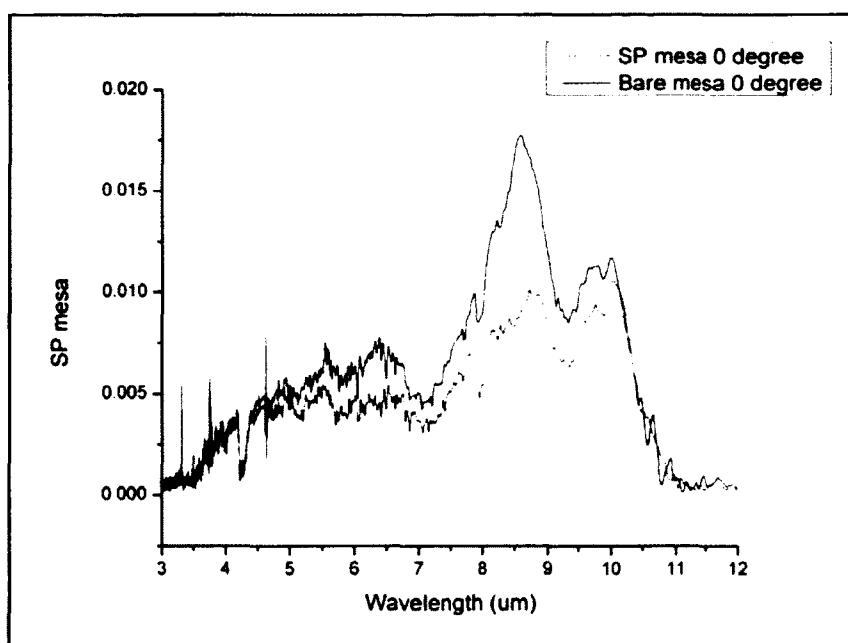


Figure 46 Polarization Selection on 2D SHA-QDIP (0 Degree)

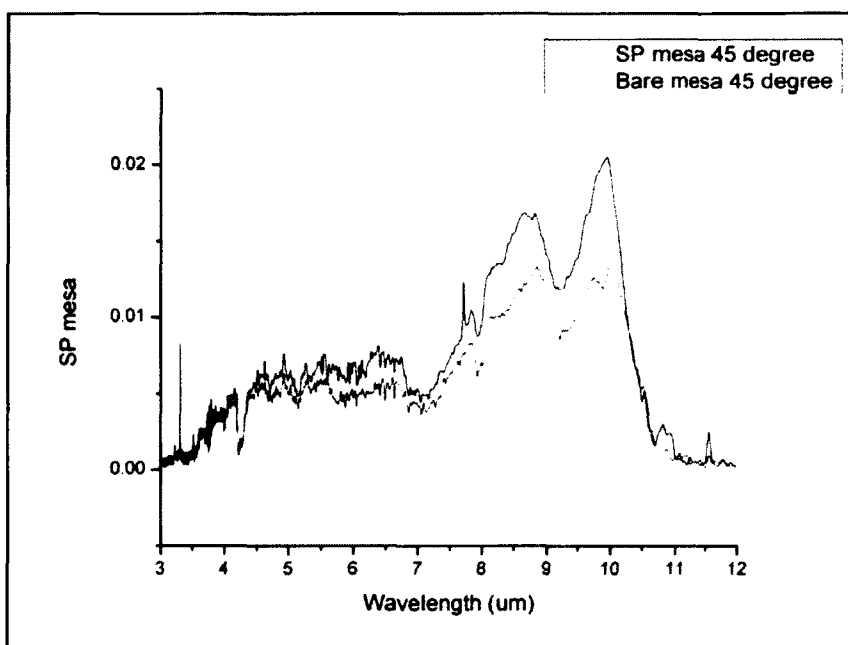


Figure 47 Polarization Selection on 2D SHA-QDIP (45 Degree)

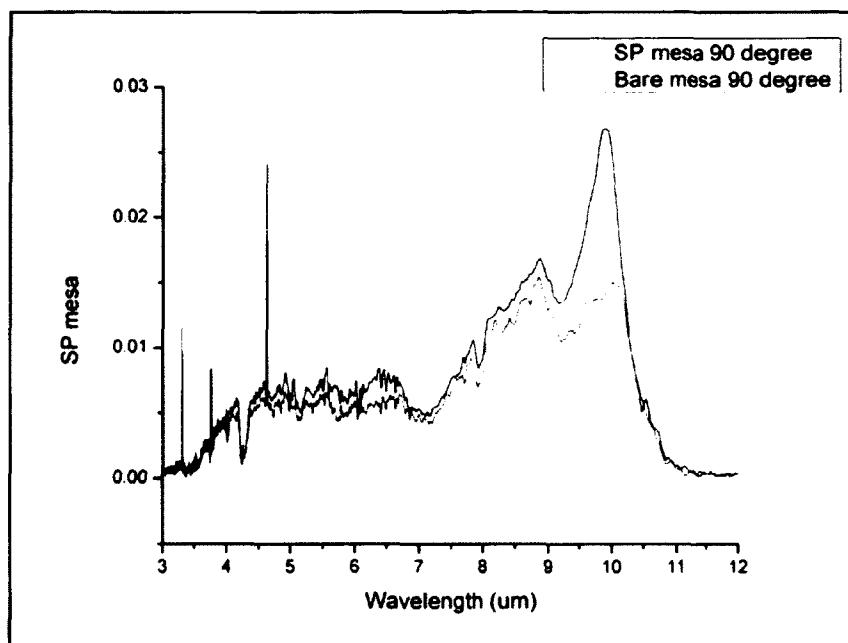


Figure 48 Polarization Selection on 2DSHA-QDIP (90 Degree)

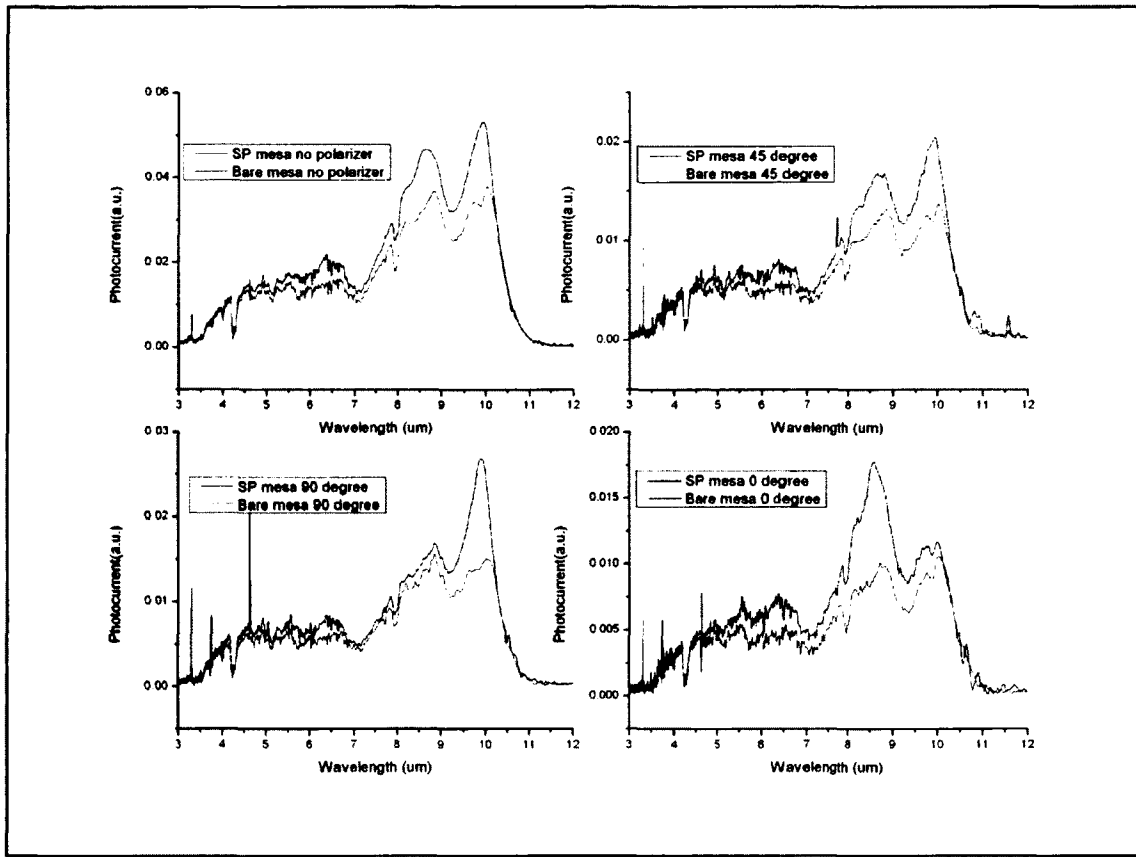


Figure 49 Polarization Selection on 2DSHA-QDIP (Summary)

The summary on Figure 49 shows significant polarization selectivity on 0 degree and 90 degree polarized. On one hand, on top subfigures, both enhancements appear on both peak at 8.6μm and 9.8μm for no polarizer and 45 degree polarized. On the other hand, the bottom subfigures show only 1 peak enhancement and solely dependent on the polarization direction. It only enhances 9.8μm peak on 90 degree polarization and 8.6μm peak on 0 degree polarization. On Figure 50, 2-times enhancement ratios have been achieved on both wavelength 8.6μm and 9.8μm. Even though 2-times extinction ratio is relatively an insignificant ratio for a commercial camera, we believe this result has overcome the possibility to manipulate the polarization selection on QDIPs due to the

uncontrollable nature of formulated quantum dot island on Stranski-Krastanov method. In addition, 2DSHA improve QDIPs performance without any adjustment on the quantum dot structure. The application of 2DSHA-QDIP will offer higher QDIP performance with easier fabrication process.

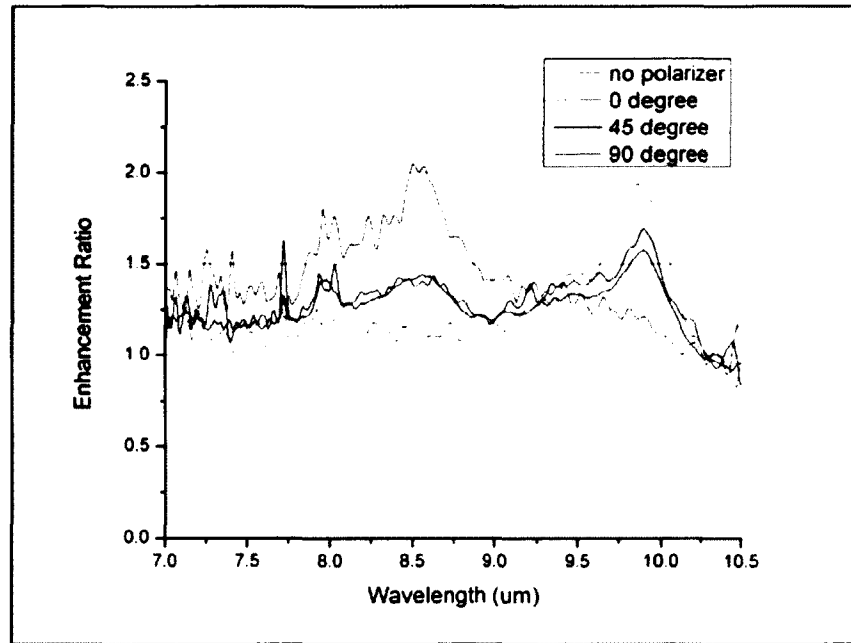


Figure 50 Enhancement Ratio on 2DSHA-QDIP

5. Conclusion

In summary, we have reported the enhancement of photocurrent on QDIPs with plasmonics structure. We have shown that two polarizations from two wavelengths can be obtained by the design of plasmonics structure. From transmission profile, the polarization dependence of the plasmonics structure has been investigated. We have formulated the period design of 2DSHA, particular for gold metallic thin film on GaAs

substrate, to match with our QDIP working wavelength. The plasmonics structure is then applied to the QDIP and has been found the photocurrent enhancement with polarization dependence. Our result offers the multi-colors and multi-polarizations on a single QDIP detector. Various applications could benefit from this method. In particular, the result offers the development of infrared sensor to detect polarization selection which leads the way to superior infrared camera.

V. METAL THICKNESS VARIATION EFFECT OF SURFACE PLASMON ENHANCED QDIP

This chapter outlines the investigation from the initial experimental results in chapter III section 3.4 Metal Thickness Variation. The surface plasmon structures, with varying thicknesses, are applied on the top surface of the QDIP and the performance of the devices was tested.

1. Introduction

From chapter III and IV, we see the importance of lattice symmetry on surface plasmon excitation along the surface dimension (X and Y dimension). The period of holes array plays a crucial role on the selective wavelength of the surface plasmon enhanced QDIP. In this chapter, we shall investigate another dimension of the holes array, Z dimension.

Surface plasmon wave exists on the interface between metal thin film and substrate, in this case gold thin film and GaAs substrate. Its properties depend on the dielectric constant of both medium and the metal film thickness. Several reports shown that the film thickness plays a role on optimizing electric field amplitude [12, 52, 53, 56-58]. Lochbiler [58] suggests that the physical dimension of gold wire grating have a

strong influence on the frequency shift (or wavelength shift) on the surface plasmon dispersion curve. Grupp et al [59] reported the role of the aperture depth on the enhanced transmission of light through sub-wavelength holes in free-standing Ag films by measuring the transmission properties of square arrays of cylindrical holes. Mahboub et al [57] also reported the optimization of bull's eye structure of transmission enhancement. In Mahboub's report, the groove depth was investigated and found to have an influence on the transmission on both experimental and theoretical. Several studies have also reported that the groove structure and the depth play a role on the laser beam shaping [31, 32, 60]. Oh et al [56] shown clearly that the height of bump grating has an effect on the efficiency of surface plasmon resonance excitation. Despite numbers of reports on metal thickness influenced by surface plasmon, the direct study of metal thickness variation effect on the detector still has not yet reported. Therefore, metal thickness variation effect of surface plasmon shall be investigated on QDIPs.

2. Transmission of Surface Plasmon Structure with Metal Thickness Variation

For surface plasmon polaritons on metallic thin film, the wavelengths of the excited surface plasmon modes at normal incidence can be expressed as equation 12

$$\lambda_{ij} = \frac{a_0}{\sqrt{i^2 + j^2}} \sqrt{\frac{\epsilon_m \epsilon_d}{\epsilon_m + \epsilon_d}} \quad \text{Equation 12}$$

where a_0 is the period of periodic hole array on metal thin film, i and j are integers, ϵ_m is dielectric constant of metal, ϵ_d is dielectric constant of surrounding medium.

For this investigation, we choose the period of surface plasmon structure at 2.6 μ m which enhance our QDIP performance at 8.6 μ m wavelength.

Table 4, Table 5, and Figure 51 are repetition from chapter III session 4) Metal Thickness Variation. Wood's anomaly [44] suggested that the thickness of the metal could play the role on the dark spot of spectrum from metal grating due to the light traveling along surface of the metal. It is stated that the metal thickness could also effect on the transmission profile of surface plasmon structure as well. The bandwidth of the transmission profile may relate to the metal thickness, we tested full-width-half-maximum for each transmission profile (Table 4). We also tested full-width-75%-maximum to measure the bandwidth of peak1 and peak2 which are the first and the second plasmonics resonance mode (mode01 and mode10)

FWHM(μ m)	peak3	peak2	peak1
Au 25nm	1.591		
Au 50nm	1.172	0.783	
Au 100nm	0.76	0.515	0.538

Table 4 FWHM (μ m) of SP Transmission Varied Metal Thickness.

FW75%M(um)	peak3	peak2	peak1
Au 25nm	0.603	0.523	0.444
Au 50nm	0.423	0.302	0.314
Au 100nm	0.286	0.252	0.254

Table 5 FW75%M (um) of SP Transmission Varied Metal Thickness.

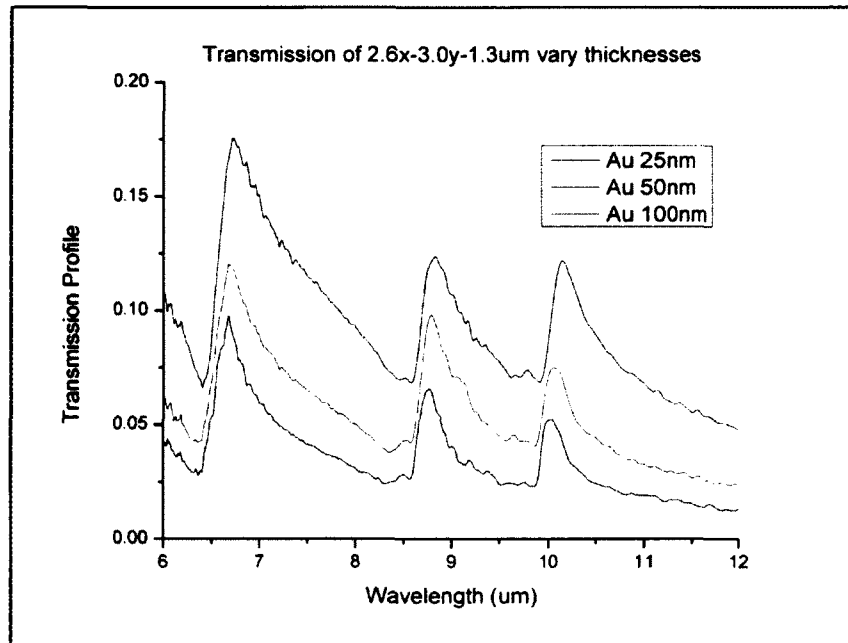


Figure 51 Transmission of Plasmonics Structure Varied Metal Thickness

Transmission profile of plasmonics structure was tested at different temperatures from 78K to 300K to verify the temperature role on transmission profile. Figure 52 confirms that the transmission profile of our plasmonics structure is not a function of temperature.

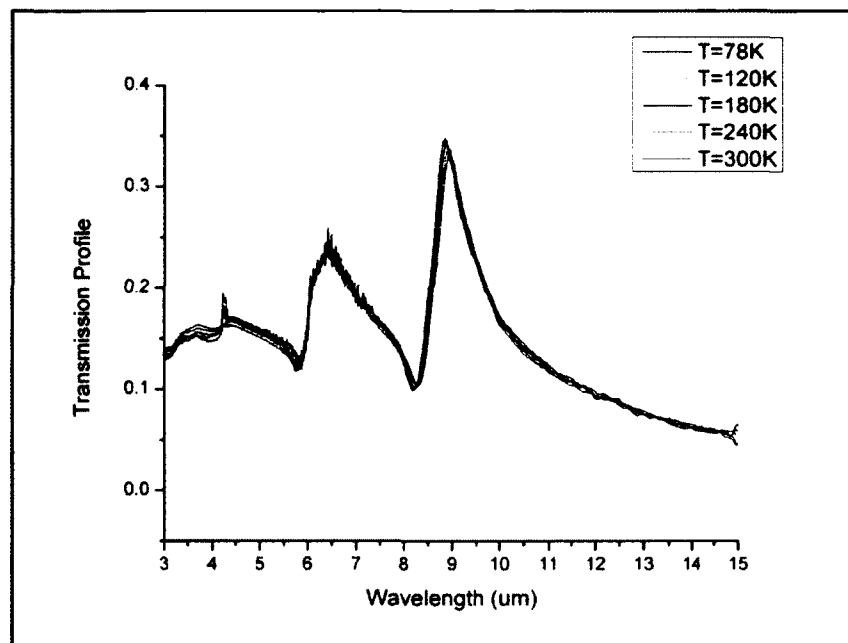


Figure 52 Transmission of Plasmonics Structure Varied Temperature

To obtain the transmission profile of plasmonics structure for thick metal (more than 100nm), LOR photoresist was used as a sacrificial layer underneath Shipley photoresist. The structure period was chosen at 5um for the convenience of fabrication. Nine thicknesses of plasmonics structures were fabricated on GaAs substrates and the transmission profile measured. The results are shown in Figure 53 and Figure 54. The minimum value and maximum value of the transmission profile were plotted on Figure 55. The minimum value and maximum value took place at 100nm thickness. This result suggests that the transmission profile of plasmonics structure can be optimized which leads to the consequence of optimized metal thickness on the detector. For this project, the QDIP sample UML273 is selected. The surface plasmon structure was chosen to be 2.6um period to match with UML273 pick up wavelength. The device fabrication is explained and the result and discussion will be followed.

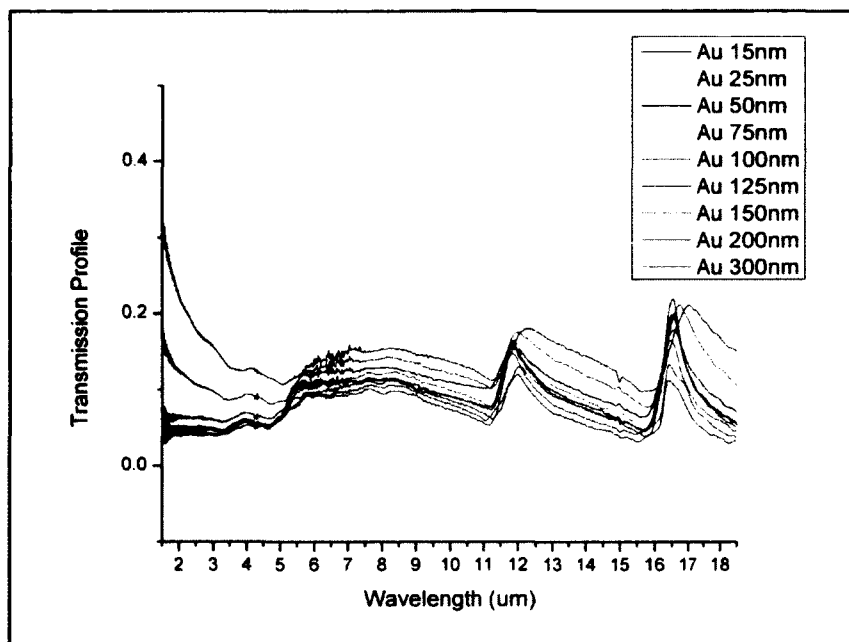


Figure 53 Transmission of Plasmonics Structure Varied Metal Thickness (15nm-300nm)

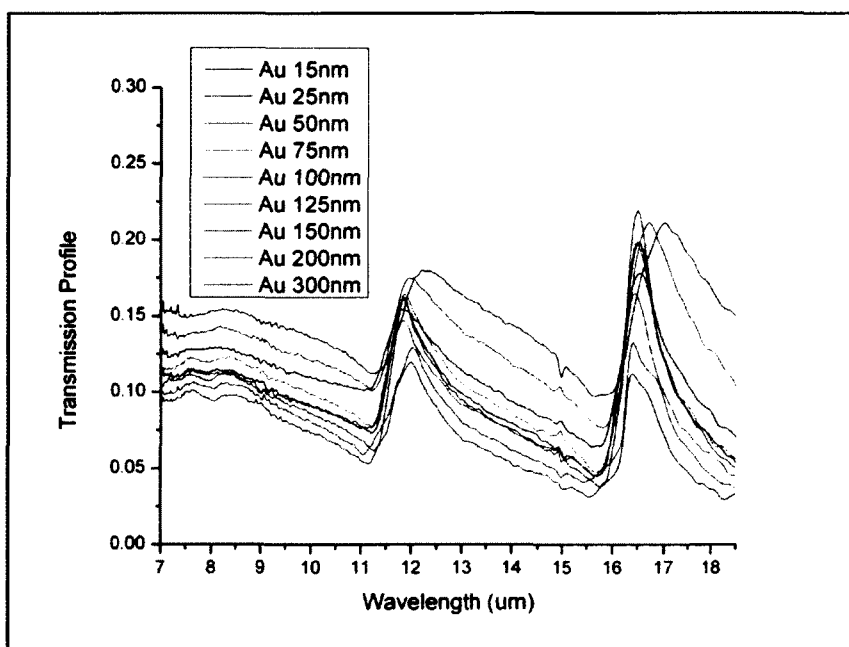


Figure 54 Transmission of Plasmonics Structure Varied Metal Thickness (15nm-300nm)

Zoom in

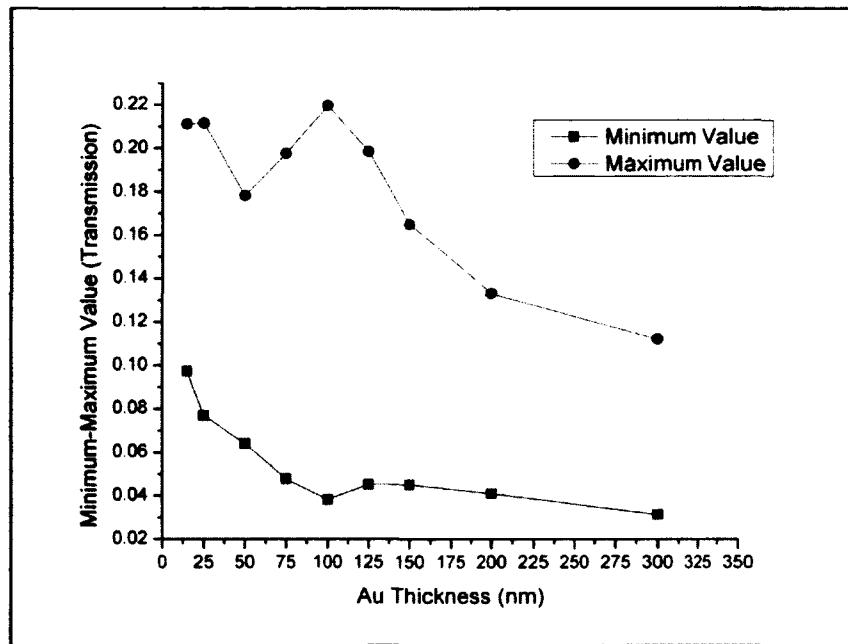


Figure 55 Maximum-Minimum Value of Transmission Profile

Calculated Momentum Vector (k_z)

Before fabricating the surface plasmon structure on QDIP sample UML273, the surface plasmon structure of 2.6 μ m period was fabricated on bare GaAs wafer again for 4 different thicknesses, 25nm, 50nm, 75nm and 100nm. The transmission profiles are presented on Figure 56. From this transmission profile, we can calculate momentum vector (k_z) by the following explanation.

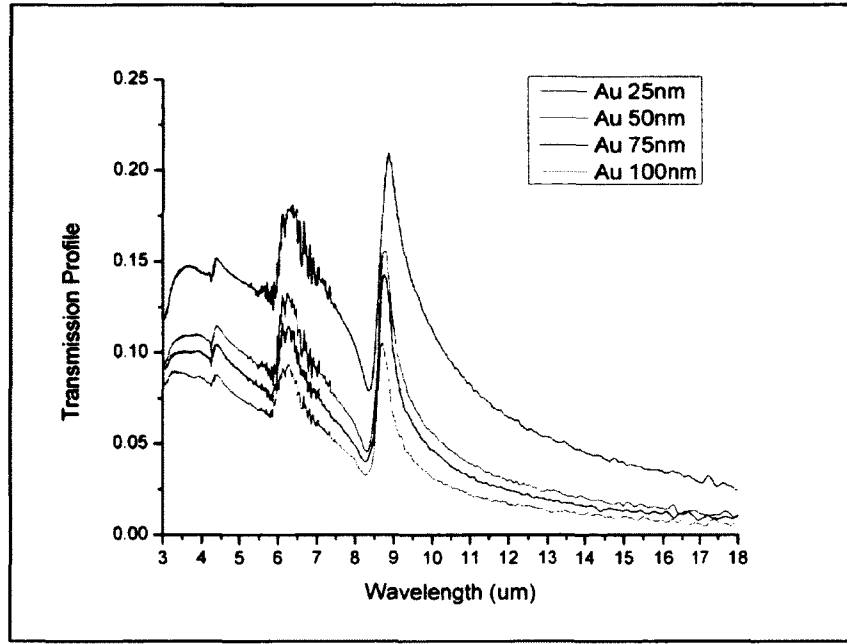


Figure 56 Transmission Profile of Surface Plasmon Structure 2.6um Period

From the transmission profile on Figure 56, assume

$$T \propto E_z^2 = A * e^{2k_z Z}$$

where as A is an arbitrary, k_z is momentum vector on z-direction, Z is the metal thickness. Then, take natural log on both side of the equation;

$$\ln(T) = (2k_z)Z + \ln(A)$$

Arrange the equation to a linear relation as $Y = aZ + b$, we obtain k_z from the slope of the linear relation. Calculated k_z is then plotted on the wavelength domain in Figure 57. Correlation Coefficient of k_z is also shown in Figure 58. The Calculated k_z in Figure 57 shows the peaks at the wavelength of 8.6um and 6.0um. The Correlation

Coefficient of k_z in Figure 58 shows consistent value around 95% along wavelength 3-18 μm .

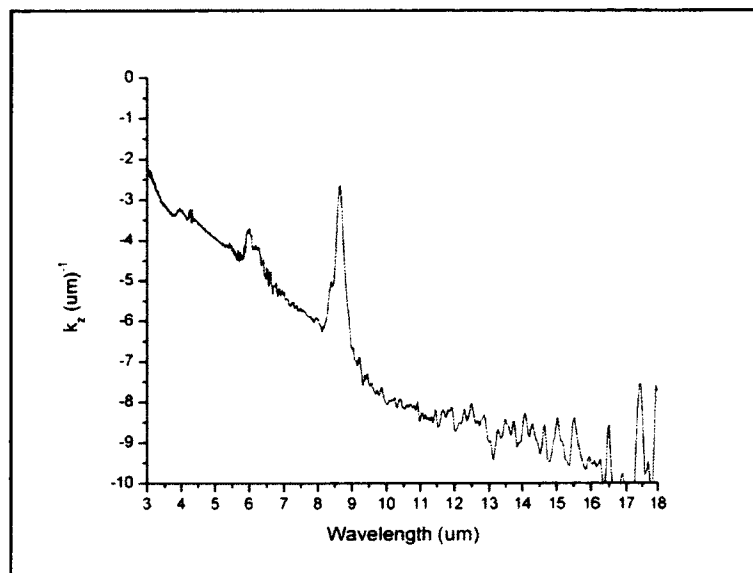


Figure 57 Calculated Momentum Vector (k_z) on Wavelength Domain

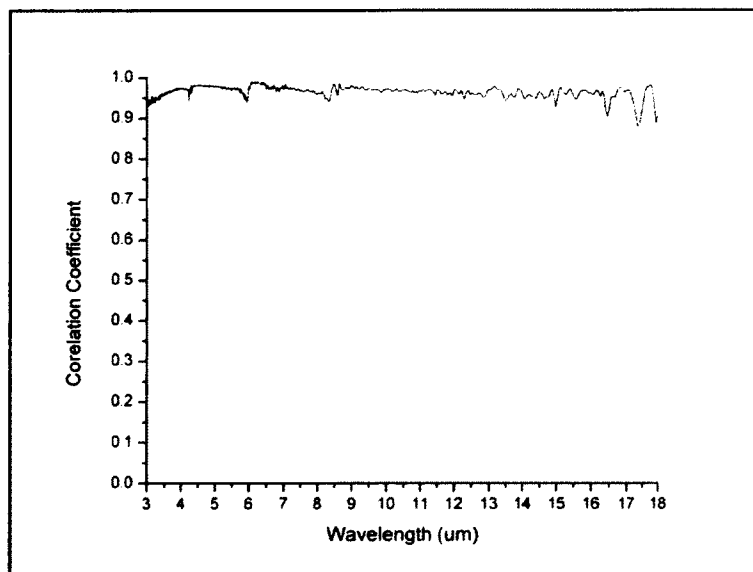


Figure 58 Correlation Coefficient of k_z

3. Device Fabrication (UML273)

The QDIP is grown by molecular beam epitaxy (MBE) using a V80H MBE system. A 0.3 μm Si-doped($n+$) GaAs contact layer ($n=1\times 10^{18} \text{ cm}^{-3}$) is first grown on a semi-insulating GaAs (100) wafer. The growth temperature for the GaAs contact and buffer layers is 620 $^{\circ}\text{C}$. The active absorption region consists of ten periods of QD heterostructures consists of 1 nm $\text{In}_{0.15}\text{Ga}_{0.85}\text{As}$ followed by 2.0 monolayer (ML) of InAs, 30 ML of $\text{In}_{0.20}\text{Ga}_{0.80}\text{As}$ cap layer, and 50 nm GaAs spacer layer. The growth rates of the InAs QDs, $\text{In}_{0.20}\text{Ga}_{0.80}\text{As}$ cap layers, and GaAs spacers were 0.16, 0.8, and 0.9 ML/ s, respectively. The doping level of the QD region was estimated to be $3.5\times 10^{17} \text{ cm}^{-3}$. The QD layers and the $\text{In}_{0.20}\text{Ga}_{0.80}\text{As}$ cap layers were grown at 470 $^{\circ}\text{C}$. The top contact layer is highly Si-doped ($n=1\times 10^{18} \text{ cm}^{-3}$) GaAs with a thickness of 0.1 μm . Figure 59 shows the structure of UML273 sample. After the growth, the wafer was processed into 250 μm diameter circular mesas using standard photolithography and wet etching procedures. The top and bottom electrodes were formed simultaneously on top and surrounding of the mesas by standard e-beam metal evaporation deposition, lift-off, and thermal annealing processes. The QDIP was then wire-bonded and mounted on a cold finger inside a temperature-controllable infrared (IR) dewar with a ZnSe IR window. The photocurrent spectrum of the QDIP was measured using a Bruker Optics Tensor27 FTIR spectrometer.

UML0273 Structure

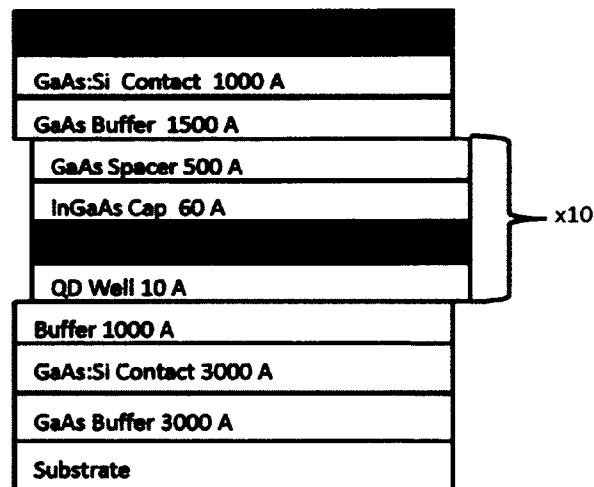


Figure 59 UML273 MBE Growth Structure

2DSHA on QDIP

Afterward, we fabricated surface plasmon structure of 2.6-1.3 μ m on top surface of our QDIP with standard lithography. We chose 6 metal thicknesses which are 25nm, 37.5nm, 50nm, 62.5nm, 75nm, and 100nm for comparison. Each of the plasmonics sample has bare detector that stands side by side used for reference purpose. Both plasmonics sample and reference sample will be tested in controlled environment and compared for the enhancement. Figure 60, Figure 61, and Figure 62 are the SEM pictures of plasmonics structure on QDIP.

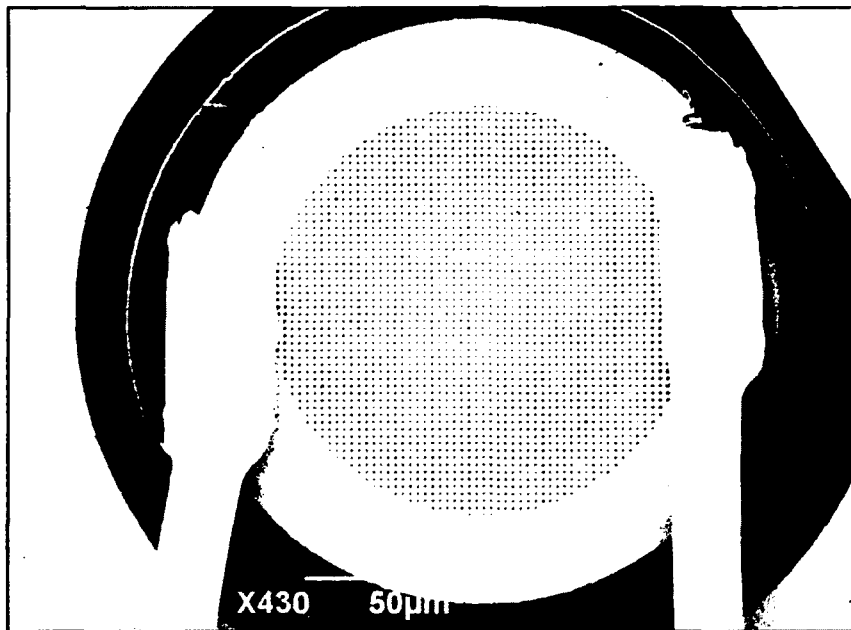


Figure 60 UML273-SP (SEM@430x magnification)

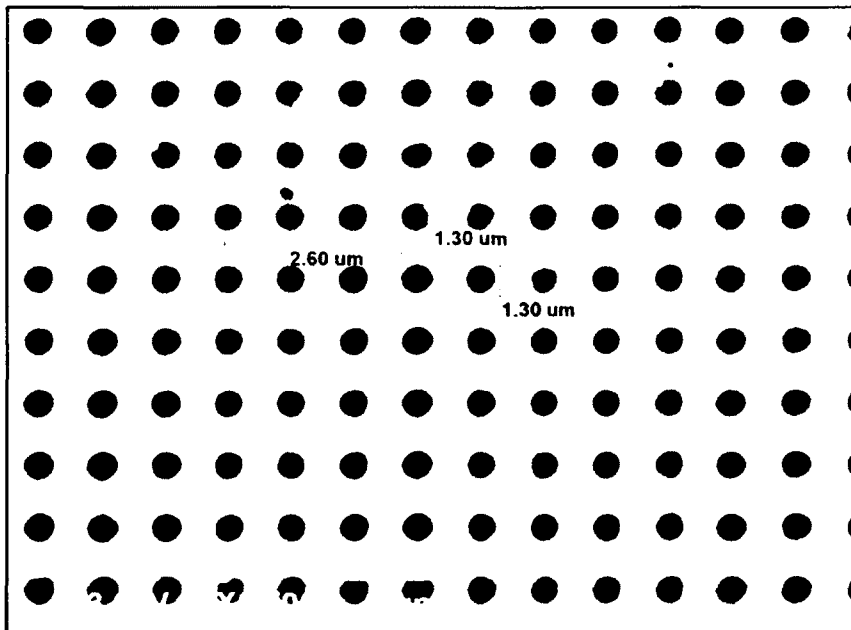


Figure 61 UML273-SP (SEM@3700x magnification)

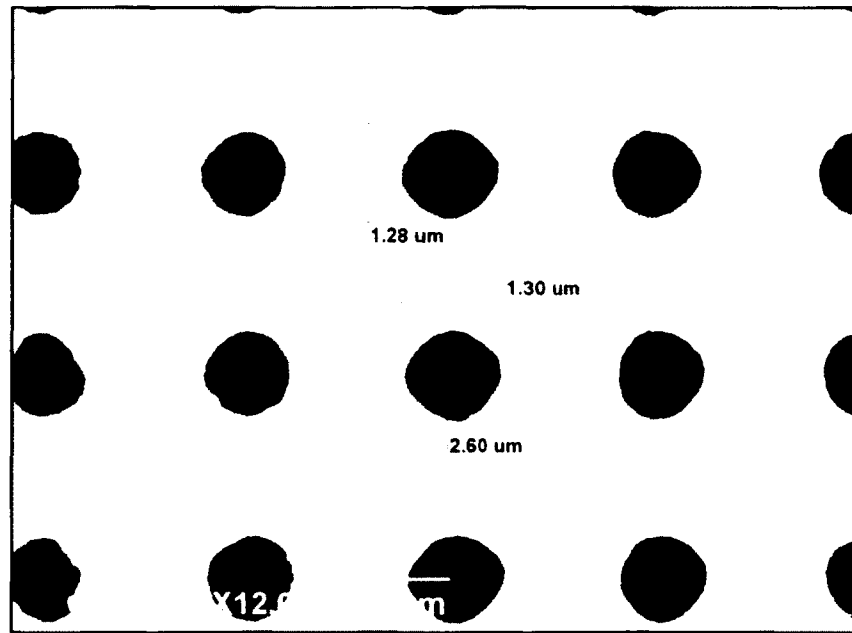


Figure 62 UML273-SP (SEM@12000x magnification)

4. Result and Discussion

The spectrum response of bare mesa and surface plasmon mesa were tested on Figure 63, Figure 64, and Figure 65 for different applied biases. Figure 63 shows the spectrum response for bias voltage $V = -0.47V$, Figure 64 for $V = -0.70V$, Figure 65 for $V = -1.2V$. For each voltage applied, the dark current is tested on the reference bare mesa and surface plasmon mesa and found to be identical. Therefore, the increasing in spectrum response is contributed to the increasing photocurrent which originates from surface plasmon wave excitation. Figure 66 and Figure 67 shows the enhancement ratio of spectrum response. Figure 66 shows 2 peaks of enhancement at $6\mu m$ and $8.6\mu m$ wavelength which is in the same position of the peaks of calculated momentum vector on

Figure 57. The maximum enhancement is around 2.5 times at 8.6um wavelength for both bias voltage $V=-0.7V$ and $V=-1.2V$.

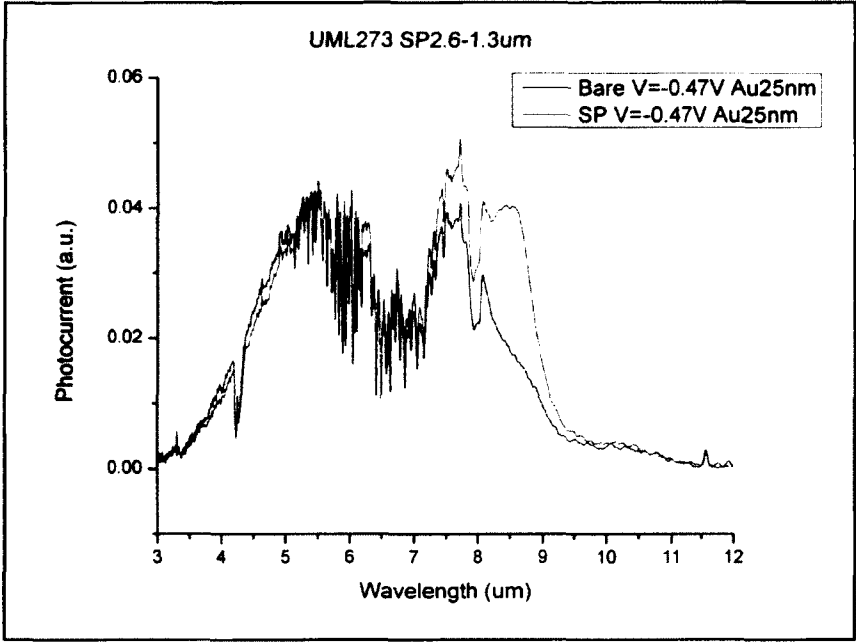


Figure 63 UML273-SP Spectrum Response $V=-0.47V$

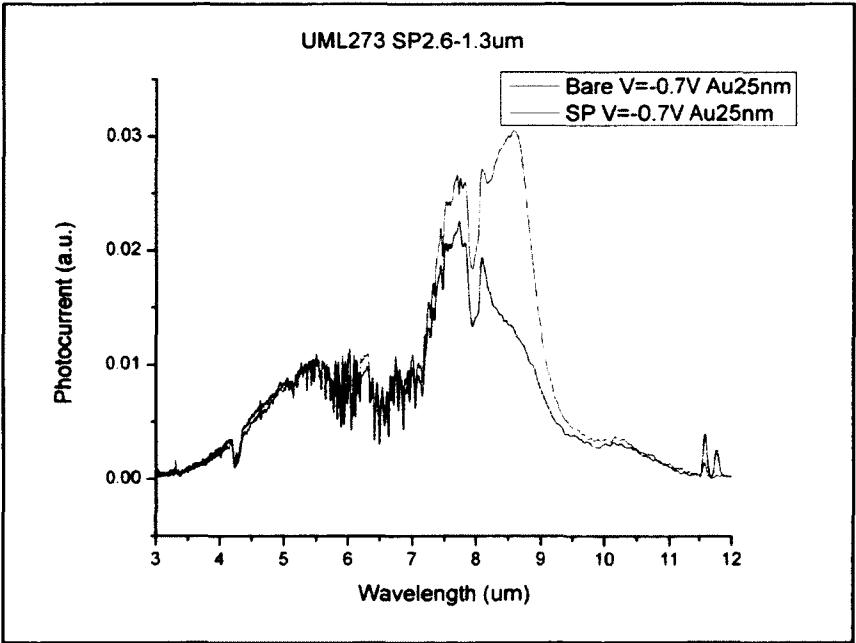


Figure 64 UML273-SP Spectrum Response $V=-0.70V$

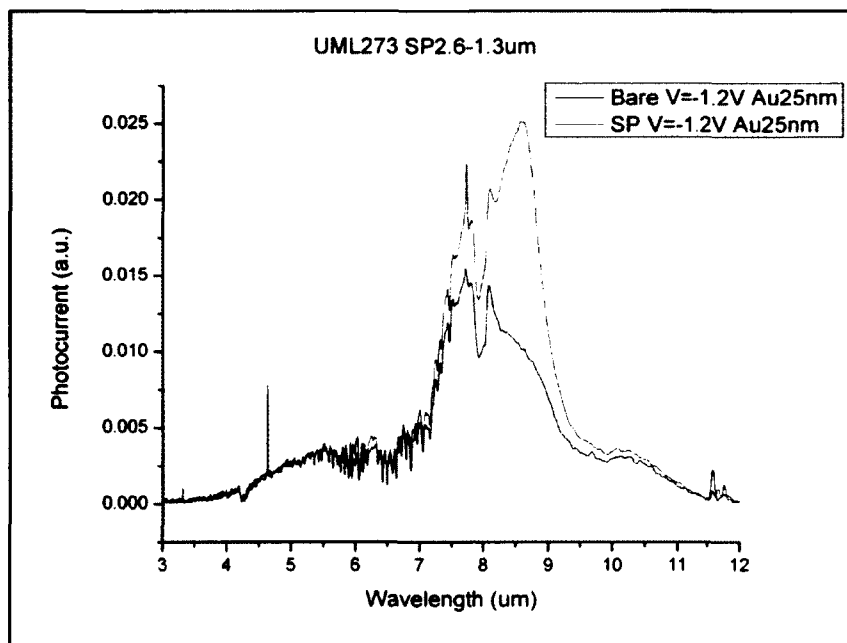


Figure 65 UML273-SP Spectrum Response V=-1.20V

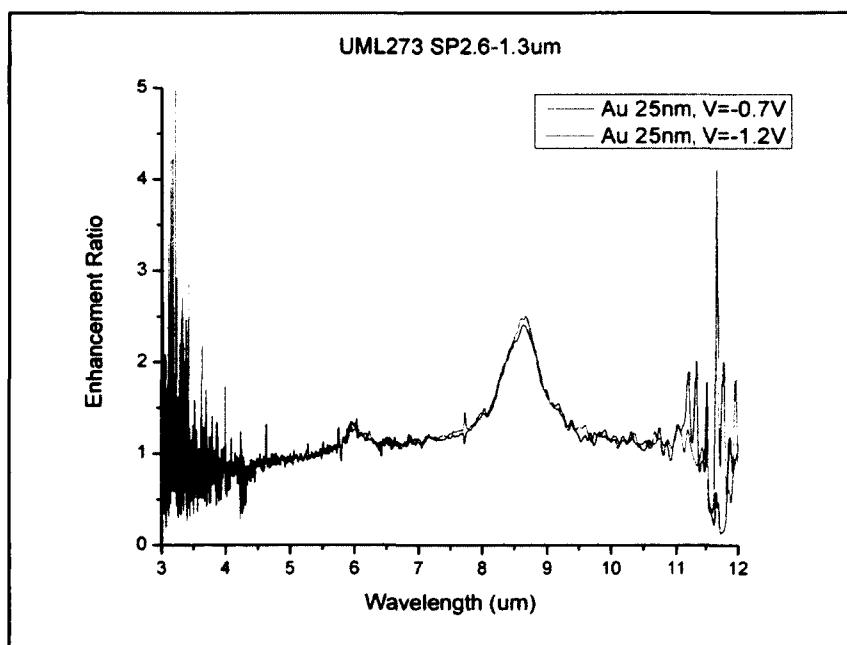


Figure 66 UML273-SP Enhancement Ratio

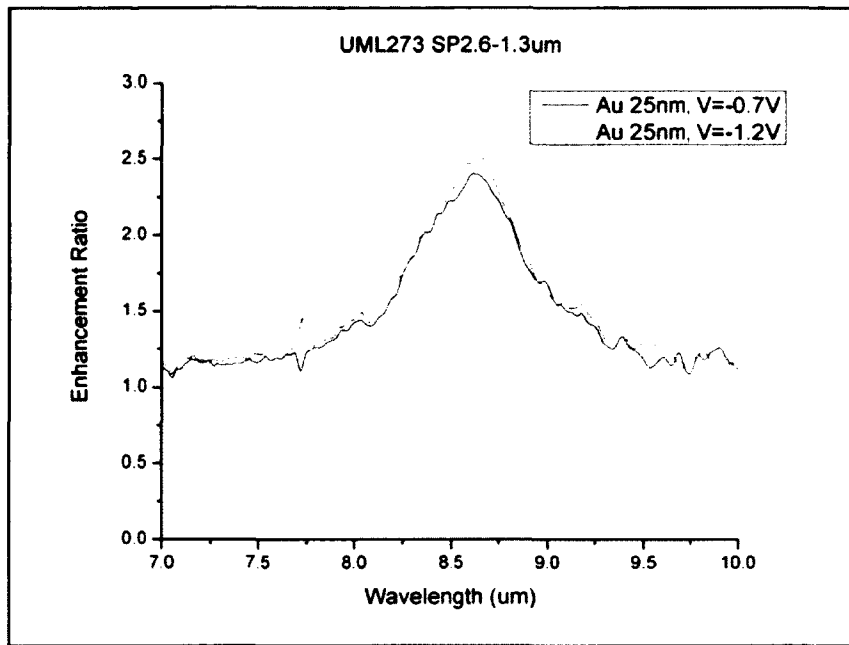


Figure 67 UML273-SP Enhancement Ratio Zoom in

For all of metal thicknesses (25nm, 37.5nm, 50nm, 62.5nm, 75nm, and 100nm), both bare mesa and plasmonics mesa were tested and compared for the enhancement ratio. The enhancement ratios are shown here on Figure 68 and Figure 69 for bias voltage $V=-0.7V$ and $V=-1.2V$. From both Figure 68 and Figure 69, it clearly suggests that the optimized metal thickness for plasmonics structure (2.6um period) on our QDIP is at 75nm. The enhancement peak of 75nm thickness is around 5.6 times compared to the bare mesa. And it can be seen that different voltage does not have significant change on the enhancement. Figure 70 are plotted again for the enhancement ratio with only bias voltage $V=-0.7V$

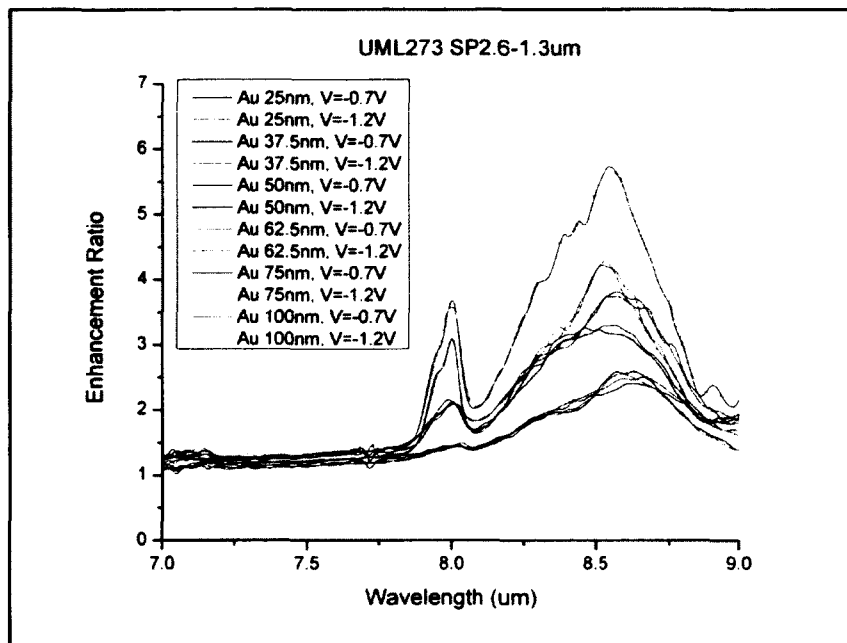


Figure 68 UML273-SP Enhancement Ratio Varied Metal Thickness

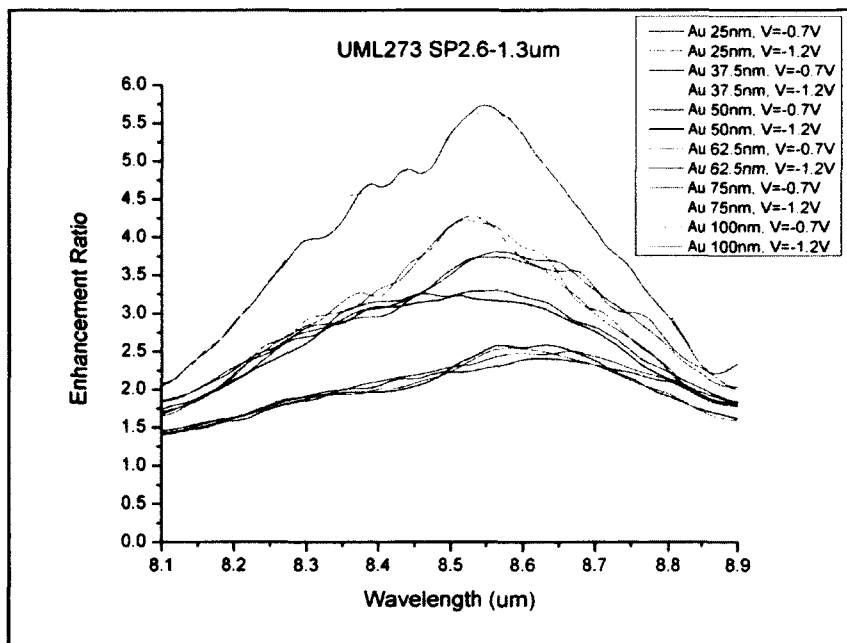


Figure 69 UML273-SP Enhancement Ratio Varied Metal Thickness Zoom in

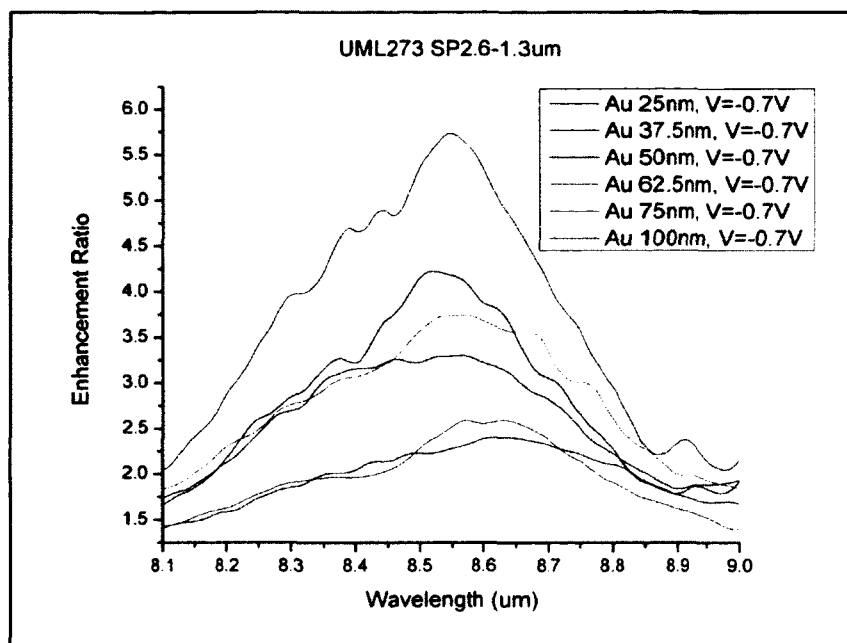


Figure 70 UML273-SP Enhancement Ratio Varied Metal Thickness $V = -0.70V$

For each metal thickness, the maximum values of enhancement ratio on QDIP were extracted from the graph and report in Table 6. The maximum enhancement is at 75nm of gold thickness with 5.67 time of enhancement for plasmonics structure 2.6um period.

Thickness(nm)	Max Enhancement
25	2.502
37.5	2.549
50	3.233
62.5	3.808
75	5.669
100	4.277

Table 6 Maximum Value of Enhancement on QDIP (UML273-SP2.6-1.3um)

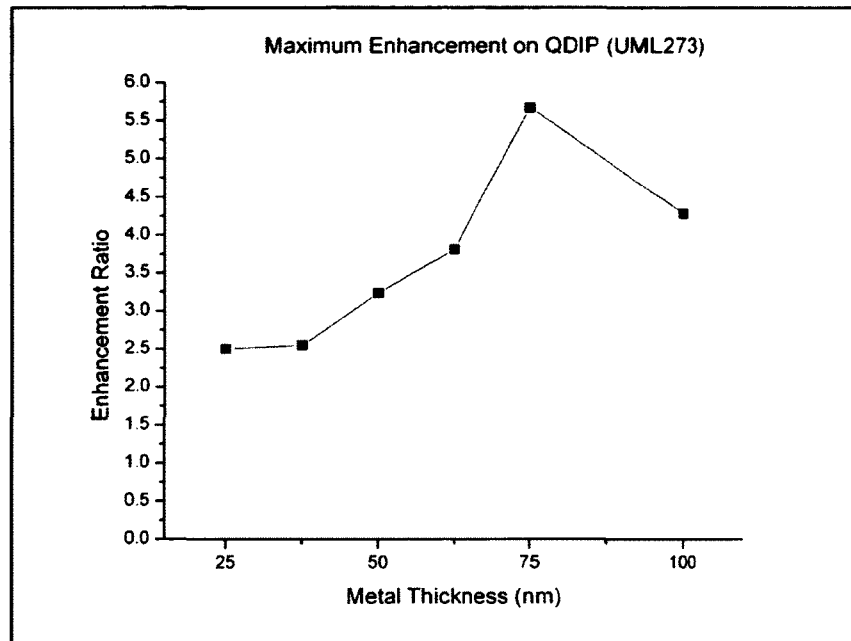


Figure 71 Maximum Value of Enhancement on QDIP (UML273-SP2.6-1.3um)

From the enhancement ratio, the full-width-half-maximum (FWHM) were measured with different bias voltage ($V = -0.7V, -1.2V, -1.8V$) and found to be relatively same value. Table 7 shown the FWHM of the enhancement on each metal thickness.

Thickness(nm)	FWHM(nm) of Enhancement
25	685
37.5	627.5
50	601
62.5	564
75	538
100	492

Table 7 FWHM of Enhancement on QDIP (UML273-SP2.6-1.3um)

After the metal thickness variation effect of surface plasmon on QDIP was successfully demonstrated, we repeated the experiment again on the QDIP sample

UML291 with surface plasmon structure of period 2.4 μm which has expected enhancement around 8 μm wavelength. This time, the surface plasmon structure has period of 2.4 μm and vary the hole size diameter from 1.2 μm to 1.5 μm . The gold metal thickness are also vary as same as previous session which are from 25nm to 100nm. The results are shown on Figure 72, Figure 73, Figure 74, and Figure 75. From the results, it shows clearly that the maximum enhancement is remaining consistent at the thickness of 75nm. Note here that on Figure 72, there is no data for 75nm thickness because of the limited resource on the fabrication. However Figure 72, Figure 73, and Figure 74 show the similar result. The maximum enhancement present at 6-8 times for the hole diameter 1.2 μm -1.4 μm . For the hole diameter 1.5 μm , the maximum enhancement is at 3 times. From these results, we can conclude that the optimization of metal thickness variation for this project should be at 75nm for our QDIP.

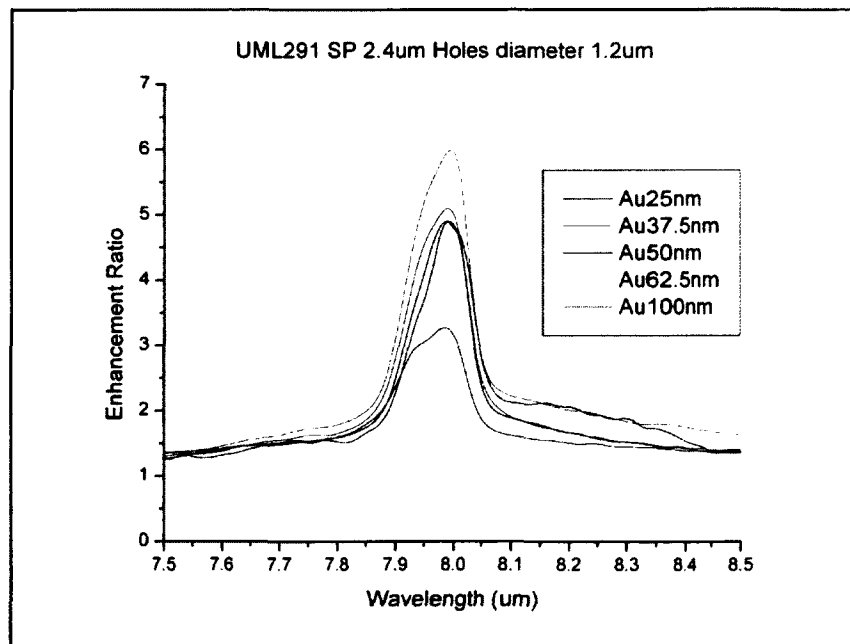
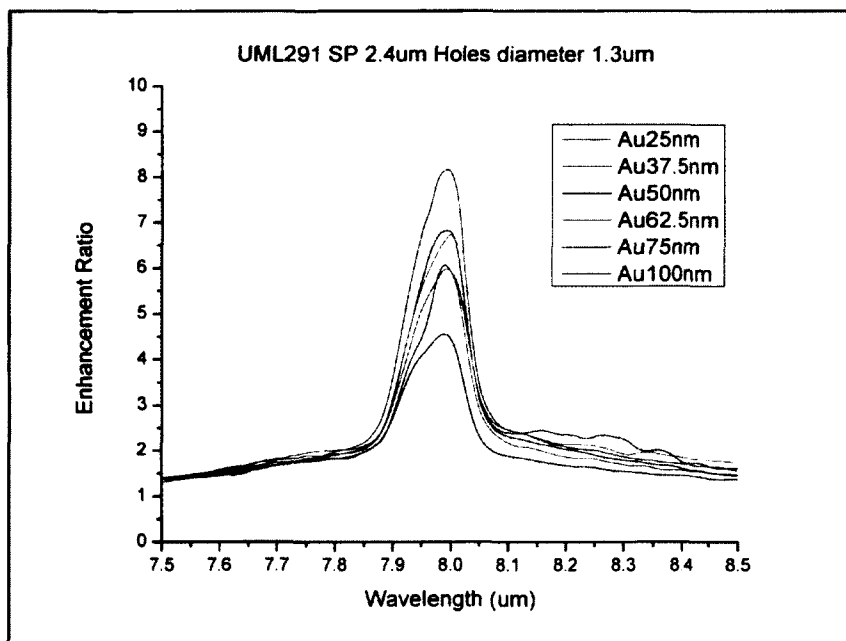
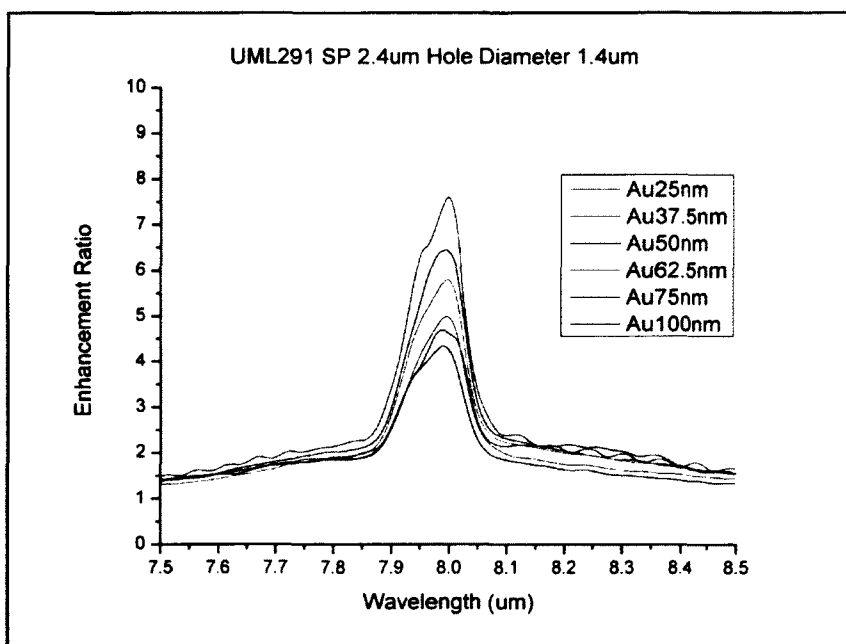


Figure 72 UML291-SP Hole Diameter 1.2 μm

Figure 73 UML291-SP Hole Diameter 1.3 μ mFigure 74 UML291-SP Hole Diameter 1.4 μ m

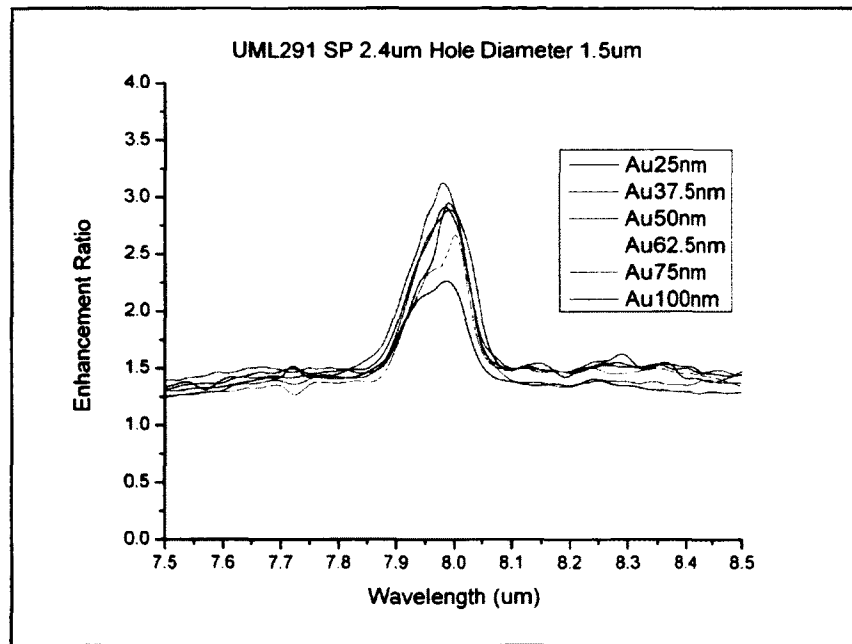


Figure 75 UML291-SP Hole Diameter 1.5um

The enhancement data is rearranged and presented in Figure 76, Figure 77, Figure 78, Figure 79, Figure 80, and Figure 81. The purpose is to demonstrate the optimization of hole diameter on surface plasmon structure on QDIPs. All of these figures show that the optimization of hole diameter is positively on hole diameter 1.3um. The highest enhancement is still on the thickness of 75um. Therefore, we conclude that the optimization of surface plasmon structure 2.4um period on the QDIP is at the gold thickness of 75nm and hole diameter of 1.3um.

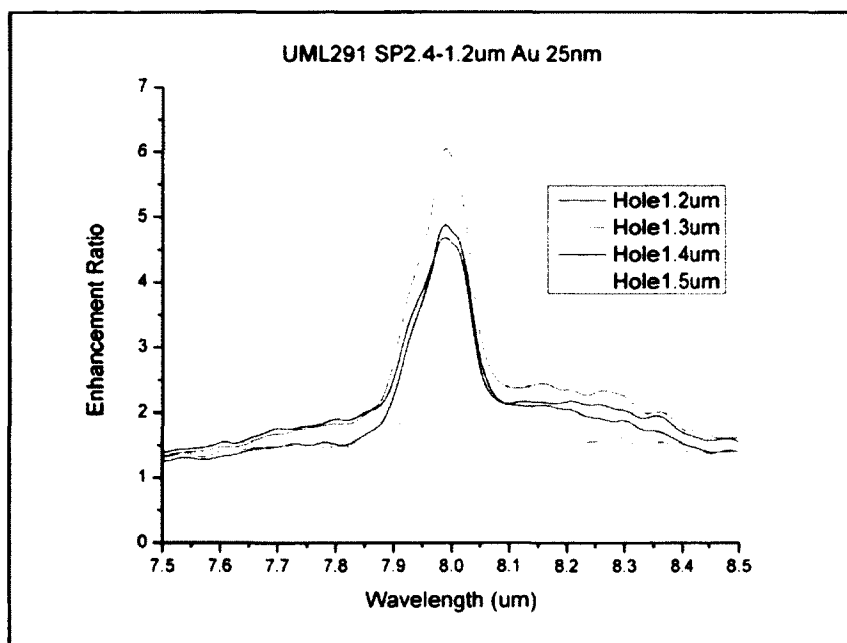


Figure 76 UML291-SP Au 25nm

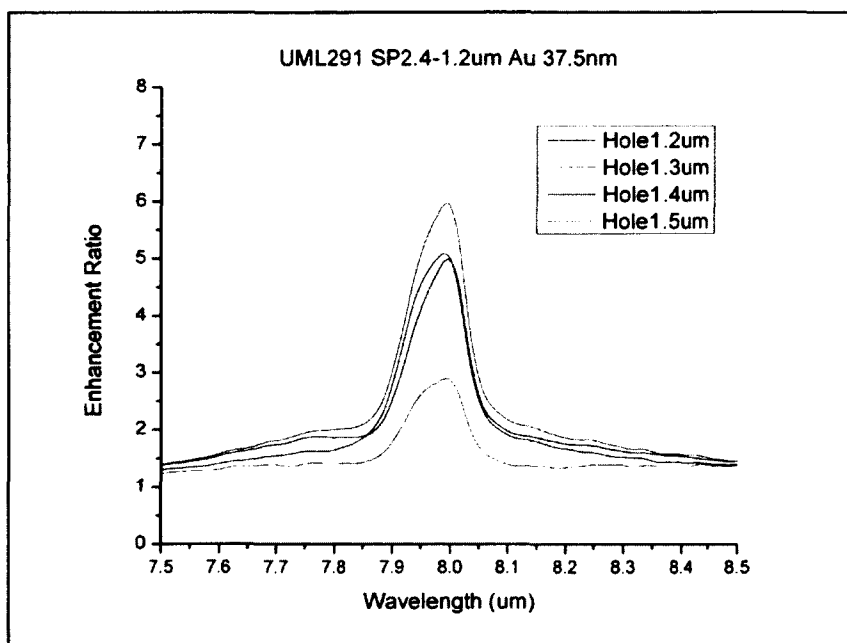


Figure 77 UML291-SP Au 37.5nm

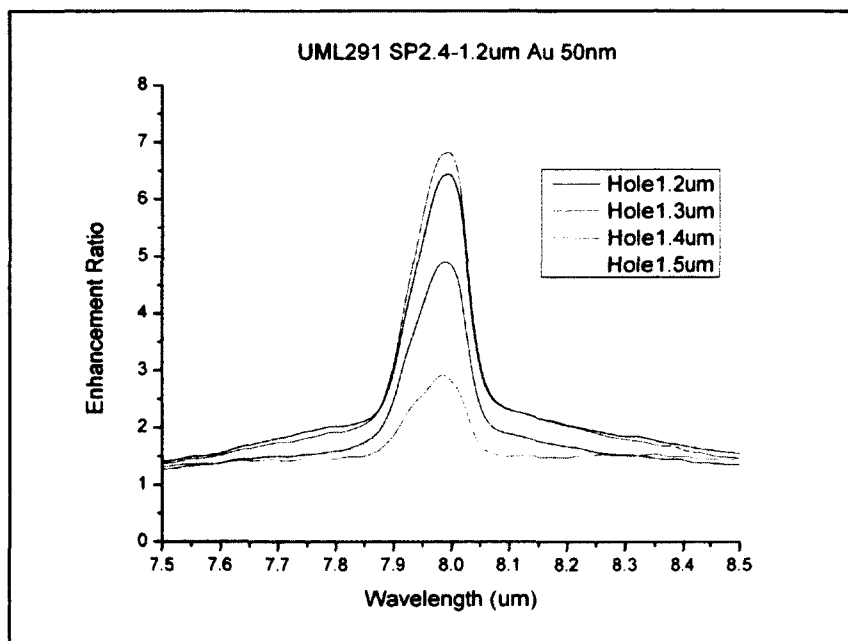


Figure 78 UML291-SP Au 50nm

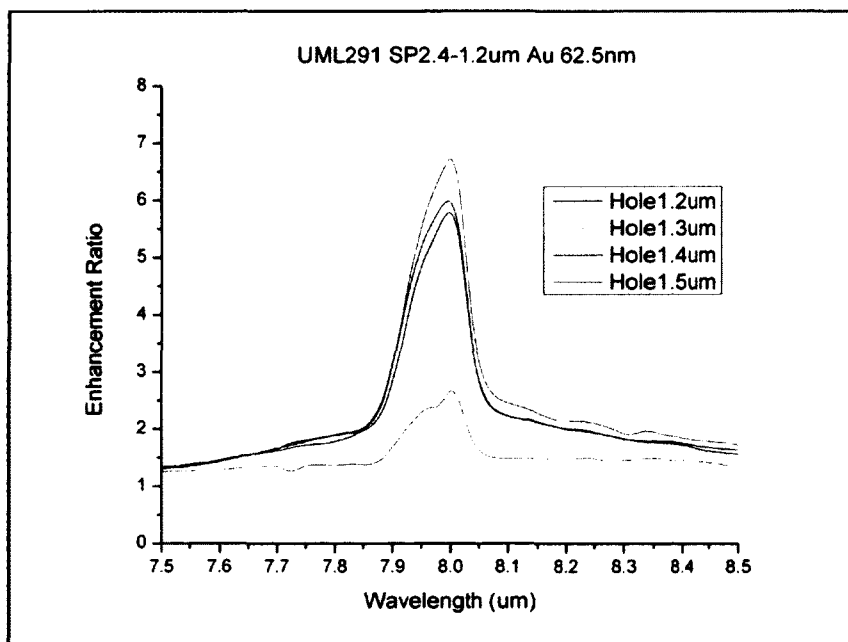


Figure 79 UML291-SP Au 62.5nm

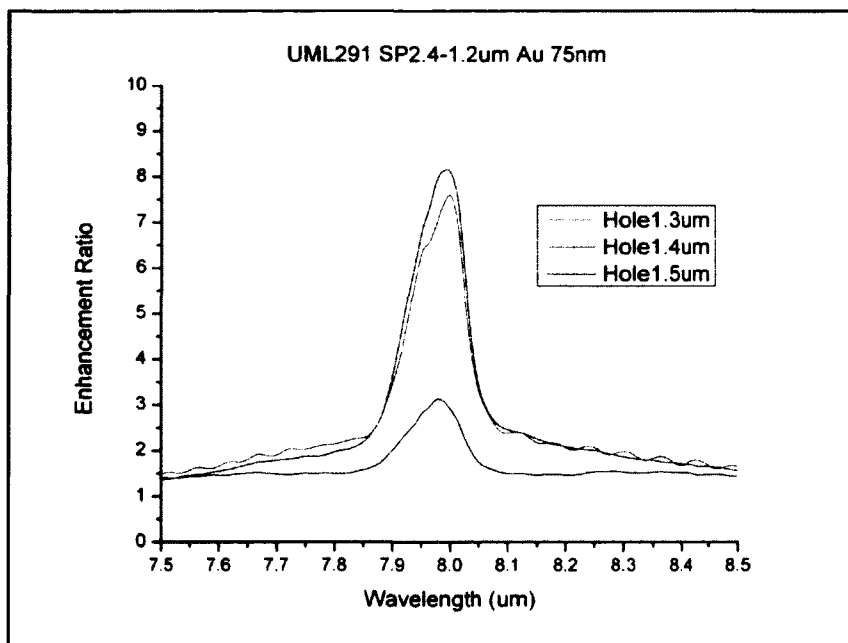


Figure 80 UML291-SP Au 75nm

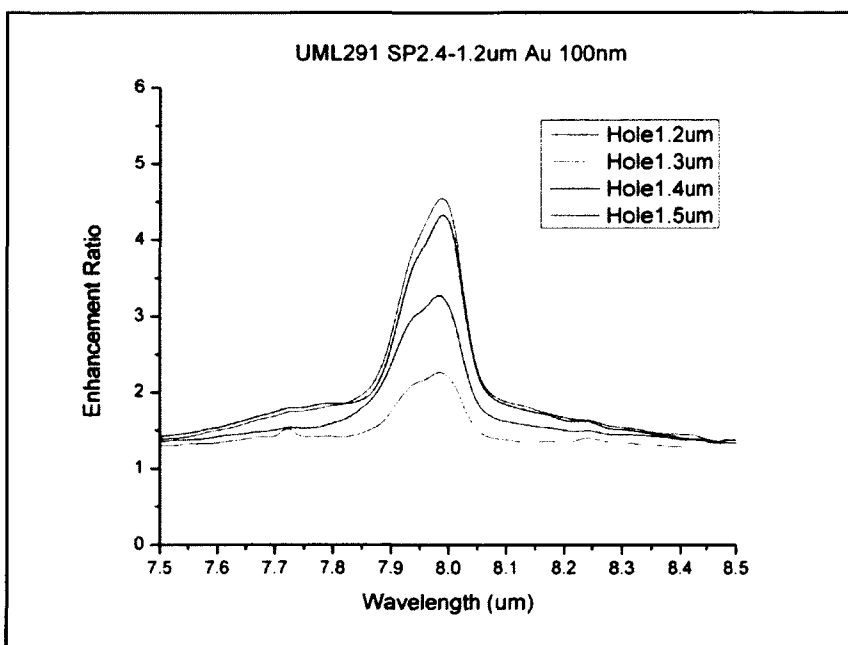


Figure 81 UML291-SP Au 100nm

5. Conclusion

In summary, we have reported the enhancement of photocurrent on QDIPs with plasmonics structure. We have shown that the performance enhancement of QDIP can be obtained by optimizing the metal thickness of the designed plasmonics structure. In addition, the optimized performance enhancement of QDIP can be also obtained by the hole diameter variation. From the transmission profile; the maximum and minimum values of the transmission profiles are reported from the metal thickness of 15nm-300nm. The surface plasmon structure is then applied on the QDIP and found the maximum photocurrent enhancement at metal thickness of 75nm for surface plasmon structure 2.6um period. Additional experiments were carried out for surface plasmon structure 2.4um and varied hole diameter. It is found that the 8-times maximum photocurrent enhancement is optimized at a hole diameter of 1.3um and metal thickness of 75nm. Our results address the development of infrared sensor on single detector and potentially offer the development of focal plane array cameras which will improve the performance of infrared camera.

VI. LITERATURE CITED

1. Tidrow, M.Z., *Device physics and state-of-the-art of quantum well infrared photodetectors and arrays*. Materials Science and Engineering B, 2000. **74**(1-3): p. 45-51.
2. Tidrow, M.Z. and W.R. Dyer, *Quantum Well Infrared Focal Plane Arrays for Ballistic Missile Defense and Space Applications*, in *RTO SET Symposium on "Space-Based Observation Technology"*. 2000: Island of Samos, Greece.
3. Xudong, J., S.S. Li, and M.Z. Tidrow, *Investigation of a multistack voltage-tunable four-color quantum-well infrared photodetector for mid- and long-wavelength infrared detection*. Quantum Electronics, IEEE Journal of, 1999. **35**(11): p. 1685-1692.
4. Stiff-Roberts, A.D., *Quantum-dot infrared photodetectors: a review*. Journal of Nanophotonics, 2009. **3**: p. 031607-17.
5. Bhattacharya, P., S. Ghosh, and A.D. Stiff-Roberts, *QUANTUM DOT OPTO-ELECTRONIC DEVICES*. Annual Review of Materials Research, 2004. **34**(1): p. 1-40.
6. Ebbesen, T.W., et al., *Extraordinary optical transmission through sub-wavelength hole arrays*. Nature, 1998. **391**(6668): p. 667-669.
7. Ghaemi, H.F., et al., *Surface plasmons enhance optical transmission through subwavelength holes*. Physical Review B, 1998. **58**(11): p. 6779-6782.
8. Matsui, T., et al., *Transmission resonances through aperiodic arrays of subwavelength apertures*. Nature, 2007. **446**(7135): p. 517-521.
9. Salomon, L., et al., *Near-Field Distribution of Optical Transmission of Periodic Subwavelength Holes in a Metal Film*. Physical Review Letters, 2001. **86**(6): p. 1110-1113.
10. Popov, E., et al., *Theory of light transmission through subwavelength periodic hole arrays*. Physical Review B, 2000. **62**(23): p. 16100-16108.
11. Stockman, M.I., *Nanoscience: Dark-hot resonances*. Nature, 2010. **467**(7315): p. 541-542.
12. Maier, S.A. and H.A. Atwater, *Plasmonics: Localization and guiding of electromagnetic energy in metal/dielectric structures*. Journal of Applied Physics, 2005. **98**(1): p. 011101-10.
13. Parsons, J., et al., *Localized surface-plasmon resonances in periodic nondiffracting metallic nanoparticle and nanohole arrays*. Physical Review B, 2009. **79**(7): p. 073412.
14. Attaluri, R.S., *Growth and Optimization of Quantum Dots-in-a-well Infrared Photodetectors*, in *Electrical Engineering*. 2007, University of New Mexico.
15. Xuejun, L., V. Jarrod, and J.M. Mark, *Temperature-dependent photoresponsivity and high-temperature (190 K) operation of a quantum dot infrared photodetector*. Applied Physics Letters, 2007. **91**(5): p. 051115.
16. Levine, B.F., *Quantum-well infrared photodetectors*. Journal of Applied Physics, 1993. **74**(8): p. R1-R81.
17. http://en.wikipedia.org/wiki/Lycurgus_Cup. *Lycurgus Cup*. 2011 [cited].

18. Mie, G., *Beiträge zur Optik trüber Medien, speziell kolloidaler Metallösungen*. Annalen der Physik, 1908. **330**(3): p. 377-445.
19. Ritchie, R.H., *Plasma Losses by Fast Electrons in Thin Films*. Physical Review, 1957. **106**(5): p. 874-881.
20. Genet, C. and T.W. Ebbesen, *Light in tiny holes*. Nature, 2007. **445**(7123): p. 39-46.
21. Bethe, H.A., *Theory of Diffraction by Small Holes*. Physical Review, 1944. **66**(7-8): p. 163-182.
22. Atwater, H.A. and A. Polman, *Plasmonics for improved photovoltaic devices*. Nat Mater, 2010. **9**(3): p. 205-213.
23. Ferry, V.E., et al., *Light trapping in ultrathin plasmonic solar cells*. Opt. Express, 2010. **18**(S2): p. A237-A245.
24. Ferry, V.E., et al., *Plasmonic Nanostructure Design for Efficient Light Coupling into Solar Cells*. Nano Letters, 2008. **8**(12): p. 4391-4397.
25. Catchpole, K.R. and A. Polman, *Plasmonic solar cells*. Opt. Express, 2008. **16**(26): p. 21793-21800.
26. Jestl, M., et al., *Polarization-sensitive surface plasmon Schottky detectors*. Opt. Lett., 1989. **14**(14): p. 719-721.
27. Liu, N., et al., *Infrared Perfect Absorber and Its Application As Plasmonic Sensor*. Nano Letters, 2010. **10**(7): p. 2342-2348.
28. Homola, J.Ä.Ä., S.S. Yee, and G.n. Gauglitz, *Surface plasmon resonance sensors: review*. Sensors and Actuators B: Chemical, 1999. **54**(1-2): p. 3-15.
29. Yu, N., et al., *Quantum cascade lasers with integrated plasmonic antenna-array collimators*. Opt. Express, 2008. **16**(24): p. 19447-19461.
30. SchnellM, et al., *Nanofocusing of mid-infrared energy with tapered transmission lines*. Nat Photon, 2011. **5**(5): p. 283-287.
31. Yu, N., et al., *Designer spoof surface plasmon structures collimate terahertz laser beams*. Nat Mater, 2010. **9**(9): p. 730-735.
32. Nanfang, Y., et al., *Plasmonics for Laser Beam Shaping*. Nanotechnology, IEEE Transactions on, 2010. **9**(1): p. 11-29.
33. Vuckovic, J., M. Loncar, and A. Scherer, *Surface plasmon enhanced light-emitting diode*. Quantum Electronics, IEEE Journal of, 2000. **36**(10): p. 1131-1144.
34. Bohren, C.F. and D.R. Huffman, *Absorption and Scattering of Light by Small Particles*. 1983, New York: Wiley.
35. Murray, W.A. and W.L. Barnes, *Plasmonic Materials*. Advanced Materials, 2007. **19**(22): p. 3771-3782.
36. Palik, E.D. and G. Ghosh. *Handbook of optical constants of solids*. 1998 [cited; Available from: <http://www.knovel.com/knovel2/Toc.jsp?BookID=1669>].
37. Raether, H., *Surface Plasmons on Smooth and Rough Surfaces and on Grateings*. 1988: Springer, Berlin.
38. Maier, S.A. *Plasmonics fundamentals and applications*. 2007 [cited; Available from: <http://dx.doi.org/10.1007/0-387-37825-1>].
39. Genet, C., M.P. van Exter, and J.P. Woerdman, *Fano-type interpretation of red shifts and red tails in hole array transmission spectra*. Optics Communications, 2003. **225**(4-6): p. 331-336.
40. Fano, U., *Effects of Configuration Interaction on Intensities and Phase Shifts*. Physical Review, 1961. **124**(6): p. 1866-1878.
41. Chang, C.-C., et al., *A Surface Plasmon Enhanced Infrared Photodetector Based on InAs Quantum Dots*. Nano Letters, 2010. **10**(5): p. 1704-1709.

42. Kuwata, H., et al., *Resonant light scattering from metal nanoparticles: Practical analysis beyond Rayleigh approximation*. Applied Physics Letters, 2003. **83**(22): p. 4625-4627.
43. Grigorenko, A.N., et al., *Nanofabricated media with negative permeability at visible frequencies*. Nature, 2005. **438**(7066): p. 335-338.
44. Wood, R.W., *Anomalous Diffraction Gratings*. Physical Review, 1935. **48**(12): p. 928-936.
45. Pacifici, D., H.J. Lezec, and H.A. Atwater, *All-optical modulation by plasmonic excitation of CdSe quantum dots*. Nat Photon, 2007. **1**(7): p. 402-406.
46. Wei, W., B. Alireza, and M. Hooman, *Plasmonic enhanced quantum well infrared photodetector with high detectivity*. Applied Physics Letters, 2010. **96**(16): p. 161107.
47. Vasinajindakaw, P., et al., *A Fano-type interference enhanced quantum dot infrared photodetector*. Applied Physics Letters, 2011. **98**(21): p. 211111-211111-3.
48. Chi-Yang, C., et al., *Wavelength selective quantum dot infrared photodetector with periodic metal hole arrays*. Applied Physics Letters, 2007. **91**(16): p. 163107.
49. Lee, S.C., S. Krishna, and S.R.J. Brueck, *Quantum dot infrared photodetector enhanced by surface plasma wave excitation*. Opt. Express, 2009. **17**(25): p. 23160-23168.
50. Lee, S.C., S. Krishna, and S.R.J. Brueck, *Plasmonic-Enhanced Photodetectors for Focal Plane Arrays*. Photonics Technology Letters, IEEE, 2011. **23**(14): p. 935-937.
51. Khurgin, J.B. and G. Sun, *Enhancement of light absorption in a quantum well by surface plasmon polariton*. Applied Physics Letters, 2009. **94**(19): p. 191106-191106-3.
52. Coe, J.V., et al., *Extraordinary Transmission of Metal Films with Arrays of Subwavelength Holes*. Annual Review of Physical Chemistry, 2008. **59**(1): p. 179-202.
53. Krishnan, A., et al., *Evanescently coupled resonance in surface plasmon enhanced transmission*. Optics Communications, 2001. **200**(1-6): p. 1-7.
54. Chang, S.-H., S. Gray, and G. Schatz, *Surface plasmon generation and light transmission by isolated nanoholes and arrays of nanoholes in thin metal films*. Opt. Express, 2005. **13**(8): p. 3150-3165.
55. Ordal, M.A., et al., *Optical properties of the metals Al, Co, Cu, Au, Fe, Pb, Ni, Pd, Pt, Ag, Ti, and W in the infrared and far infrared*. Appl. Opt., 1983. **22**(7): p. 1099-1119.
56. Lindquist, N.C., et al., *Monolithic Integration of Continuously Tunable Plasmonic Nanostructures*. Nano Letters, 2011. **11**(9): p. 3526-3530.
57. Mahboub, O., et al., *Optimization of bull's eye structures for transmission enhancement*. Opt. Express, 2010. **18**(11): p. 11292-11299.
58. Lochbihler, H., *Surface polaritons on gold-wire gratings*. Physical Review B, 1994. **50**(7): p. 4795-4801.
59. Grupp, D.E., et al., *Crucial role of metal surface in enhanced transmission through subwavelength apertures*. Applied Physics Letters, 2000. **77**(11): p. 1569-1571.
60. Aouani, H., et al., *Bright Unidirectional Fluorescence Emission of Molecules in a Nanoaperture with Plasmonic Corrugations*. Nano Letters, 2011. **11**(2): p. 637-644.